Mechanical Models of Friction That Exhibit Hysteresis, Stick-Slip, and the Stribeck Effect

by

Bojana Drinčić

A dissertation submitted in partial fulfillment
of the requirements for the degree of
Doctor of Philosophy
(Aerospace Engineering)
in The University of Michigan
2012

Doctoral Committee:

Professor Dennis S. Bernstein, Chair
Professor James R. Barber
Professor Pierre Tshimanga Kabamba
Assistant Professor Anouck Renee Girard

Sve što čovek, bilo čime da se bavi u životu,
uradi sa žarom, ljubavlju i prevelikom strašću,
sve je pesma.

-Miroslav "Mika" Antić

Everything a man, whatever his calling in life,
does with fervor, love and overwhelming passion,
everything is a poem.

-Miroslav "Mika" Antić

Mom kolegi, Deda Raki

To my colleague, Grandpa-Raka

ACKNOWLEDGEMENTS

I would like to thank my advisor Prof. Dennis Bernstein for his support, advice, and direction during the past five years. I would also like to thank my committee members Prof. James Barber, Prof. Anouck Girard, and Prof. Pierre Kabamba for their suggestions and comments on ways to improve my dissertation.

I am grateful to my friends Ashley Verhoff, Anna Luisa Polachini, Shayna Hall, Marco Ceze, Tony D'Amato, Tim Eymann, Eric Muir, Lisa Muir, Erin Farbar, Matt Fledderjohn, and Caty Tillman Fledderjohn for all the good times. I will miss you all immensely and hope that we will see each other soon. Special thanks goes out to my office mate Scott Stapleton for all the great conversations we've had for the past five years.

I would like to thank my parents Vesna and Dragan Drinčić and the rest of my family for their never-ending support and encouragement during my studies. I would also like to thank my grandpa Raka for being an amazing role model. I hope that my legacy will be as great as his. Finally, I want to thank my husband Matthew S. Holzel for his patience, love, understanding, and for making all my dreams come true.

TABLE OF CONTENTS

LIST OF FIGURES

Figure

LIST OF TABLES

Table

ABSTRACT

Mechanical Models of Friction That Exhibit Hysteresis, Stick-Slip, and the Stribeck Effect

by

Bojana Drinčić

Chair: Dennis S. Bernstein

In this dissertation, we model hysteretic and friction phenomena without introducing friction or hysteresis per se. We use a combination of masses, springs, and dashpots and the frictional phenomena emerge as the result of their interaction. By using physical elements, we can understand the physical mechanisms that lead to hysteretic energy dissipation and phenomena, such as stick-slip behavior and the Stribeck effect. Furthermore, we study the origins of butterfly hysteresis, which arises in optics and ferromagnetism.

We define the multiplay model for hysteresis with nonlocal memory, which consists of N mass/spring/dashpot with deadzone elements. The advantage of this model is that its hysteresis map can be inverted analytically.

Second, we investigate the origins of stick-slip friction by developing an asperity-based friction model involving the frictionless contact between a body and a row of rigid, rotating bristles. This model exhibits hysteresis and quasi-stick-slip friction. The hysteretic energy-dissipation mechanism is the sudden release of the pivoted

bristles. The discontinuous rotating bristle model is an approximation of the rotating bristle model that exhibits exact stick-slip and hysteresis.

We next develop an asperity-based friction model in which the vertical motion of the body leads to the Stribeck effect. The friction model is hysteretic and the energy-dissipation mechanism is the sudden release of the compressed bristles. We show that this bristle model is a generalization of the LuGre model.

The final contribution of this dissertation is a framework for relating butterfly-shaped hysteresis maps to simple hysteresis maps, which are typically easier to model and more amenable to control design. In particular, a unimodal mapping is used to transform simple loops to butterfly loops.

CHAPTER I

Introduction

Friction is a force resisting the relative motion of two bodies sliding over each other. It is a widespread phenomenon that has many practical uses such as walking and driving and is instrumental in mechanical processes such as grinding and polishing. However, friction also wastes energy and causes wear. Due to its a crucial role in design, modeling, and control, friction is studied extensively [2–9]. Furthermore, the understanding of friction is important in many aerospace applications. For example, friction in bolted joints impacts the structural dynamics of ballistic missiles and other built-up structures [10–13]. In airplane engines, friction can lead to turbine blade failure due to fretting fatigue [14–16]. Friction stir welding is used in the aerospace industry for construction of aircraft and spacecraft where the properties of the welded materials must be unchanged by the welding process [17–19].

As a result of the pervasiveness of friction, a large number of friction models exist and are based either on the physics of the surface interactions [8, 20, 21] or on the experimental observations [6, 22–30]. Furthermore, since friction is a macroscopic phenomenon that arises due to the interaction of surfaces on the microscopic level, asperity-based friction models are also often used [5, 6, 31, 32]. The most commonly used friction models are Maxwell-slip [33–35], Dahl [36–38], and LuGre models [26–28], which are discussed in more detail in the Section 1.3.

In order to study friction which is a hysteretic phenomenon, it is necessary to also understand hysteresis. Hysteresis is a non vanishing input-output loop in the limit as the frequency of the input goes to zero [39]. It is present in many applications such as ferromagnetism [40–42], smart materials [43–45], aerodynamic stall [46–48], biological systems [49,50], optics [51,52], and friction [2,6,35,53]. It arises in systems with multiple stable equilibria, where as the input slowly increases, the output is attracted to one set of stable equilibria and as the input slowly decreases the output is attracted to a different set of stable equilibria [39]. This type of system is said to have multistability, that is, for a constant value of the input, the system has multiple corresponding stable equilibria. For a single-input, single-output system, hysteresis is manifested by the existence of a non-vanishing input-output loop in the limit as the frequency of the input tends to zero [54,55]. Hysteresis is an inherently nonlinear effect since no such loop persists for asymptotically stable linear systems.

In this dissertation, the goal is to model hysteretic and friction phenomena without introducing friction or hysteresis per se. We begin with a combination of masses, springs, and dashpots, and the frictional phenomena emerge as the result of their interaction. By using physical elements, we can obtain insight into the physical mechanisms that lead to hysteretic energy dissipation and phenomena such as stick-slip [56–58] and the Stribeck effect [27,59]. The stick-slip refers to motion in which a body attached to a compliance periodically comes to rest. This kind of motion, which is reminiscent of a limit cycle, occurs when the friction force drops as velocity increases from zero. The Stribeck effect is the apparent drop in the friction force as the velocity increases. Furthermore, we study the origins of butterfly hysteresis, which is present in optics and ferromagnetism [40,60–62].

1.1 Introduction to Systems with Hysteresis

Since friction arises in hysteretic systems, we begin by defining hysteresis and discussing the types of systems that exhibit hysteresis. Next, we give a brief overview of hysteretic models which are commonly encountered in the literature. Finally, we describe the three friction models which are often used to describe systems with friction.

In this section we introduce basic concepts and terminology from the literature on hysteresis. We use these definitions throughout this dissertation and they are also available in [22, 63]. Consider the single-input, single-output system

$$\dot{\boldsymbol{x}}(t) = \boldsymbol{f}(\boldsymbol{x}(t), u(t)), \quad \boldsymbol{x}(0) = \boldsymbol{x}_0, \quad t \geq 0, \tag{1.1}$$

$$y(t) = h(\boldsymbol{x}(t), u(t)), \tag{1.2}$$

where $u : [0, \infty) \to \mathbb{R}$ is continuous and piecewise C^1, $\boldsymbol{f} : \mathbb{R}^n \times \mathbb{R} \to \mathbb{R}^n$ is continuous, and $y : [0, \infty) \to \mathbb{R}$, and $h : \mathbb{R}^n \times \mathbb{R} \to \mathbb{R}$ are continuous. We assume that the solution to (1.1) exists and is unique on all finite intervals. The following definitions are necessary for further discussion.

Definition 1.1.1. Consider (1.1)-(1.2) with constant $u(t) = \bar{u}$. The system (1.1)-(1.2) is *step convergent* if $\lim_{t\to\infty} x(t)$ exists for all $x_0 \in \mathbb{R}^n$ and for all $\bar{u} \in \mathbb{R}$.

Definition 1.1.2. The nonempty set $\mathcal{H} \subset \mathbb{R}^2$ is a *closed curve* if there exists a continuous, piecewise C^1, and periodic map $\gamma : [0, \infty) \to \mathbb{R}^2$ such that $\gamma([0, \infty)) = \mathcal{H}$.

For the system (1.1)-(1.2), we define a periodic input-output map and the limiting periodic input-output map or a hysteresis map as follows.

Definition 1.1.3. Let $u : [0, \infty) \to [u_{\min}, u_{\max}]$ be continuous, piecewise C^1, periodic with period α, and have exactly one local maximum $u_{\max}$ for $t \in [0, \alpha)$ and exactly one local minimum $u_{\min}$ for $t \in [0, \alpha)$. For all $T > 0$, define $u_T(t) \triangleq u(\alpha t/T)$,

assume that there exists $\boldsymbol{x}_T : [0, \infty) \to \mathbb{R}^n$ that is periodic with period T and satisfies (1.1) with $u = u_T$, and let $y_T : [0, \infty) \to \mathbb{R}$ be given by (1.2) with $\boldsymbol{x} = \boldsymbol{x}_T$ and $u = u_T$. For all $T > 0$, the *periodic input-output map* $\mathcal{H}_T(u_T, \boldsymbol{x}_0)$ is the closed curve $\mathcal{H}_T(u_T, \boldsymbol{x}_0) \triangleq \{\big(u_T(t), y_T(t)\big) : t \in [0, \infty)\}$, and the *limiting periodic input-output map* $\mathcal{H}_\infty(u, \boldsymbol{x}_0)$ is the closed curve $\mathcal{H}_\infty(u, \boldsymbol{x}_0) \triangleq \lim_{T\to\infty} \mathcal{H}_T(u_T, y_T, \boldsymbol{x}_0)$ if the limit exists. If there exist $(u, y_1), (u, y_2) \in \mathcal{H}_\infty(u, \boldsymbol{x}_0)$ such that $y_1 \neq y_2$, then $\mathcal{H}_\infty(u)$ is a *hysteresis map*, and (1.1)-(1.2) is *hysteretic*.

Example 1.1.1. Consider the linear system that represents a body of mass m attached to a wall by a dashpot with damping coefficient c. The free end of the body is attached to a spring with stiffness coefficient k. A periodic position input $u(t)$ is applied to the free end of the spring. The equations that describe the system are

$$m\ddot{x}(t) + c\dot{x}(t) + k(x(t) - u(t)) = 0, \tag{1.3}$$

$$y(t) = x(t), \tag{1.4}$$

where $x(t)$ is the position of the center of mass of the body. The periodic input-output maps of (1.3)-(1.4) are shown in Figure 1.1 for $u(t) = \sin(\omega t)$, $m = 1$ kg, $c = 2$ N-s/m, $k = 1$ N/m, and $\omega = 1, 0.1, 0.01, 0.001$ rad/s. Although the periodic input-output map $\mathcal{H}_T(u_T, \boldsymbol{x}_0)$ forms a loop for $\omega = 1$ rad/s, the loop disappears as the frequency of the input tends to DC. Thus, the system (1.3)-(1.4) is not hysteretic.

□

Example 1.1.2. Now consider the cubic example [22]

$$\dot{x}(t) = -x^3(t) + x(t) + u(t), \tag{1.5}$$

$$y(t) = x(t), \tag{1.6}$$

where $u(t)$ is a periodic input and $y(t)$ is the system output. The periodic input-

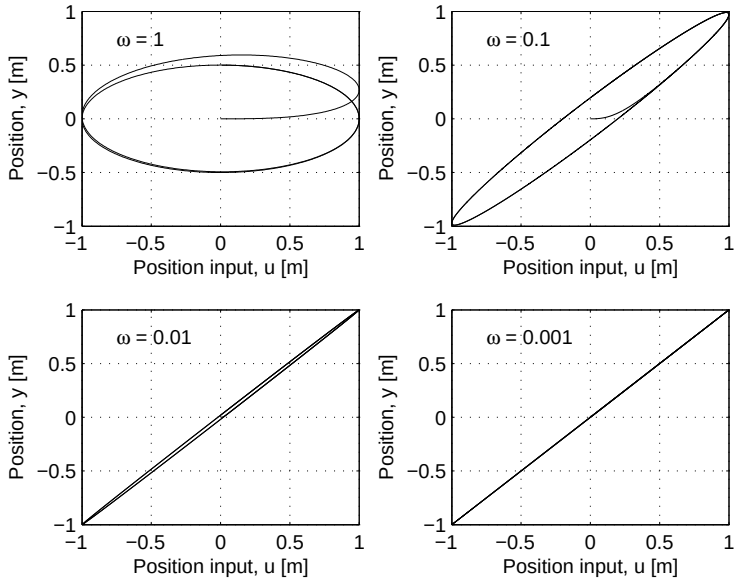

Figure 1.1: The periodic input-output maps $\mathcal{H}_T(u_T, y_T)$ of (1.3)-(1.4) with $u(t) = \sin(\omega t)$, $m = 1$ kg, $c = 2$ N-s/m, $k = 1$ N/m, and $\omega = 1, 0.1, 0.01, 0.001$ rad/s. The system (1.3)-(1.4) is not hysteretic since the loop in the input-output plane vanishes as the frequency of the input tends to DC.

output maps $\mathcal{H}_T(u_T, x_0)$ of (1.5)-(1.6) are shown in Figure 1.2 for $u(t) = \sin(\omega t)$ and $\omega = 1, 0.1, 0.01, 0.001$ rad/s. As the frequency of the input tends to DC, $\mathcal{H}_T(u_T, x_0)$ of (1.5)-(1.6) converges to the hysteretic limiting periodic input-output map $\mathcal{H}_\infty(u, x_0)$. Thus, the system (1.5)-(1.6) is hysteretic.

□

Definition 1.1.4. The *equilibria map* $\mathcal{E}$ of (1.1)-(1.2) is the set of points $(\bar{u}, h(\bar{\boldsymbol{x}}, \bar{u})) \in \mathbb{R}^2$ such that $\bar{u}$ and $\bar{\boldsymbol{x}}$ satisfy

$$\boldsymbol{f}(\bar{\boldsymbol{x}}, \bar{u}) = 0. \tag{1.7}$$

Suppose (1.1), (1.2) is step convergent. Then it follows from the above definitions that $\lim_{t\to\infty} x(t)$ exists for every constant $u(t) = \bar{u}$ and is an equilibrium of (1.1), (1.2). Now, let $u(t) \in [u_{\min}, u_{\max}]$ be periodic with period α. Let $u_T(t) = u(\alpha t/T)$ and suppose the *periodic input-output map* $\mathcal{H}(u_T, x_0)$ exists for all $T > 0$. Further-

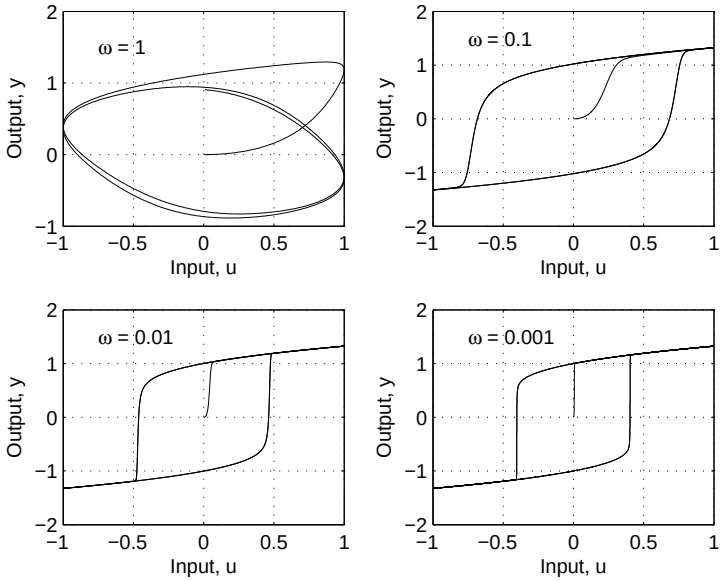

Figure 1.2: The periodic input-output maps $\mathcal{H}_T(u_T, y_T)$ of (1.5)-(1.6) with $u(t) = \sin(\omega t)$ and $\omega = 1, 0.1, 0.01, 0.001$ rad/s. As the frequency of the input tends to DC, $\mathcal{H}_T(u_T, y_T)$ of (1.5)-(1.6) converges to the hysteresis map $\mathcal{H}_\infty(u, x_0)$.

more, assume the *limiting periodic input-output map* $\mathcal{H}_\infty(u, x_0)$ exists. There exists a close relationship between $\mathcal{H}_\infty(u, \boldsymbol{x}_0)$ and the input-output equilibria map $\mathcal{E}$ of (1.1), (1.2). The set $\mathcal{H}_\infty(u, \boldsymbol{x}_0)$ represents the response of the system in the limit of DC operation. Therefore, each element of $\mathcal{H}_\infty(u, \boldsymbol{x}_0)$ is the limit of a sequence of points in $\mathcal{H}(u_T, \boldsymbol{x}_T(0))$ for a sequence of increasingly slower inputs. Thus, the limiting point $(\bar{u}, \bar{y}) \in \mathcal{H}_\infty(u, \boldsymbol{x}_0)$ is an equilibrium of (1.1), (1.2) corresponding to the constant input $u(t) = \bar{u}$, and thus is an element of $\mathcal{E}$.

However, not every point in $\mathcal{H}_\infty(u, \boldsymbol{x}_0)$ is in $\mathcal{E}$. If (1.1), (1.2) has a bifurcation, that is, a change in the qualitative structure of the equilibria as u changes, then the limiting solution of (1.1), (1.2), can alternate between the subsets of $\mathcal{E}$. In this particular case, the limiting periodic input-output map $\mathcal{H}_\infty(u, \boldsymbol{x}_0)$ contains vertical components that connect subsets. Thus, it follows that $\mathcal{H}_\infty(u, \boldsymbol{x}_0) \subseteq \mathcal{E}$.

Since the definition of hysteresis requires that the hysteresis map have at least two

distinct points (u, y_1) and (u, y_2), a necessary condition for (1.1), (1.2) to be hysteretic is that $\mathcal{E}$ be a multivalued map. However, not every nonlinear feedback model that has a multivalued map $\mathcal{E}$ exhibits hysteresis. The system (1.1), (1.2) is hysteretic if the multivalued map $\mathcal{E}$ has either a continuum of equilibria or a bifurcation for some $u \in [u_{\min}, u_{\max}]$.

Example 1.1.3. Reconsider the cubic model (1.5)-(1.6) in Example 1.1.2. For all constant inputs $u(t) = \bar{u}$, equilibria map $\mathcal{E}$ of (1.5)-(1.6) is the set

$$\mathcal{E} = \left\{(\bar{x}, \bar{u}) \in \mathbb{R} : -\bar{x}^3 + \bar{x} + \bar{u} = 0\right\}. \tag{1.8}$$

Figure 1.3(a) shows the equilibria map (1.8). Figure 1.3(b) shows the equilibria set $\mathcal{E}$ and the hysteresis map $\mathcal{H}_\infty(u, x_0)$ of the cubic model (1.5)-(1.6). $\mathcal{H}_\infty(u, x_0)$ is a subset of $\mathcal{E}$ everywhere except for the vertical portions, which represent the transition from one set of stable equilibria to another and appear at the points of bifurcations. □

Definition 1.1.5. If the hysteresis map $\mathcal{H}_\infty(u, \boldsymbol{x}_0)$ as described in Definition 1.1.3 exists, and if, in addition, $\mathcal{H}_\infty(u, \boldsymbol{x}_0)$ is independent of $\boldsymbol{x}_0$, then the system (1.1), (1.2) has *local memory*, and we write $\mathcal{H}_\infty(u)$. Otherwise, $\mathcal{H}_\infty(u, \boldsymbol{x}_0)$ has *nonlocal memory*.

The nonlocal memory of a system is manifested in the form of congruent minor loops. That is, for two different initial conditions $\boldsymbol{x}_0$, the same input $u(t)$ results in two different outputs $y(t)$.

Definition 1.1.6. The continuous and piecewise C^1 function $\tau : [0, \infty) \to [0, \infty)$ is a *positive time scale* if $\tau(0) = 0$, τ is nondecreasing, and $\lim_{t\to\infty} \tau(t) = \infty$. The system (1.1), (1.2) is *rate independent* if, for every pair of continuous and piecewise C^1 functions $\boldsymbol{x}$ and u satisfying (1.1) and for every positive time scale τ, it follows that $\boldsymbol{x}_\tau(t) \triangleq \boldsymbol{x}(\tau(t))$ and $u_\tau(t) \triangleq u(\tau(t))$ also satisfy (1.1).

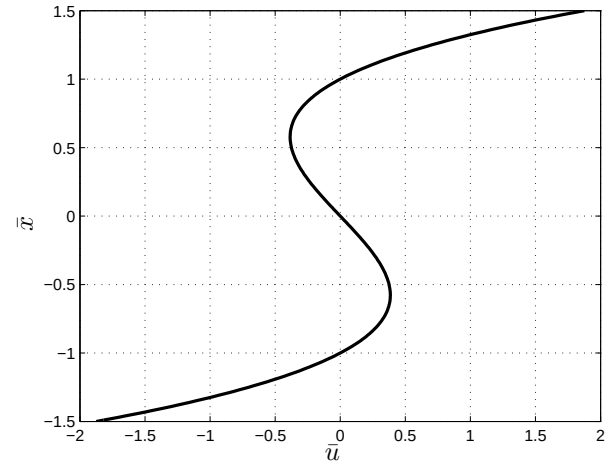

(a)

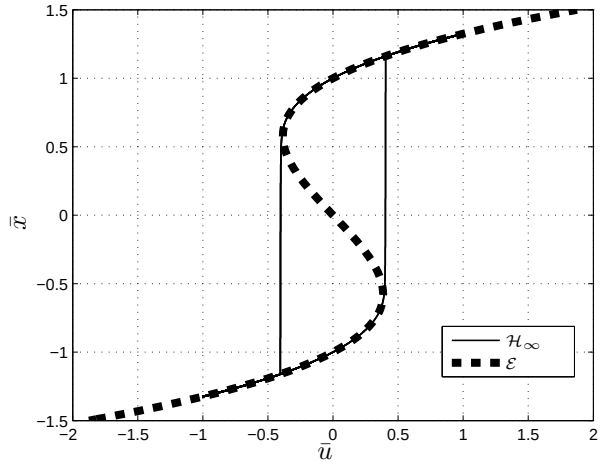

(b)

Figure 1.3: The equilibria map $\mathcal{E}$ and hysteresis map $\mathcal{H}_\infty(u, x_0)$ of the cubic model (1.5)-(1.6) in Example 1.1.2. (a) shows the equilibria map $\mathcal{E}$. (b) shows $\mathcal{E}$ and $\mathcal{H}_\infty(u, x_0)$. Note that, except for the vertical portions, $\mathcal{H}_\infty(u, \boldsymbol{x}_0) \subseteq \mathcal{E}$.

An easy way to determine whether a system is rate dependent or rate independent is to plot the periodic input-output maps $\mathcal{H}_T(u_T, \boldsymbol{x}_0)$ for several different frequencies of the input. If the shape of the $\mathcal{H}_T(u_T, \boldsymbol{x}_0)$ changes with frequency of the input, then (1.1)-(1.2) is a rate-dependent model.

Example 1.1.4. Reconsider the cubic model (1.5)-(1.6) in Example 1.1.2. Figure

1.2 shows the periodic input-output maps $\mathcal{H}_T(u_T, x_0)$ of (1.5)-(1.6) with $u(t) = \sin(\omega t)$ and $\omega = 1, 0.1, 0.01, 0.001$ rad/s. Note that the shape of $\mathcal{H}_T(u_T, x_0)$ changes with the frequency of the input, and converges to $\mathcal{H}_\infty(u, x_0)$ as the frequency of the input tends to zero. Thus, the cubic model (1.5)-(1.6) is rate dependent. □

1.2 Hysteretic Models

In the literature on hysteresis, there are three types of commonly used hysteresis models, namely, the Preisach model, the Duhem model, and the nonlinear feedback model. A brief overview of these models and their properties is given in Table 1.1.

Hysteresis Model	Rate Dependence	Type of Memory
Preisach	rate-independent	nonlocal
Duhem	rate-dependent or independent	local or nonlocal
Nonlinear Feedback	rate-dependent	nonlocal

Table 1.1: Hysteresis models and their properties.

The Preisach model [64–67] is an integral operator, that operates on an infinite number of elementary hysteresis operators called hysterons. The hysterons are turned "on" or "off" depending on the direction and value of the input. The hysterons that are "on" contribute to the output, while the hysterons that are "off" do not. The Preisach model has the form

$$y(t) = \int\int_{\alpha \geq \beta} \mu(\alpha, \beta) \hat{\gamma}_{\alpha\beta} u(t) \, d\alpha \, d\beta, \tag{1.9}$$

where $\mu(\alpha, \beta)$ is a weight function, $u(t)$ is the input, the hysteresis operator $\hat{\gamma}_{\alpha\beta}$ is called a hysteron, and α and β are the values at which the output of the hysteron is switched on and off, respectively. Preisach models are rate-independent and have nonlocal memory. They are often used to model hysteresis in piezoceramic actuators,

shape memory alloys, and magnetism [65,68,69]. The Prandtl-Ishlinskii model, which is a special type of Preisach model, replaces the hysterons by the play operators weighted by a density function [66, 70–72]. We discuss it in more detail in Chapter V.

The state of the Duhem model depends on the derivative of the input and thus the output changes its character when the input changes direction [22,27,36,55]. The general form of the Duhem model is

$$\dot{\boldsymbol{x}}(t) = f(\boldsymbol{x}(t), u(t))g(\dot{u}(t)), \tag{1.10}$$

$$y(t) = h(\boldsymbol{x}(t), u(t)), \tag{1.11}$$

where g is a function that determines how the output changes as the input changes direction [55]. The function g satisfies $g(0) = 0$ and thus, for a constant input $u(t) = \bar{u}$, there is an infinite number of equilibria. Duhem models can be rate dependent or rate independent and can exhibit local or nonlocal memory [22]. Commonly used examples of the Duhem model are Maxwell-slip, Dahl, and LuGre models described in Section 1.3.

Nonlinear feedback models are studied in [54, 63] and consist of a linear system connected in feedback to a memoryless nonlinearity. Single-input, single-output nonlinear feedback models have the form

$$\dot{\boldsymbol{x}}(t) = A\boldsymbol{x}(t) + Du(t) + By_\phi(t), \qquad \boldsymbol{x}(0) = \boldsymbol{x}_0, \quad t \geq 0, \tag{1.12}$$

$$y(t) = C\boldsymbol{x}(t), \tag{1.13}$$

$$u_\phi(t) = E_1\boldsymbol{x}(t) + E_0u(t), \tag{1.14}$$

$$y_\phi(t) = \phi\big(u_\phi(t)\big), \tag{1.15}$$

where $A \in \mathbb{R}^{n\times n}$, $D \in \mathbb{R}^n$, $B \in \mathbb{R}^n$, $C \in \mathbb{R}^{1\times n}$, $E_1 \in \mathbb{R}^{1\times n}$, $E_0 \in \mathbb{R}$, $u : [0, \infty) \to \mathbb{R}$ is

continuous and piecewise C^1, $\phi : \mathbb{R} \to \mathbb{R}$ is a static nonlinearity, and $\boldsymbol{x}(t)$, $\boldsymbol{x}_0 \in \mathbb{R}^n$. Nonlinearities such as deadzone, cubic, and sinusoid can give rise to hysteresis in a nonlinear feedback model. These models are rate dependent. A well-known example of a nonlinear feedback model is backlash, which usually arises due to free play in mechanical engineering applications [73–75].

1.3 Friction Models

In this section we present four commonly used hysteretic friction models, namely, Coulomb model, Maxwell-Slip model, Dahl model, and LuGre model. We present the model equations and investigate their input-output properties by varying the input frequency and amplitude. Based on the input-output maps, we conclude whether the model exhibits rate dependent or rate independent hysteresis and whether it has local or nonlocal memory. The properties of the three models are classified in Table 1.2.

Friction Model		Rate Dependence	Continuity
Coulomb		rate-independent	discontinuous
Maxwell-slip		rate-independent	discontinuous
Dahl	$\gamma = 0$	rate-independent	discontinuous
	$0 < \gamma < 1$	rate-independent	continuous but not Lipschitz
	$\gamma \geq 1$	rate-independent	Lipschitz
LuGre		rate-dependent	Lipschitz

Table 1.2: Classification and properties of friction models.

1.3.1 Coulomb Model

The magnitude of the Coulomb model friction force is proportional to the normal load [24], that is,

$$F_C = \mu F_N, \tag{1.16}$$

where μ is commonly refereed to as the friction coefficient and F_N is the normal force. The magnitude of the Coulomb model friction force is independent of the magnitude of the velocity and the contact area and the friction force opposes the motion of the body. The friction force can be expressed as

$$F_f = \text{sign}(v) F_C, \tag{1.17}$$

where v is the velocity of the body relative to the surface it is sliding over [24, 76, 77]. Figure 1.4 shows the Coulomb model friction force as a function of velocity. The Coulomb model is rate independent.

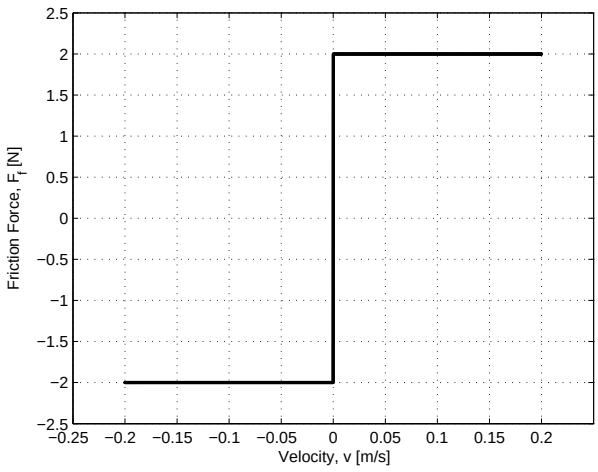

Figure 1.4: The Coulomb model friction force as a function of velocity.

Consider a body of mass m connected to a wall by a spring with stiffness coefficient K, sliding on the ground under the influence of a periodic input force u. The equations of motion are

$$m\ddot{x}(t) + Kx(t) = u(t) - F_f, \tag{1.18}$$

where F_f is defined by (1.17). By defining $\text{sign}(v) \triangleq [0, 1]$, the equilibria map of

(1.18) for constant $u(t) = \bar{u}$ can be defined as

$$\mathcal{E} = \left\{ (\bar{u}, \bar{x}) : \bar{u} \in \mathbb{R}, \bar{x} = \frac{1}{K} \left(\bar{u} - (2\alpha - 1) F_C \right), \alpha \in [0, 1] \right\}. \tag{1.19}$$

A portion of the equilibria map $\mathcal{E}$ defined by (1.19) corresponding to $\bar{u} \in [-3, 3]$ is shown shaded in Figure 1.5. Note that, for each constant value of u, the corresponding subset of $\mathcal{E}$ is a continuum. Figure 1.5 also shows the hysteresis map of (1.18) with $u = 3\sin(0.001t)$ N, $m = 1$ kg, $K = 1$ N/m, and $F_C = 2$ N. The hysteresis map is a subset of the equilibria map.

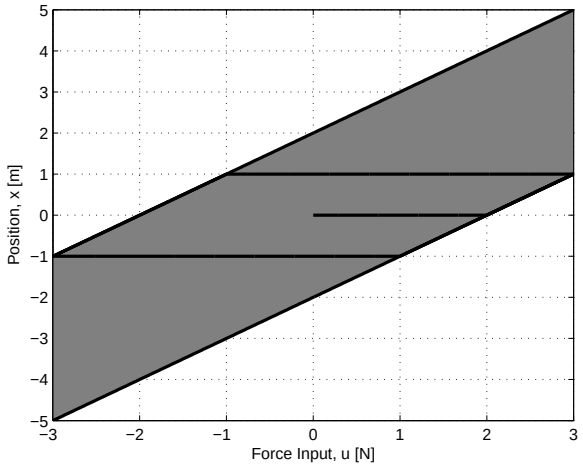

Figure 1.5: The equilibria map and the hysteresis map of the (1.18) with the Coulomb friction force (1.17). The shaded area represents the equilibria map $\mathcal{E}$. For every constant value $\bar{u}$ of the input u, there is an infinite number of corresponding equilibria. The hysteresis map $\mathcal{H}_\infty$ is a subset of the equilibria map.

1.3.2 Maxwell-Slip Model

The Maxwell-slip model [33–35] shown in Figure 1.6 consists of N masses and N springs. For $i = 1, \ldots, N$, the mass m_i with displacement x_i is connected by a stiffness k_i to a common termination point whose displacement is u. Associated with each mass is a displacement deadband of width $\Delta_i > 0$, below which the mass does

not move, and above which the mass moves with velocity $\dot{u}$, that is, the inertia of the masses is ignored when the mass is sliding. Hence, $k_i\Delta_i$ is the minimum spring force needed to move the mass m_i. Once the mass m_i begins to move, the spring force remains at $k_i\Delta_i$ for all velocities of the mass. Hence, each mass-spring combination in the Maxwell-slip model is subjected to an equivalent Coulomb friction force $F = k_i\Delta_i$.

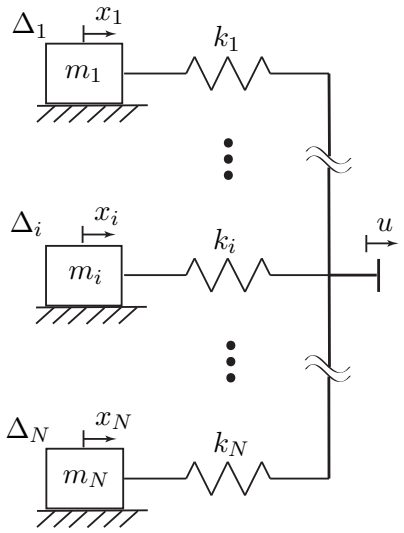

Figure 1.6: The Maxwell-slip model with N masses and N springs. Each mass is associated with a displacement deadband Δ_i, below which the mass does not move, and above which the mass moves with the same velocity as the common termination point.

We can represent the system of masses and springs shown in Figure 1.6 as the Duhem model [22, 27, 36, 55]

$$\dot{x}_i(t) = \begin{bmatrix} U\big(-x_i(t) + u(t) - \Delta_i\big) & 1 - U\big(-x_i(t) + u(t) + \Delta_i\big) \end{bmatrix} \begin{bmatrix} \dot{u}_+(t) \\ \dot{u}_-(t) \end{bmatrix}, \quad (1.20)$$

$$F_f(t) = \sum_{i=1}^{N} k_i\big(-x_i(t) + u(t)\big), \qquad i = 1, \ldots, N, \quad (1.21)$$

where F_f is the friction force and

$$U(v) \triangleq \begin{cases} 1, & v \geq 0, \\ 0, & v < 0. \end{cases} \tag{1.22}$$

Figure 1.7 shows the input-output maps of the Maxwell-slip model (1.20), (1.21) with $N = 10$. The frequency of the input is $\omega = 2$ rad/s in Figure 1.7(a) and $\omega = 0.1$ rad/s in Figure 1.7(b). The Maxwell-Slip model is rate independent which is demonstrated by the identical input-output maps at two different frequencies of the input. The input $u(t)$ is initially $u_1(t) = \sin(\omega t)$ and the friction force corresponds to the major loops in figures 1.7(a) and 1.7(b). When $u(t)$ changes to $u_2(t) = 0.5\sin(\omega t)$ after one period, the friction force F_f corresponds to the upper minor loops in figures 1.7(a) and 1.7(b). When $u(t)$ changes to $u_2(t)$ after one and a half periods, F_f corresponds to the lower minor loops in figures 1.7(a) and 1.7(b). Consequently, with identical inputs but different initial conditions, (1.20)-(1.21) result in distinct hysteresis maps. Thus, $\mathcal{H}_\infty(u, \boldsymbol{x}_0)$ depends on $\boldsymbol{x}_0$, and the Maxwell-slip model has nonlocal memory.

1.3.3 Dahl Model

The Dahl model [36–38] has the form

$$\dot{F}_f(t) = \sigma \left| 1 - \frac{F_f(t)}{F_c} \text{sign } \dot{u}(t) \right|^\gamma \text{sign} \left(1 - \frac{F_f(t)}{F_c} \text{sign } \dot{u}(t) \right) \dot{u}(t), \tag{1.23}$$

where F_f is the friction force, u is the relative displacement between the two surfaces in contact, $F_c > 0$ is the Coulomb friction force, $\gamma \geq 0$ is a parameter that determines the shape of the force-displacement curve, and $\sigma > 0$ is the rest stiffness, that is, the slope of the force-deflection curve when $F_f = 0$. The right-hand side of (1.23) is Lipschitz continuous in F_f for $\gamma \geq 1$ but not Lipschitz continuous in F_f for $0 \leq \gamma < 1$.

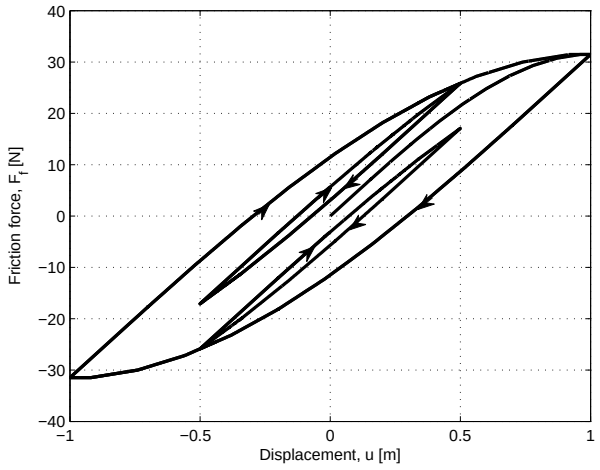

(a)

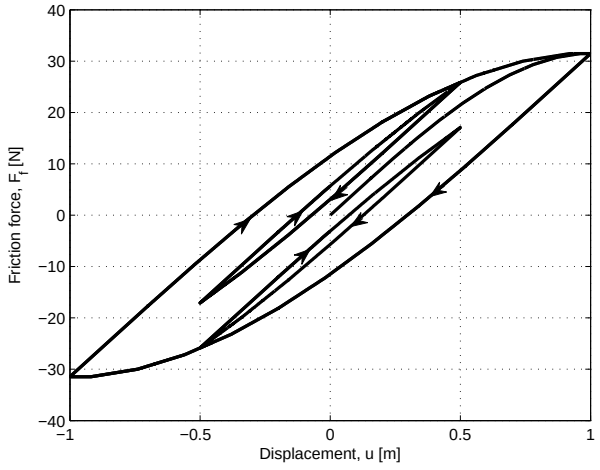

(b)

Figure 1.7: Input-output maps of the Maxwell-Slip model (1.20), (1.21) with $N = 10$, $\Delta = [1.5, 2.4, 3.3, 4.2, 5.1, 6, 6.9, 7.8, 8.7, 9.6] \times 10^{-1}$ m, and $k = [1, 1.8, 2.6, 3.4, 4.2, 5, 5.8, 6.6, 7.4, 8.2]$ N/m. In (a) the frequency of the input is $\omega = 2$ rad/s, and in (b) $\omega = 0.1$ rad/s. The input $u(t)$ is initially $u_1(t) = \sin(\omega t)$ m, where the friction force corresponds to the major loops. When $u(t)$ changes to $u_2(t) = 0.5\sin(\omega t)$ m after one period, the friction force F_f corresponds to the upper minor loops. When $u(t)$ changes to $u_2(t)$ after one and a half periods, the friction force F_f corresponds to the lower minor loops.

As shown in Figure 1.8, the parameter γ determines the shape of the hysteresis map.

The magnitude of the friction force $F_f(t)$ approaches F_c under monotonic inputs.

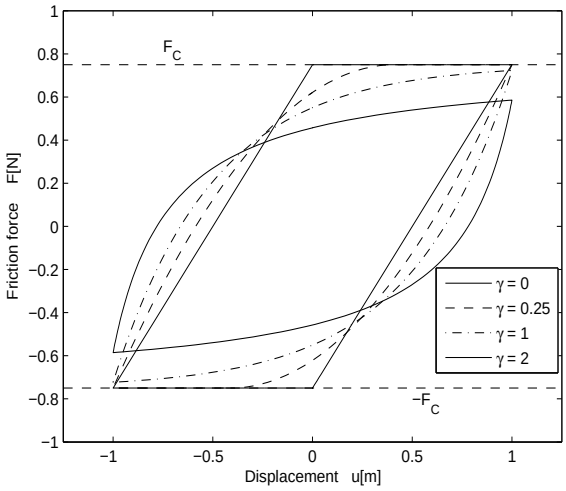

Figure 1.8: Displacement u versus friction force F for hysteresis maps of the Dahl model for several values of γ. The shape of the hysteresis map from u to F depends on the value of γ. The numerical values used are $F_c = 0.75$ N, $\sigma = 1.5$ N/m, and $u(t) = \sin 0.1t$ m.

Figure 1.9 shows the input-output maps of the Dahl model (1.23) for sinusoidal input with frequency $\omega = 2$ rad/s (Figure 1.9(a)) and $\omega = 0.1$ rad/s (Figure 1.9(b)) with $F_c = 1.5$ N, $\sigma_0 = 7.5$ N/m, and $\gamma = 1$. The shape of the input-output map is independent of the input frequency, and thus, the Dahl model (1.23) is rate independent. The input $u(t)$ is initially $u_1(t) = 5\sin(\omega t)$ and the friction force corresponds to the major loops in figures 1.9(a) and 1.9(b). When the input changes to $u_2(t) = \sin(\omega t)$ after one period the friction force corresponds to the minor loops in figures 1.9(a) and 1.9(b). Furthermore, when the input changes from u_1 to u_2 after one and a half periods, the friction force also corresponds to the minor loops in figures 1.9(a) and 1.9(b). Thus, with identical inputs but with different initial conditions, (1.23) results in identical hysteresis maps and therefore Dahl model has local memory.

1.3.4 LuGre Model

The LuGre model [26–28], which models the asperities of two surfaces as elastic bristles, is given by

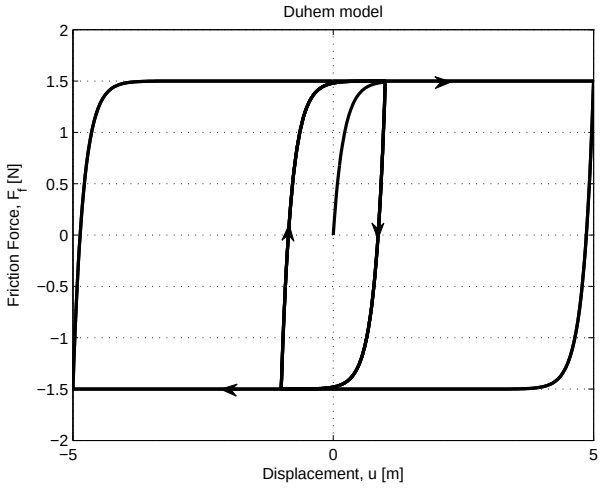

(a)

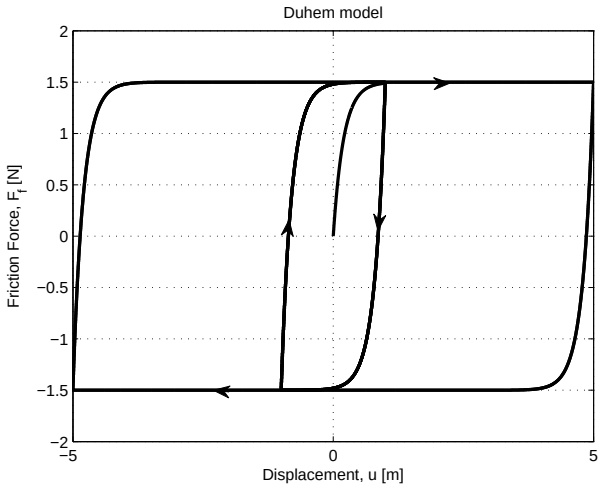

(b)

Figure 1.9: Input-output maps of the Dahl model (1.23) with $F_c = 1.5$ N, $\sigma_0 = 7.5$ N/m, and $\gamma = 1$. In (a) the frequency of the input is $\omega = 2$ rad/s, and in (b) $\omega = 0.1$ rad/s. The input $u(t)$ is initially $u_1(t) = 5\sin(\omega t)$ m and the friction force corresponds to the major loops. When the $u(t)$ changes to $u_2(t) = \sin(\omega t)$ m the friction force F_f corresponds to the minor loop regardless of whether the input change happens after one or one and a half periods.

$$\dot{z}(t) = \dot{u}(t) - \frac{|\dot{u}(t)|}{z_{ss}\big(\dot{u}(t)\big)} z(t), \tag{1.24}$$

$$F(t) = \sigma_0 z(t) + \sigma_1 \dot{z}(t) + \sigma_2 \dot{u}(t), \tag{1.25}$$

where z is the average deflection of the bristles, u is the relative displacement, F_f is the friction force, and $\sigma_0, \sigma_1, \sigma_2 > 0$ are stiffness, damping, and viscous friction coefficients, respectively. The right hand side of (1.24) is Lipschitz continuous with respect to z.

In [2, 27], $z_{ss}(\dot{u}(t))$ is defined by

$$z_{ss}(\dot{u}(t)) = \frac{1}{\sigma_0}\left(F_c + (F_s - F_c)e^{-(\dot{u}(t)/v_s)^2}\right), \tag{1.26}$$

where $F_c > 0$ is the Coulomb friction force, F_s is the stiction force, and v_s is the Stribeck velocity. For a given constant velocity $\dot{u}$, the steady-state friction force $F_{\rm ss}$ obtained from (1.24) and (1.25) is

$$F_{\rm ss}(\dot{u}) = \sigma_0 z_{ss}(\dot{u})\mathrm{sign}(\dot{u}) + \sigma_2 \dot{u}. \tag{1.27}$$

The drop in friction force (see Figure 1.10) at low magnitudes of velocity is due to the Stribeck effect, while the Stribeck velocity is the velocity at which the steady-state friction force begins to decrease when the velocity is positive and increasing.

Letting $F_s = F_c$ in (1.26) and $\sigma_1 = \sigma_2 = 0$ in (1.25), the LuGre model (1.24)-(1.26) is equivalent to the Dahl model (1.23) with $\gamma = 1$ and $\sigma = 1$. Figure 1.11 shows the input-output maps of the LuGre model (1.24)-(1.26) with $F_c = 1$ N, $F_s = 1.5$ N, $\sigma_0 = 10^4$ N/m, and $\sigma_1 = \sqrt{10^4}$ N-s/m, $\sigma_2 = 0.6$ N-s/m, $v_s = 0.04$ m/s, and $u(t) = 5\cos(\omega t)$. In Figure 1.11(a) the input frequency is $\omega = 0.25$ rad/s and in Figure 1.11(b) the input frequency is $\omega = 0.01$ rad/s. Since the shape of the input-output map changes with frequency, the LuGre model is rate dependent.

As noted in [78] the LuGre model has local memory. Thus the hysteresis map $\mathcal{H}_\infty(u, \boldsymbol{x}_0)$ of the LuGre model is independent of $\boldsymbol{x}_0$.

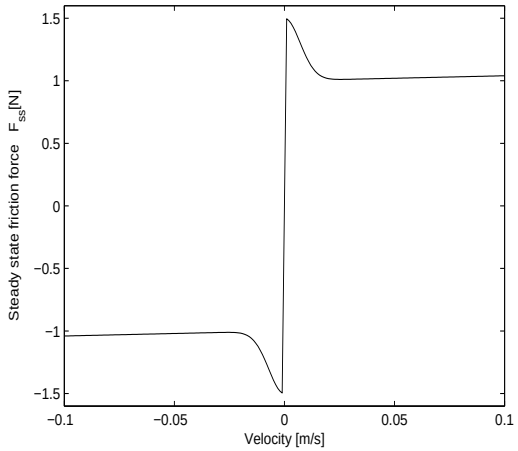

Figure 1.10: Steady-state friction force (1.27) of the LuGre model. The drop in the friction force at low velocities is the Stribeck effect, while the Stribeck velocity $v_S = 0.001$ m/s is the velocity at which the steady-state friction force begins to decrease when the velocity is positive and increasing. The numerical values are $F_c = 1$ N, $F_s = 1.5$ N, $v_s = 0.001$ m/s, $\sigma_0 = 10^5$ N/m, $\sigma_1 = \sqrt{10^5}$ N-s/m, and $\sigma_2 = 0.4$ N-s/m.

1.4 Dissertation Outline

In this dissertation, the goal is to use mechanical elements such as masses, springs and dashpot and observe the frictional phenomena and hysteresis arise from their interaction. In particular we are interested in discovering the mechanical mechanisms that lead to hysteretic energy dissipation, stick-slip and the Stribeck effect. Stick-slip is a friction induced limit cycle in which a body sliding on a surface periodically comes to rest. The Stribeck effect is the apparent drop in the friction force as the velocity increases. In order to investigate these phenomena, we build several hysteretic models in hopes that a better understanding of these processes leads to a better understanding and prediction of friction. If the origins of stick-slip and the Stribeck effect are understood, then this knowledge can be applied in development of experimentally based models, so that they can predict a broad spectrum of behaviors.

A short summary of all of the models presented in this dissertation is shown in Table 1.3. Table 1.3 also states the insights gained from the development of the model

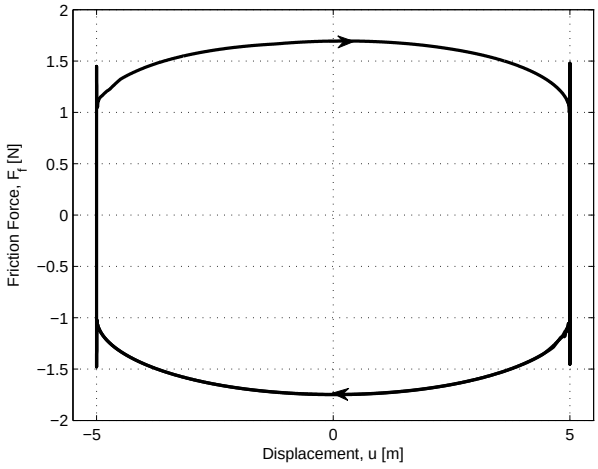

(a)

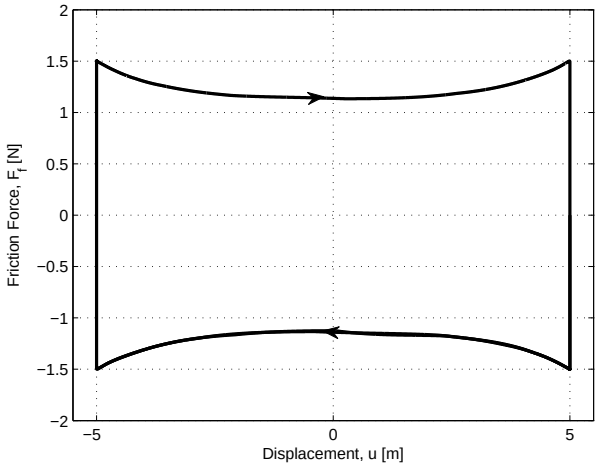

(b)

Figure 1.11: Input-output maps of the LuGre model (1.23) with $F_c = 1$ N, $F_s = 1.5$ N, $\sigma_0 = 10^4$ N/m, and $\sigma_1 = \sqrt{10^4}$ N-s/m, $\sigma_2 = 0.6$ N-s/m, $v_s = 0.04$ m/s, and $u(t) = 5\cos(\omega t)$. In (a) the frequency of the input is $\omega = 0.25$ rad/s, and in (b) $\omega = 0.01$ rad/s.

as well as whether the model is an original contribution of this dissertation or not. The major contributions of this dissertation include the multiplay model for symmetric hysteresis. This model is invertible which is helpful in control design in systems where hysteresis is detrimental to the performance. Discontinuous rotating bristle model (DRBM) gives insight into the origins of hysteretic energy dissipation and the

origins of stick-slip. The compressed bristle model reveals the physical mechanism which leads to the Stribeck effect.

Friction Model	Description / Insights gained	Original Contribution
Maxwell-slip	Models friction with nonlocal memory	No
Dahl	Models friction with local memory	No
LuGre	Exhibits stick-slip and Stribeck effect	No
Multiplay	Has nonlocal memory, invertible, physical representation of Maxwell-Slip model	Yes
Rotating Bristle	Exhibits quasi stick-slip	Yes
DRBM	Physical mechanism for stick-slip and hysteretic energy dissipation	Yes
Compressed Bristle	Physical mechanism for Stribeck effect and physical representation of LuGre model	Yes

Table 1.3: Summary of the friction models developed or described in this dissertation and classification of original contributions of this dissertation.

The contents of this dissertation are as follows. In Chapter II, we consider the multiplay model for hysteresis with nonlocal memory. This new model consists of N mass/spring/dashpot-with-deadzone elements. The hysteresis map of the multiplay model is completely determined by the stiffness coefficients and widths of the gaps of the mass/spring/dashpot-with-deadzone elements. This multiplay model can be used to model a hysteretic system with a hysteresis map possessing the symmetry of the cyclic rotation group C_2. Parameters of the multiplay model can be determined based on the slope of the sampled hysteresis map. Once the multiplay model is determined, its inverse can be analytically computed.

In Chapter III, we investigate the origins of stick-slip friction by developing an asperity-based friction model based on the frictionless contact between a body and a row of rigid, rotating bristles attached to the ground by torsional springs and dashpots. This model exhibits hysteresis and quasi-stick-slip behavior. The hysteretic energy-dissipation mechanism is the release of the pivoted bristles, after which the bristles oscillate and the stored energy is dissipated by the dashpot. The discontinuous rotating bristle model is an approximation of the rotating bristle model that exhibits exact stick-slip and hysteresis. We derive a single-state formulation of the discontinuous rotating bristle model and investigate similarities to the LuGre model.

In Chapter IV we investigate the origin of the Stribeck effect. We develop an asperity-based friction model and show that the vertical motion of the body leads to the Stribeck effect. The friction model is hysteretic, and the energy-dissipation mechanism of the bristle model is the release of the compressed bristles, which causes the bristles to oscillate and the energy is dissipated by a dashpot. We also show that the compressed bristle model is a generalization of the LuGre model, and we derive the LuGre model equations from the compressed bristle model equations.

The contribution of the Chapter V is a framework for relating butterfly-shaped hysteresis maps to simple (single-loop) hysteresis maps, which are typically easier to model and more amenable to control design than the butterfly-shaped loops. In particular, a unimodal mapping is used to transform simple loops to butterfly loops. For the practically important class of piecewise-monotone hysteresis maps, we provide conditions for producing butterfly-shaped maps and examine the properties of the resulting butterflies. Conversely, we present conditions under which butterfly-shaped maps can be converted to simple piecewise monotone hysteresis maps to facilitate hysteresis compensation and control design. Examples of a preloaded two-bar linkage mechanism and a magnetostrictive actuator illustrate the theory and its utility for understanding, modeling, and controlling systems with butterfly-shaped hysteresis.

CHAPTER II

A Multiplay Model for Rate-Independent and Rate-Dependent Hysteresis with Nonlocal Memory

In this chapter we introduce the multiplay model for hysteresis with nonlocal memory. This model consists of N mass/spring/dashpot with deadzone elements. The hysteresis map of the multiplay model is completely determined by the stiffness coefficients and widths of the gaps of the mass/spring/dashpot with deadzone elements. This multiplay model can be used to model a hysteretic system with a hysteresis map possessing the symmetry of the cyclic rotation group C_2. Parameters of the multiplay model can be determined based on the slope of the sampled hysteresis map. Once the multiplay model is determined, its inverse can be analytically computed.

2.1 Introduction

Hysteresis is manifested as a non-vanishing input-output loop for inputs at asymptotically low frequency. This phenomenon arises in nonlinear systems with multiple attracting equilibria. In the limit of DC operation, the output is attracted to different equilibria depending on the direction of the input, which results in a nontrivial input-output loop called the *hysteresis map* [39, 79].

Several types of models can capture hysteretic behavior. Duhem and nonlinear

feedback models are finite dimensional. Differential equations of Duhem models involve derivatives of the input [55, 66]. Various types of Duhem models including Maxwell-slip are described in [22]. Nonlinear feedback models consist of a linear system with a feedback nonlinearity [63]. Preisach and Prandtl-Ishlinskii models, which are infinite dimensional, consist of an infinite number of hysterons or unitary hysteresis operators, which are turned on or off depending on the current direction of the input [64]. The Prandtl-Ishlinskii model, which is a special type of the Preisach model, utilizes the play operators weighted by a density function [66, 70–72].

If the shape of the hysteresis map changes with the frequency of the input, the model is said to be *rate dependent*. If the shape of the hysteresis map is identical for all frequencies of the input, the model is *rate independent* (see Definition 1.1.6). Nonlinear feedback models are rate dependent [63], Preisach and Prandtl-Ishlinskii models are rate independent [72] and can be extended to rate dependent [80], and Duhem models can be either rate independent or rate dependent [22].

Some hysteresis models have nonlocal memory, that is, the shape and position of the hysteresis map depend on the initial conditions. Nonlocal memory is manifested as the existence of congruent minor loops corresponding to input reversals (see Definition 1.1.5) [22, 81]. Infinite dimensional Preisach and Prandtl-Ishlinskii models capture this property [64, 70]. However, we introduce a finite-dimensional nonlinear feedback model with nonlocal memory called the multiplay model. This rate-dependent model is equivalent to the Maxwell-slip model in the limit of DC operation and can be analytically inverted which makes it suitable for real-time applications.

In this chapter, we first demonstrate that the multiplay model is a rate-dependent model with nonlocal memory. Second, we make the connection between the Maxwell-slip model and the nonlinear feedback model. Third, we extend the Maxwell-slip model by introducing negative stiffness coefficients, which give greater flexibility to the shape of the hysteresis map. Next, we present a method for fitting the nonlinear

feedback model to hysteresis maps possessing the symmetry of the cyclic rotation group C_2. Finally, we introduce a simple algorithm for analytically inverting a given hysteresis map.

2.2 Multiplay

Consider the mass/spring/dashpot system with deadzone shown in Figure 2.1. This system consists of a body with mass m, a spring with stiffness k, a dashpot with damping coefficient c, and a deadzone of width 2Δ. The input $u(t)$ is the position of the right end of the spring, and the output $x(t)$ is the position of the mass. The system is modeled by the differential equation

$$m\ddot{x}(t) + c\dot{x}(t) + kd_{2\Delta}\big(x(t) - u(t)\big) = 0, x(0) = x_0, \quad t \geq 0, \tag{2.1}$$

where

$$d_{2\Delta}(v) \triangleq \begin{cases} v - \Delta, & v \geq \Delta, \\ 0, & |v| < \Delta, \\ v + \Delta, & v \leq -\Delta \end{cases} \tag{2.2}$$

is the deadzone function with width $2\Delta \geq 0$.

The mass/spring/dashpot system with deadzone in Figure 2.1 can be represented as in Figure 2.2, where the mass with deadzone is replaced by the play operator discussed in [82]. In the present chapter we work directly with the model (2.1) rather than the play operator.

Next, we define *multiplay* as the parallel connection of N mass/spring/dashpot systems with deadzone shown in Figure 2.3. The multiplay system has N masses, N play operators with widths $2\Delta_i$, N springs with stiffness coefficients k_i, and N dash-

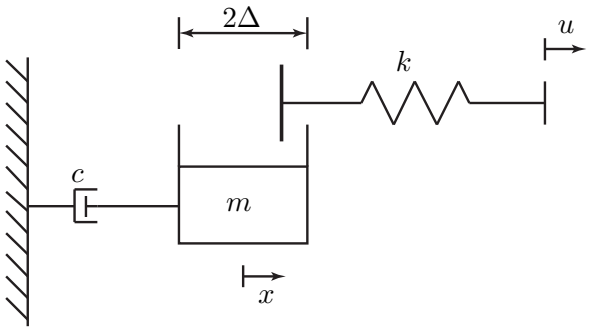

Figure 2.1: Mass/spring/dashpot system with deadzone. The input u is the position of the right end of the spring, and output x is the position of the mass. The system is modeled by (2.1) and the deadzone is modeled by (2.2).

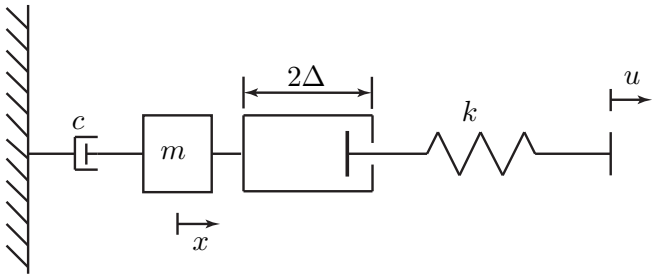

Figure 2.2: Play operator representation of the mass/spring/dashpot with deadzone system. The deadzone is replaced by the play operator of width 2Δ.

pots with damping coefficients c_i. The mass/spring/dashpot with deadzone elements are connected by a rigid bar. The input to the multiplay system is the position $u(t)$ of the bar. Each element is modeled by the differential equation

$$m_i\ddot{x}_i(t) + c_i\dot{x}_i(t) + k_i d_{2\Delta_i}\big(x_i(t) - u(t)\big) = 0, \tag{2.3}$$
$$x_i(0) = x_{i0}, \quad t \geq 0, \quad i = 1, \ldots, N,$$

where $d_{2\Delta_i}(\cdot)$ is the deadzone function defined by (2.2). The output of the system is defined as

$$y(t) = \sum_{i=1}^{N} k_i(u(t) - x_i(t)). \tag{2.4}$$

Physically, $y(t)$ represents the sum of spring forces in the multiplay system. We allow the stiffness coefficients and masses to be negative. We call (2.3)-(2.4) the multiplay model, and we omit units since we do not physically construct this system.

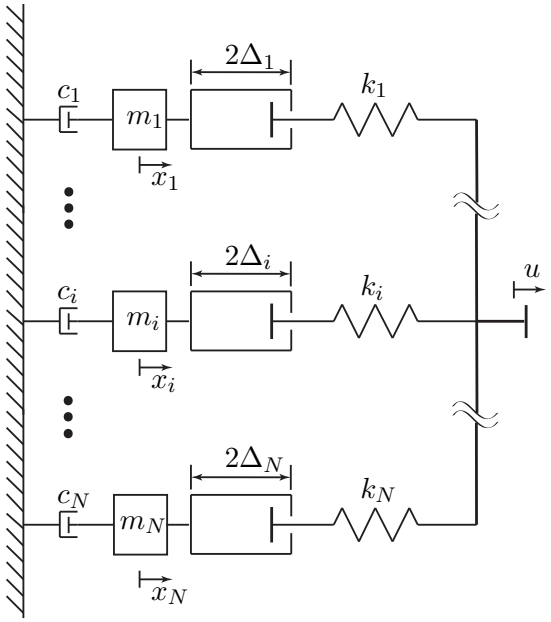

Figure 2.3: A schematic representation of the multiplay system consisting of N mass/spring/dashpot with deadzone elements. The elements are connected in parallel by a rigid bar.

The periodic input-output maps $\mathcal{H}_T(u_T, y_T)$ as defined by Definition 1.1.3, of the multiplay model converge to a hysteretic map $\mathcal{H}_\infty(u, x_0)$ as the frequency of the periodic input approaches zero as shown in Figure 2.4. This figure shows the input-output response of a multiplay model with two elements. For simplicity all masses are set to $m_i = 1$, all stiffness coefficients to $k_i = 1$, all damping coefficients to $c_i = 1$, and the deadzone widths to $\Delta_1 = 0.8$ and $\Delta_2 = 0.2$. Furthermore, the multiplay model in Figure 2.4 has nonlocal memory. When the direction of the input is reversed after either a half or a full period, the output converges to two distinct trajectories.

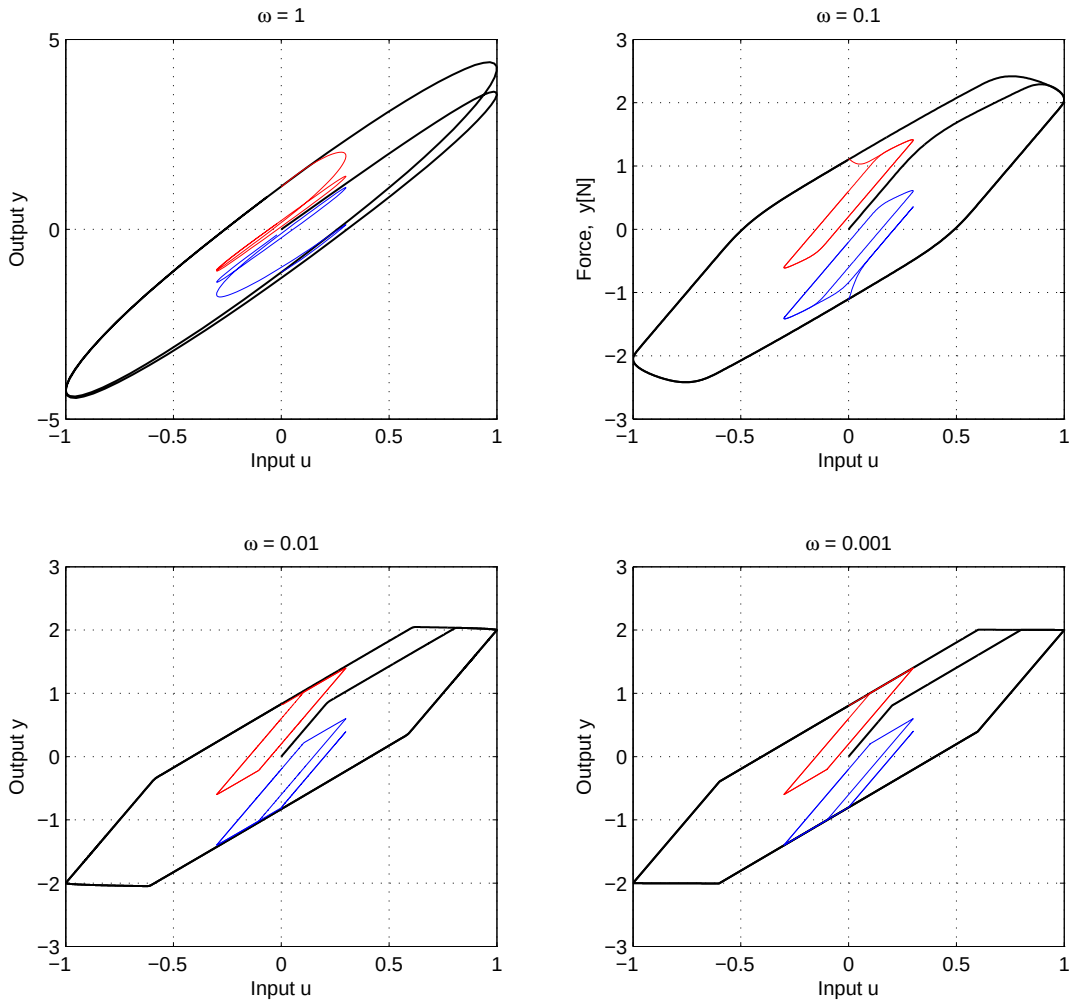

Figure 2.4: Periodic input-output maps $\mathcal{H}_T(u_T, y_T)$ of the multiplay model. As the frequency of the input approaches zero the periodic input-output map approaches a hysteretic map $\mathcal{H}_\infty(u, x_0)$ with nonlocal memory. This hysteretic system is rate dependent.

2.3 Multiplay and Maxwell-Slip Model

In this section we explore the relationship between the multiplay model and the Maxwell-slip model. We begin by taking the time derivative of (2.3)

$$m_i \dddot{x}_i(t) + c_i \ddot{x}_i(t) = k_i d'_{2\Delta_i}\big(u(t) - x_i(t)\big)\big(\dot{u}(t) - \dot{x}_i(t)\big). \tag{2.5}$$

In the limit, as the period of the input approaches infinity, the dynamics in (2.3) become negligible. The effective mass and damping coefficient are zero, and (2.5) becomes

$$d'_{2\Delta_i}\big(u(t) - x_i(t)\big)\big(\dot{u}(t) - \dot{x}_i(t)\big) = 0, \tag{2.6}$$

which means that either

$$\dot{x}_i(t) = \dot{u}(t) \tag{2.7}$$

or

$$d'_{2\Delta_i}\big(u(t) - x_i(t)\big) = 0. \tag{2.8}$$

Note that the derivative of the deadzone function (2.2) for $v = -\Delta_i$ and $v = \Delta_i$ is equal to the δ function. Defining the derivative to be 1 at these two points for convenience, we have

$$d'_{2\Delta_i}(v) = \begin{cases} 1, & v \leq -\Delta_i, \\ 0, & |v| < \Delta_i, \\ 1, & v \geq \Delta_i, \end{cases} \tag{2.9}$$

so that (2.8) holds if and only if

$$|u(t) - x_i(t)| < \Delta_i. \tag{2.10}$$

If (2.10) holds, the end of the spring inside the play element is not in contact with either the left or right wall of the play operator. Thus, the position of the mass is not changing since the end of the spring is neither pushing nor pulling on the play

operator. In other words, $|u(t) - x_i(t)| < \Delta_i$ corresponds to $\dot{x}_i(t) = 0$. Now, (2.7) corresponds to $u(t) - x_i(t) \leq -\Delta_i$ and $u(t) - x_i(t) \geq \Delta$. If $u(t) - x_i(t) \leq -\Delta_i$ the left end of the spring is pushing on the left wall of the play operator and $u(t)$ is decreasing. If $u(t) - x_i(t) \geq \Delta_i$ the left end of the spring is pushing on the right wall of the play operator and $u(t)$ is increasing. Based on this discussion, in the limit, as the period of the input approaches infinity (2.3) is equivalent to

$$\dot{x}_i(t) = \begin{cases} \dot{u}(t), & u(t) - x_i(t) \leq -\Delta_i, \quad \dot{u}(t) < 0, \\ 0, & |u(t) - x_i(t)| < \Delta_i, \\ \dot{u}(t), & u(t) - x_i(t) \geq \Delta_i, \quad \dot{u}(t) > 0. \end{cases} \tag{2.11}$$

Expression (2.11) can be rewritten as

$$\dot{x}_i(t) = \begin{bmatrix} U(u(t) - x_i(t) - \Delta_i) & 1 - U(u(t) - x_i(t) + \Delta_i) \end{bmatrix} \begin{bmatrix} \dot{u}_+(t) \\ \dot{u}_-(t) \end{bmatrix}, \tag{2.12}$$

$$y(t) = \sum_{i=1}^{N} k_i(u(t) - x_i(t)), \tag{2.13}$$

where $U(v)$ is the unit step function

$$U(v) \triangleq \begin{cases} 1, & v \geq 0, \\ 0, & v < 0, \end{cases} \tag{2.14}$$

and $\dot{u}_+(t)$ and $\dot{u}_-(t)$ are defined as

$$\dot{u}_+(t) \triangleq \max\{0, \dot{u}(t)\}, \quad \dot{u}_-(t) \triangleq \min\{0, \dot{u}(t)\}. \tag{2.15}$$

Equation (2.12) is a rate-independent semilinear Duhem model of friction, known as the Maxwell-slip model. Thus, in the limit of DC operation, as the frequency

of the input approaches zero, the multiplay model (2.3)-(2.4) is equivalent to the rate-independent Maxwell-slip model (2.12)-(2.13).

2.4 Determining the Hysteresis Map From the Multiplay Model

In this section we analyze the properties of the limiting periodic input-output map $\mathcal{H}_\infty(u, x_0)$, that is, the periodic input-output map in the limit as the period of the input approaches infinity.

To find the slope of the limiting periodic input-output map, we differentiate (2.4) with respect to the input $u(t)$, that is,

$$\frac{dy}{du} = \sum_{i=1}^{n} k_i(1 - \frac{dx_i}{du}), \tag{2.16}$$

where $\frac{dx_i}{du}$ depends on whether m_i is moving or not. Rewriting $\dot{x}_i(t)$ as

$$\frac{dx_i}{dt} = \frac{dx_i}{du}\frac{du}{dt} = \frac{dx_i}{du}\dot{u} \tag{2.17}$$

and using (2.11), we have

$$\frac{dx_i}{du}\dot{u} = \begin{cases} \dot{u}(t), & u(t) - x_i(t) \leq -\Delta_i, \quad \dot{u}(t) < 0, \\ 0, & |u(t) - x_i(t)| < \Delta_i, \\ \dot{u}(t), & u(t) - x_i(t) \geq \Delta_i, \quad \dot{u}(t) > 0. \end{cases} \tag{2.18}$$

From (2.18) we conclude that

$$\frac{dx_i}{du} = \begin{cases} 1, & |u(t) - x_i(t)| \geq \Delta_i, \\ 0, & |u(t) - x_i(t)| < \Delta_i. \end{cases} \tag{2.19}$$

Substituting (2.19) into (2.16) and assuming that, for $i = 1, \ldots, r$, $|u(t) - x_i(t)| \geq \Delta_i$ and, for $i = r+1, \ldots, N$, $|u(t) - x_i(t)| < \Delta_i$, then

$$\frac{dy}{du} = \sum_{i=1}^{r} k_i(1 - \frac{dx_i}{du}) + \sum_{i=r+1}^{N} k_i(1 - \frac{dx_i}{du}) \tag{2.20}$$

$$= \sum_{i=1}^{r} k_i(1-1) + \sum_{i=r+1}^{N} k_i(1-0) = \sum_{i=r+1}^{N} k_i. \tag{2.21}$$

Once mass m_j starts moving, its stiffness is no longer included in the summation in (2.20), and thus does not affect the slope of the limiting input-output map until the input u reverses direction and moves $2\Delta_j$ in the opposite direction. The slope of the limiting input-output curve changes each time a stationary mass starts moving. Assuming that the input is oscillating between $u_{\min}$ and $u_{\max} > u_{\min} + 2\Delta_N$, if u just reached $u_{\min}$ and is monotonically increasing, none of the masses of the multiplay are moving. The slope of the limiting input-output map, which is equal to the sum of all of the stiffnesses, first changes when u reaches $u_{\min} + 2\Delta_1$. The slope becomes the sum of stiffnesses k_2 through k_N. Next, when u increases past $u_{\min} + 2\Delta_2$ the slope is equal to the sum of stiffnesses k_3 through k_N. In general, each time u becomes larger then $u_{\min} + 2\Delta_i$ the slope decreases by k_i. As the input increases from $u_{\min}$ to $u_{\max}$ the slope changes according to

$$\begin{bmatrix} s_1 \\ s_2 \\ \vdots \\ s_N \end{bmatrix} = A \begin{bmatrix} k_1 \\ k_2 \\ \vdots \\ k_N \end{bmatrix} \tag{2.22}$$

where s_1 is the slope of the section of the hysteresis map that corresponds to $u \in [u_{\min}, u_{\min} + 2\Delta_1]$ and s_i is the slope of the section of the hysteresis map that corresponds to $u \in [u_{\min} + 2\Delta_{i-1}, u_{\min} + 2\Delta_i]$, $i = 2, \ldots, N$, and $A \in \mathbb{R}^{N \times N}$ is given

by

$$A = \begin{bmatrix} 1 & 1 & \cdots & 1 \\ 0 & 1 & \cdots & 1 \\ \vdots & \vdots & \ddots & \vdots \\ 0 & 0 & \cdots & 1 \end{bmatrix}. \tag{2.23}$$

We demonstrate (2.20) based on the limiting input-output map of the two-element multiplay shown in Figure 2.5(a). The stiffnesses are $k_1 = 2$ and $k_2 = 4$, the deadzone widths are $\Delta_1 = 1$ and $\Delta_2 = 3$, and $u_{\min} = -5$ and $u_{\max} = 5$. In the limit of DC operation, the mass and damping coefficient are irrelevant, and we thus set them equal to the corresponding stiffnesses. The transient response is shown by the dashed line. As the arrows indicate, the hysteresis loop is counterclockwise. As u increases from $u_{\min} = -5$ to $u_{\min} + 2\Delta_1 = -3$ the slope of the input-output map is $s_1 = 6 = k_1 + k_2$. At this point, the first mass starts moving and the slope becomes $s_2 = 4 = k_2$. When u increases above $u_{\min} + 2\Delta_2 = 1$, the second mass moves and the slope becomes zero. When u reaches $u_{\max}$ and starts decreasing, the slope follows the same rules; in particular the slope is initially 6, then 4, then 0.

The stiffness coefficients k_i do not have to be limited to positive numbers, which allows the slope of the hysteresis map to be negative and corresponds to a stiffening spring. However, if any of the stiffnesses are negative, the corresponding mass and damping coefficient must also be negative in order for system (2.3)-(2.4) to be stable. Note that the negative masses and damping coefficient do not have a physical meaning, rather they are a tool used to allow for more flexibility in the shape of the hysteresis map. We can introduce the negative masses and damping coefficient since their effect in the limit of DC operation is negligible.

We demonstrate that the hysteresis map has negative slope with negative stiffness coefficients, we use the two-element multiplay in Figure 2.5(b). The stiffness coeffi-

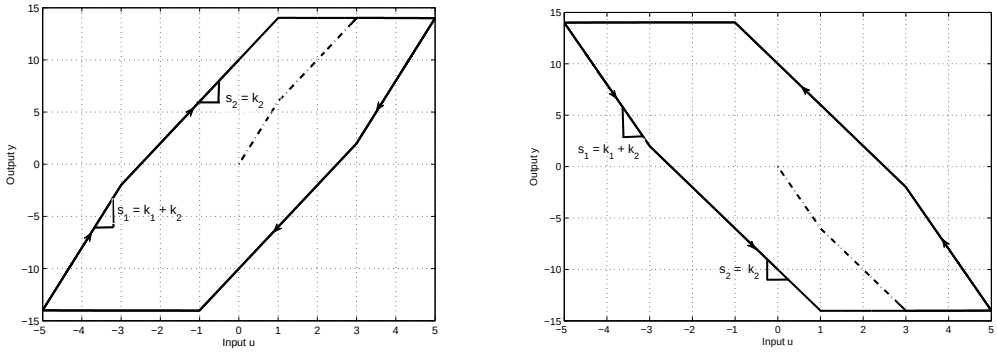

(a) (b)

Figure 2.5: Hysteresis map of the multiplay model with two elements and a) positive and b) negative stiffness coefficients. The slope of the hysteresis map at each point is equal to the sum of the stiffness coefficients corresponding to the stationary masses.

cients are $k_1 = -2$ and $k_2 = -4$. Masses and damping coefficients are equal to the corresponding stiffnesses. All other parameters are the same as in the previous example. The hysteresis map is now counterclockwise, and as u increases from $u_{\min} = -5$ to $u_{\max} = 5$ the slope changes from $s_1 = -6 = k_1 + k_2$, to $s_2 = -4 = k_2$, to $s_3 = 0$.

Positive and negative stiffness coefficients can be combined in the same multiplay model to give S-shaped loops as shown in Figure 2.6. The stiffness coefficients are $k_1 = \cdots = k_5 = -1$ and $k_6 = \cdots = k_{10} = 2$. Masses and damping coefficients are equal to corresponding stiffnesses. Deadzone widths are $\Delta = \begin{bmatrix} 1 & 3 & 5 & 7 & 9 & 11 & 13 & 15 & 17 & 19 \end{bmatrix}'$, where the ith entry of Δ is Δ_i.

2.5 Determining the Multiplay Model From the Hysteresis Map

The multiplay model can be used to approximate a known hysteresis map that is symmetric under a 180° rotation in the input-output plane, that is, having the symmetry of the cyclic rotational group C_2. The hysteresis map is approximated by

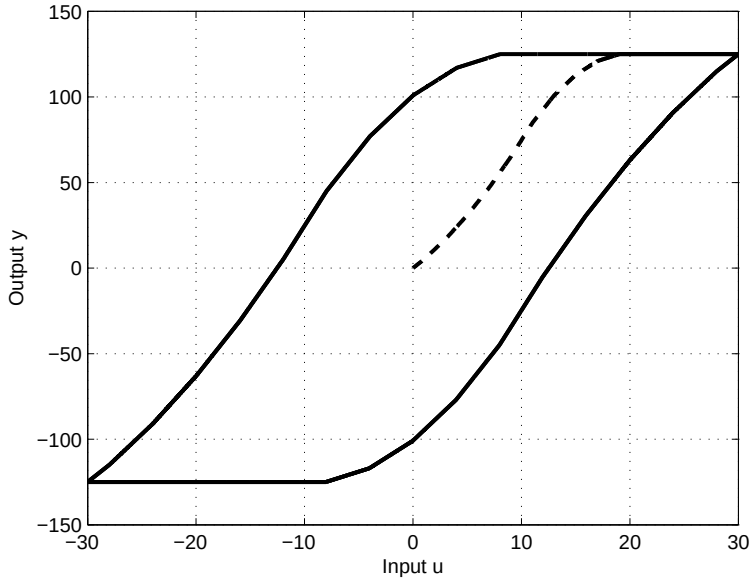

Figure 2.6: S-shaped hysteresis map of a multiplay model with ten elements. The S-shape is the result of a combination of positive and negative stiffness coefficients.

using positive and negative stiffness coefficients to give the desired slope. We divide the hysteresis map into $N+1$ piecewise linear segments, each with slope s_i. Once the slopes are known, the stiffness coefficients can be computed by inverting (2.22). The matrix A in (2.22) is nonsingular for all N and its inverse $A^{-1} \in \mathbb{R}^{N\times N}$ is

$$A^{-1} = \begin{bmatrix} 1 & -1 & 0 & \cdots & 0 \\ 0 & 1 & -1 & \cdots & 0 \\ \vdots & \ddots & \ddots & \ddots & \vdots \\ 0 & \cdots & 0 & 1 & -1 \\ 0 & \cdots & \cdots & 0 & 1 \end{bmatrix}. \tag{2.24}$$

Assuming that the output trajectory from $u_{\min}$ to $u_{\max}$ is partitioned into $N+1$ segments with endpoints $(u_{\min}, y(u_{\min})), (u_1, y(u_1)), \ldots, (u_N, y(u_N)), (u_{\max}, y(u_{\max}))$. The slope of each segment is found from the endpoint coordinates, and the stiffness

coefficients are computed from

$$\begin{bmatrix} k_1 \\ \vdots \\ k_N \end{bmatrix} = A^{-1} \begin{bmatrix} s_1 \\ \vdots \\ s_N \end{bmatrix}, \tag{2.25}$$

where $s_1, \ldots, s_N$ are the slopes of the consecutive segments and the slope s_{N+1} is not used in the calculation. The widths of the deadzones associated with the stiffness coefficients calculated from (2.25) can be found from

$$\begin{bmatrix} \Delta_1 \\ \vdots \\ \Delta_N \end{bmatrix} = \begin{bmatrix} (u_1 - u_{\min})/2 \\ \vdots \\ (u_N - u_{\min})/2 \end{bmatrix} \tag{2.26}$$

The following example is taken from [1]. Note that this hysteresis map has the symmetry of the cyclic group C_2. However, the actual data presented in the chapter are not available, so the "true" hysteresis map was estimated by "extracting" the points $(u_{\min}, y(u_{\min})), (u_1, y(u_1)), \ldots, (u_N, y(u_N)), (u_{\max}, y(u_{\max}))$ from the plot. Stiffness coefficients and deadzone widths are calculated from (2.25) and (2.26), respectively. The estimated and actual hysteresis maps are identical as shown in Figure 2.7.

2.6 Minor Loops of the Multiplay Model

As already stated, the multiplay system has nonlocal memory, which is manifested as existence of external or internal minor loops that correspond to input reversals.

The shape of the minor loops is determined by the stiffness coefficients k_i and the deadzone widths Δ_i of the masses with Δ_i less than the amplitude of the input reversal. After every input reversal, the initial slope of the reversal loop s_{r1} is given

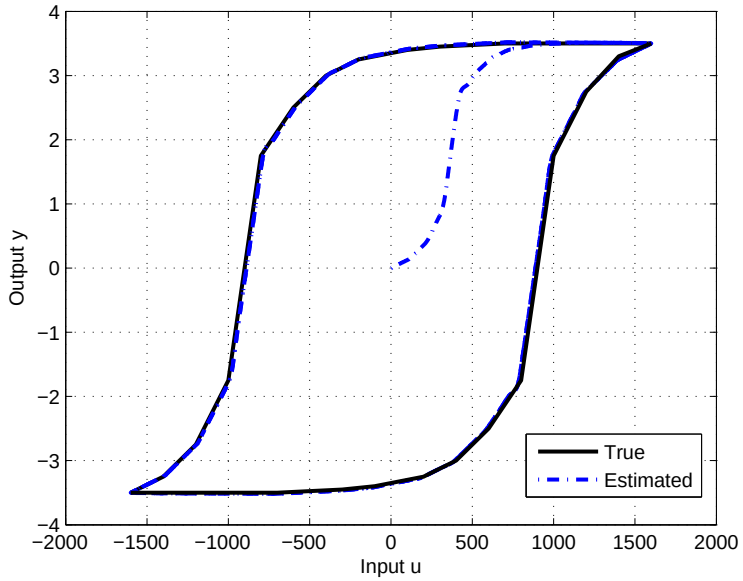

Figure 2.7: True and estimated hysteresis maps from [1]. Note that the hysteresis map is symmetric under 180° rotation in the input-output plane, and that the true and estimated hysteresis maps are identical.

by $s_{r1} = \sum_{i=1}^{N} k_i$.

The slope subsequently changes according to the same rules as described above. When the input reversal occurs at a point of the major loop where the slope of the major loop s_i satisfies $s_i > \sum_{i=1}^{N} k_i$, the minor loop is external. When the reversal happens at the point where the slope of the major loop satisfies $s_i < \sum_{i=1}^{N} k_i$, the minor loop is internal. However, if $s_i = \sum_{i=1}^{N} k_i$, then the minor loop is internal if its slope increases and external if its slope decreases when a stationary mass begins moving.

Minor loops are shown in Figure 2.8. The figure shows the hysteresis map of a multiplay system and the minor loops that correspond to input reversals at different points along the major loop. The multiplay has 10 masses with stiffness coefficients $k_1 = \cdots = k_4 = -2$ and $k_5 = \cdots = k_{10} = 2$. Masses and damping coefficients are equal to corresponding stiffnesses. Deadzone widths are $\Delta =$

$\begin{bmatrix} 1 & 2 & 4 & 6 & 8 & 10 & 12 & 14 & 16 & 18 \end{bmatrix}^{\mathrm{T}}$, where the ith entry of Δ is Δ_i.

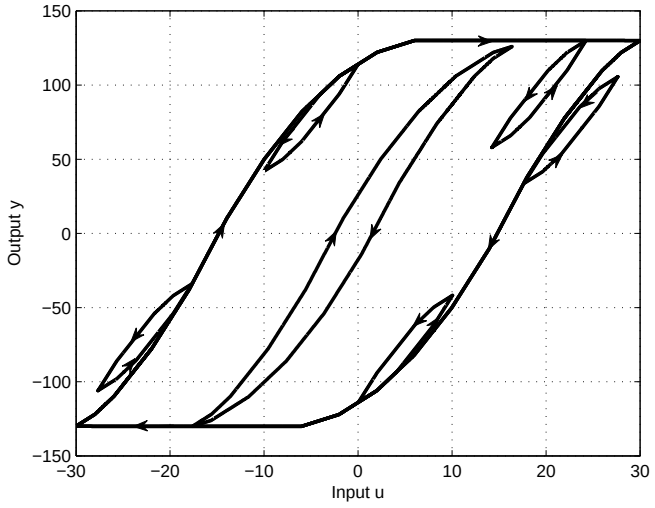

Figure 2.8: Internal and external minor loops of an S-shaped multiplay hysteresis map. The major and the large minor loop are clockwise while the small minor loops are counterclockwise.

2.7 Inverse of the Multiplay Model

In this section we develop the strategy for computing the inverse of a multiplay model with a known hysteresis map. The slopes s_i' of the inverse hysteresis map are

$$s_i' = \frac{1}{s_i}, \quad s_i \neq 0, \tag{2.27}$$

where s_i is defined in (2.25). The stiffness coefficients k_i' of the inverse hysteresis map are calculated from s_i' as in (2.25)

$$\begin{bmatrix} k_1' \\ \vdots \\ k_N' \end{bmatrix} = A^{-1} \begin{bmatrix} s_1' \\ \vdots \\ s_N' \end{bmatrix}. \tag{2.28}$$

To find the new deadzone widths Δ'_i, we use the points $y(u_{\min}), \ldots, y(u_N)$ similarly to (2.26)

$$\begin{bmatrix} \Delta'_1 \\ \vdots \\ \Delta'_N \end{bmatrix} = \begin{bmatrix} (y(u_1) - y(u_{\min}))/2 \\ \vdots \\ (y(u_N) - y(u_{\min}))/2 \end{bmatrix}. \tag{2.29}$$

One shortcoming of the inverse model obtained through this procedure is that it cannot handle the segments of infinite slope. The inverse hysteresis map of the one in Figure 2.6 is shown in Fig 2.9. Note that the inverse hysteresis maps are counterclockwise. The true and estimated hysteresis maps differ only in the vertical segments with infinite slope. However, if the segment of the estimated inverse that corresponds to the decreasing input is shifted up and the segment of the estimated inverse that correspond to the increasing input is shifted down, then the resulting hysteresis map matches the actual inverse hysteresis map.

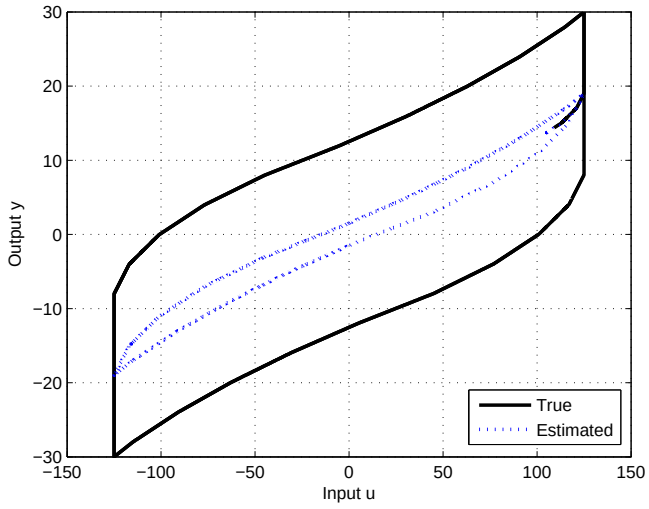

Figure 2.9: True and estimated inverse hysteresis maps. Note that the estimated hysteresis map defers from the true only in the vertical segments with infinite slope.

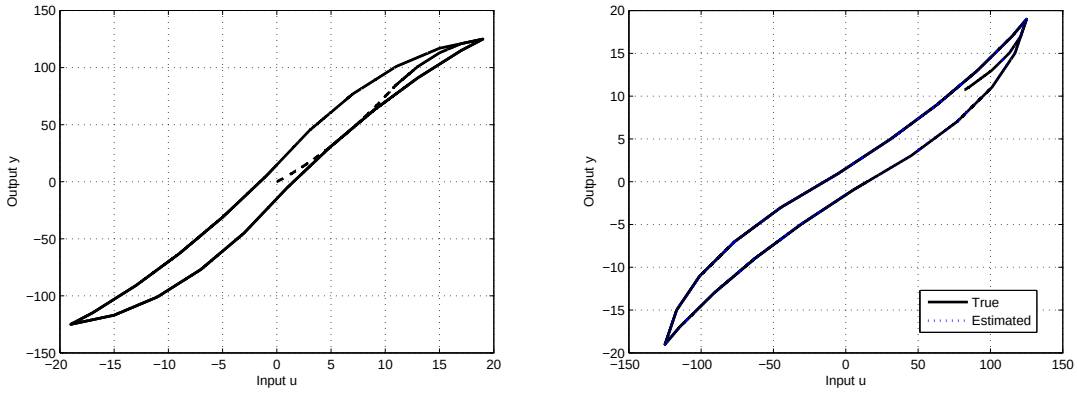

(a) (b)

Figure 2.10: Inversion of a hysteresis map without segments having zero slope. The true hysteresis map is shown in a), while its true and estimated inverse is shown in b).

The inverse model obtained from (2.27)-(2.29) will give much better results if the original hysteresis map has no zero-slope segments. Figure 2.10(a) shows a hysteresis map of a multiplay with 10 masses. The stiffness coefficients are $k_1 = \cdots = k_5 = -1$ and $k_6 = \cdots = k_{10} = 2$. Masses and damping coefficients are $m_1 = \cdots = m_5 = -1$ kg, $m_6 = \cdots = m_{10} = 2$ kg, $c_1 = \cdots = c_5 = -1$ N-m/s, $c_6 = \cdots = c_{10} = 2$ N-m/s, respectively. Deadzone widths are $\Delta = \begin{bmatrix} 1 & 3 & 5 & 7 & 9 & 11 & 13 & 15 & 17 & 19 \end{bmatrix}'$, where the ith entry of Δ is Δ_i. The true and estimated inverses of this hysteresis map are shown in Figure 2.10(b). The true and estimated inverse are now identical.

2.8 Alternative Inverse of the Multiplay Model

In this section we develop an alternative strategy for computing the inverse of any multiplay model given input stiffness coefficients k_i, deadzone widths Δ_i, and the output $y(t)$. If the k_i's and Δ_i's are not given initially, they can be computed through the procedure outlined in Section 2.5. Starting with (2.4) the input $u(t)$ can

be expressed as

$$u(t) = \frac{y(t) + \sum_{j=1}^{N} k_j x_j(t)}{\sum_{j=1}^{N} k_j}, \quad \sum_{j=1}^{N} k_j \neq 0. \tag{2.30}$$

Substituting (2.30) into (2.3) we get

$$m_i \ddot{x}_i(t) + c_i \dot{x}_i(t) + k_i d_{2\Delta_i}\left(x_i - \frac{y + \sum_{j=1}^{N} k_j x_j}{\sum_{j=1}^{N} k_j}\right) = 0. \tag{2.31}$$

Introducing the change of variables $\bar{u}(t) = y(t)$ and $\bar{y}(t) = u(t)$ in (2.31) gives a new system

$$\begin{aligned} m_i \ddot{x}_i(t) + c_i \dot{x}_i(t) + k_i d_{2\Delta_i}\left(x_i(t) - \frac{\bar{u}(t) + \sum_{j=1}^{N} k_j x_j(t)}{\sum_{j=1}^{N} k_j}\right) = 0, \\ x_i(0) = x_{i0}, \quad t \geq 0, \quad i = 1, \ldots, N, \quad \sum_{j=1}^{N} k_j \neq 0, \end{aligned} \tag{2.32}$$

with the output

$$\bar{y}(t) = \frac{\bar{u}(t) + \sum_{j=1}^{N} k_j x_j(t)}{\sum_{j=1}^{N} k_j}, \quad \sum_{j=1}^{N} k_j \neq 0. \tag{2.33}$$

Figure 2.11 shows the inverse of the hysteresis loop displayed in Figure 2.6. The output of the multiplay shown in Figure 2.6 is used as the input $\bar{u}(t)$ in (2.32)-(2.33). Stiffness coefficients, masses, damping coefficients, and deadzone widths remain the same. The actual inverse is also shown for comparison.

2.9 Conclusions

In this chapter we introduced the multiplay model of hysteresis, which consists of a parallel connection of mass/spring/dashpot with deadzone elements. This hysteresis model has nonlocal memory. Multiplay model is used to recreate a known hysteresis

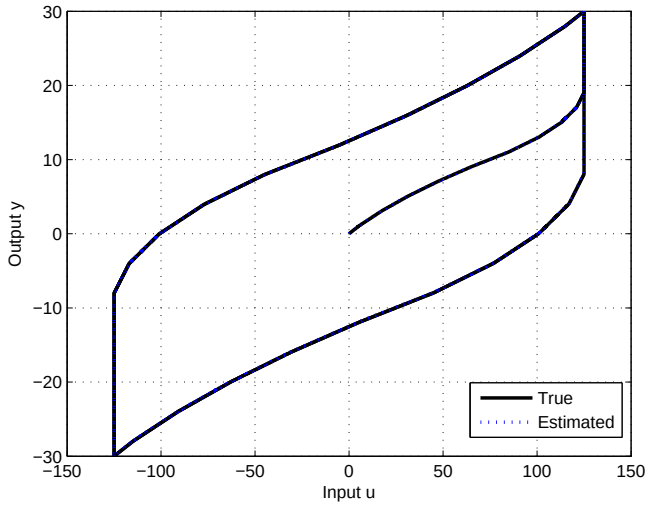

Figure 2.11: True and recreated inverse hysteresis maps. The inverse is computed from (2.32)-(2.33) based on the known $u(t)$ and $y(t)$.

map. Parameters of the multiplay model can be determined based on the slope of the desired hysteresis map. We also present an algorithm for inversion of the hysteresis map of the multiplay. The multiplay model is a useful tool in control engineering since it can be used to model a hysteresis map which is symmetrical under 180 degree rotation. Furthermore, since this model is invertible, it can be used to cancel out hysteresis in a given system and allow for easier control.

CHAPTER III

A Frictionless Bristle-Based Friction Model That Exhibits Hysteresis and Stick-Slip Behavior

In this chapter, we investigate the origins of stick-slip friction by developing an asperity-based friction model based on the frictionless and lossless contact between a body and a row of rigid, rotating bristles attached to the ground by torsional springs and dashpots. This model exhibits hysteresis and quasi-stick-slip friction. The hysteretic energy-dissipation mechanism is the sudden release of the compressed bristles, after which the bristles oscillate and the stored energy is dissipated by the dashpot. The discontinuous rotating bristle model is an approximation of the rotating bristle model that exhibits exact stick-slip and hysteresis. We derive a single-state formulation of the discontinuous rotating bristle model and investigate similarities to the LuGre model. The purpose of this chapter is to understand the physical mechanism that leads to hysteretic energy dissipation and stick-slip friction. We investigate these phenomena in hopes that a better understanding of these processes leads to a better understanding and prediction of friction. If the origins of stick-slip are known, then this knowledge can be applied in development of experimentally based models, so that they can predict a broad spectrum of behaviors.

3.1 Introduction

Modeling and control of systems with friction remains a challenging and practically important problem in science and engineering [2–4, 6, 9, 83]. Excessive friction contributes to wasted energy measured in billions of dollars, whereas insufficient friction contributes to accidents. In manufacturing applications, friction is crucial to grinding and polishing, and it is a limiting factor in achieving precision motion control. In scientific applications, such as atomic force microscopes and nano-scale devices, friction plays a crucial role [84]. A better understanding of friction is essential for improved design, analysis, and prediction.

Experimental observations provide the primary approach to understanding how friction depends on material properties and the relative motion between contacting surfaces [8, 20, 21]. Based on these studies, various empirical models have been developed to capture the macroscopic properties of friction [6, 22–30]. These models can be fit to data for a specific application, or they can be used for adaptive control, where parameters are identified and controller gains are updated during operation [24, 78, 85, 86]. As discussed in [87], empirical friction models are typically based on an internal state variable, denoted by z, that reflects the internal friction mechanism.

The approach we take to modeling friction is motivated by bristle models [5, 31, 32], where the bristles represent the asperities, which determine the macroscopic roughness of the contact surfaces. As the contacting surfaces slide over each other, their asperities touch and are deformed due to shear stresses. Energy is dissipated as the asperities deform and change the shape of the contacting surfaces [6].

The unconventional aspect of the bristle model in the present chapter is that the interface between the bristles and the contacting body is frictionless and lossless. The goal of this work is thus to discover how friction and the related phenomenon of hysteresis can emerge from friction-free characteristics. To do this, we construct a

hysteretic dissipation mechanism without introducing friction per se. In particular, we assume that each rigid bristle is connected to a spring and a dashpot. As the moving body comes into contact with each bristle, the bristle is deflected and reaction forces occur, but otherwise the contact is lossless and thus frictionless. As the moving body passes beyond a bristle, the bristle is suddenly released, and the potential energy stored in the spring is dissipated by a dashpot regardless of how slowly the body moves. The resulting model is thus hysteretic in the sense that energy dissipation occurs under asymptotically slow motion [39].

In the present chapter we analyze the stick-slip behavior of the bristle-based model. We differentiate between *exact stick-slip* and *quasi-stick-slip*. Exact stick-slip refers to motion in which a body attached to a compliance periodically comes to rest. This kind of motion, which is reminiscent of a limit cycle, occurs when the friction force drops as velocity increases from zero; the LuGre model can reproduce stick-slip friction, as can other friction models [25, 56, 57, 88–92]. Quasi-stick-slip refers to a limit cycle in which forward movement (that is, slip) is followed by a slight backward movement called quasi-slip. Furthermore, we use the steady-state characteristics of the emergent friction force to derive single-state friction models [93] that exhibit stick-slip friction. In particular, we derive the LuGre model [25–28] by this approach.

The contents of the chapter are as follows. In Section 3.2 we introduce the rotating bristle model, derive the governing equations, and show that this model exhibits quasi-stick-slip. In Section 3.3 we introduce the discontinuous rotating bristle model and show that this model exhibits exact stick-slip and hysteresis. In Section 3.4 we derive simplified versions of the discontinuous rotating bristle model, including the LuGre model. A preliminary version of some results from this chapter is given in [94].

3.2 Rotating Bristle Model

In this section we describe and analyze the rotating bristle model and demonstrate the emergence of quasi-stick-slip motion. The bristles represent the microscopic roughness of the surface on which the body is sliding as shown in Figure 3.1. The body of mass m and length d moves over an infinite row of rigid bristles, each of which has length l_b. The position of the center of mass of the body is denoted by x. At the base of each bristle is a torsional spring with stiffness coefficient κ and a torsional dashpot with damping coefficient c. The damping coefficient provides viscous energy dissipation but is otherwise negligible. The mass of each bristle is nonzero but negligible compared to the mass of the body. Therefore, the interaction between each bristle and the body is dominated by the stiffness of the torsional spring. Since the bristles are rigid, they rotate about their base point, but do not buckle. The distance between the bases of adjacent bristles is Δ, and the location of the base of the ith bristle is denoted by x_{b_i}. Furthermore, we assume that the body moves only horizontally, maintaining a constant height h above the ground. The body is not allowed to rotate or move vertically. The distance h can be viewed as the average height of the asperities, which determine the macroscopic roughness of the contacting surfaces. The length $d_0 \triangleq \sqrt{l_b^2 - h^2}$, and we assume throughout this chapter that $\dfrac{d_0}{\Delta} > 1$, so that at every instant there is at least one bristle contributing to the friction force.

As the body moves, there is a frictionless reaction force between the bristle and the body at the point of contact. This force is due to the torsional spring at the base of each bristle. We assume that the force on the body due to contact with the bristle is perpendicular to the direction of the bristle. The sum of all horizontal forces exerted by the bristles at each instant is defined to be the friction force. Since the bristle-body contact is frictionless, the direction of the reaction force between the body and each bristle contacting the lower surface of the body is vertical, and thus these bristles do not contribute to the friction force. Only the bristles that are in

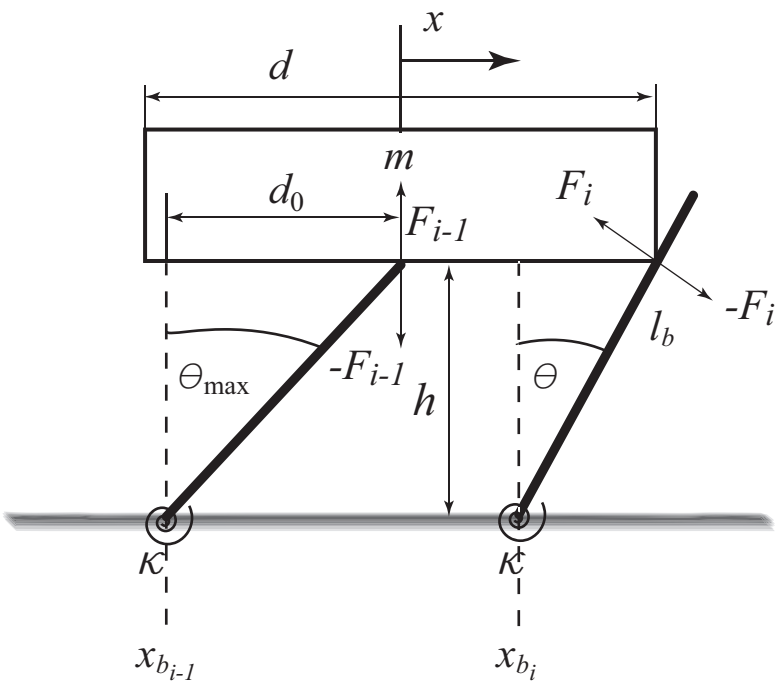

Figure 3.1: Schematic representation of the body and bristle contact for the rotating bristle model. The body of mass m slides over an infinite row of bristles with negligible mass and length l_b. Each bristle is attached to the ground at its base through a torsional spring with stiffness coefficient κ and a torsional dashpot with damping coefficient c. The distance between the bases of adjacent bristles is Δ, and the location of each bristle is denoted by x_{b_i}. The frictionless reaction force at the point of contact between the body and the ith bristle is F_i.

contact with the lower corners of the body contribute to the friction force.

For simplicity, we neglect the force due to the dashpot and the bristle dynamics resulting from the impact between the body and the bristle. The torsional dashpot and the bristle mass provide a mechanism for dissipation of the energy stored in the torsional spring but otherwise play no role in the bristle-body interaction. Modeling the impact between the body and each bristle would result in the bristles bouncing off the mass and hitting each other, thus significantly increasing the complexity of the model. Furthermore, we neglect the dynamics of the bristles since they represent the asperities of the contacting surface, which can deform during the contact, but

otherwise exhibit no dynamics.

Furthermore, in simulations of the bristle model throughout this chapter we assume that the bristle-related parameters such as l_b, Δ, κ, etc. have numerical values with physical units. However, these parameter values do not necessarily represent physically meaningful quantities. They are a tool used to represent the interaction between the body and the asperities and have no physical meaning. We assign them units so that the model is dimensionally consistent, but otherwise do not assume that they represent physical quantities.

3.2.1 Bristle pivot angle

The pivot angle of each bristle depends on the position of the bristle relative to the body. Since the body is not allowed to move vertically, the distance h from the ground to the lower surface of the body is constant. The maximum angle $\theta_{\max}$ that a bristle can pivot is given by

$$\theta_{\max} = \cos^{-1}\left(\frac{h}{l_b}\right), \tag{3.1}$$

and $\theta_{\max} < \frac{\pi}{2}$.

If the ith bristle is pivoted less than $\theta_{\max}$, then its pivot angle θ_i depends on the distance from the position x of the center of the mass of the body to the location x_{b_i} of the base of the ith bristle. If the bristle is in contact with the right lower corner of the body, then $\theta_i = \theta_i^r$, where

$$\theta_i^r = \tan^{-1}\left(\frac{x + \frac{d}{2} - x_{b_i}}{h}\right) \geq 0. \tag{3.2}$$

If the bristle is in contact with the left lower corner of the body, then $\theta_i = \theta_i^l$, where

$$\theta_i^l = \tan^{-1}\left(\frac{x - \frac{d}{2} - x_{b_i}}{h}\right) \leq 0. \tag{3.3}$$

We use the pivot angle of each bristle to calculate its contribution to the friction force.

3.2.2 Friction force

The friction force is equal to the sum of the horizontal components of all of the contact forces between the body and the bristles that are pivoted less than $\theta_{\max}$ and thus are in contact with one of the lower corners of the body. When the ith bristle is in contact with either the left or right lower corner of the body and pivoted by the angle θ_i, the distance from the base of the ith bristle to the point at which the contact force acts is

$$r_i = \frac{h}{\cos\theta_i}, \tag{3.4}$$

the contact force between the body and the ith bristle is

$$F_i = \frac{\kappa\theta_i}{r_i} = \frac{\kappa\theta_i \cos\theta_i}{h}, \tag{3.5}$$

and the horizontal component of the contact force (3.5) due to the ith bristle is

$$F_{fi} = F_i \cos\theta_i = \frac{\kappa\theta_i(\cos\theta_i)^2}{h}. \tag{3.6}$$

To describe the friction force that results from the interaction between the bristles and the body, we define $\Theta_r \in \mathbb{R}^n$ to be the vector whose entries are the pivot angles θ_i^r of the bristles in contact with the right lower corner of the body. Likewise, $\Theta_l \in \mathbb{R}^n$

is the vector whose entries are the pivot angles θ_i^l of the bristles in contact with the left lower corner of the body. We define $\mathcal{X}_b^r(x)$ to be the set of base positions x_{b_i} of the bristles in contact with the right lower corner of the body and $\mathcal{X}_b^l(x)$ to be the set of base positions x_{b_i} of the bristles in contact with the left lower corner of the body. The pivot angles θ_i^r and θ_i^l are calculated by using the elements of the sets $\mathcal{X}_b^r(x)$ and $\mathcal{X}_b^l(x)$ in (3.2) and (3.3), respectively. The elements of $\mathcal{X}_b^r(x)$ and $\mathcal{X}_b^l(x)$ are determined based on the position and velocity of the body by using the rules outlined in Table 3.1, where x_{r-} is the base position of the rightmost bristle contacting the lower surface of the body at the instant the velocity changes sign from negative to positive, and x_{r+} is the base position of the leftmost bristle contacting the lower surface of the body at the instant the velocity changes sign from positive to negative.

Velocity	Position	$\mathcal{X}_b^r(x)$, $\mathcal{X}_b^l(x)$	Description
$v \geq 0$	$x + \frac{d}{2} \leq x_{r-} + \Delta$	$\mathcal{X}_b^l = \{x_{b_i} : x - \frac{d}{2} \leq x_{b_i} < x - \frac{d}{2} + d_0\}$ $\mathcal{X}_b^r = \varnothing$	Figure 3.2(a)-(1)
	$x_{r-} + 2\Delta > x + \frac{d}{2} \geq x_{r-} + \Delta$	$\mathcal{X}_b^l = \{x_{b_i} : x - \frac{d}{2} \leq x_{b_i} < x - \frac{d}{2} + d_0\}$ $\mathcal{X}_b^r = \{x_{b_i} : x_{r-} + \Delta \leq x_{b_i} < x + \frac{d}{2}\}$	Figure 3.2(a)-(2)
	$x + \frac{d}{2} \geq x_{r-} + 2\Delta$ $x_{r-} - d_0 \geq x - \frac{d}{2}$	$\mathcal{X}_b^l = \{x_{b_i} : x - \frac{d}{2} \leq x_{b_i} < x - \frac{d}{2} + d_0\}$ $\mathcal{X}_b^r = \{x_{b_i} : x + \frac{d}{2} - d_0 < x_{b_i} \leq x + \frac{d}{2}\}$	Figure 3.2(a)-(3)
	$x_{r-} \geq x - \frac{d}{2} > x_{r-} - d_0$	$\mathcal{X}_b^l = \{x_{b_i} : x - \frac{d}{2} \leq x_{b_i} \leq x_{r-}\}$ $\mathcal{X}_b^r = \{x_{b_i} : x + \frac{d}{2} - d_0 < x_{b_i} \leq x + \frac{d}{2}\}$	Figure 3.2(a)-(4)
	$x - \frac{d}{2} > x_{r-}$	$\mathcal{X}_b^l = \varnothing$ $\mathcal{X}_b^r = \{x_{b_i} : x + \frac{d}{2} - d_0 < x_{b_i} \leq x + \frac{d}{2}\}$	Figure 3.2(a)-(5)
$v < 0$	$x - \frac{d}{2} > x_{r+} - \Delta$	$\mathcal{X}_b^l = \varnothing$ $\mathcal{X}_b^r = \{x_{b_i} : x + \frac{d}{2} - d_0 < x_{b_i} \leq x + \frac{d}{2}\}$	Figure 3.2(b)-(1)
	$x_{r+} - 2\Delta < x - \frac{d}{2} \leq x_{r+} - \Delta$	$\mathcal{X}_b^l = \{x_{b_i} : x - \frac{d}{2} < x_{b_i} \leq x_{r+} - \Delta\}$ $\mathcal{X}_b^r = \{x_{b_i} : x + \frac{d}{2} - d_0 \leq x_{b_i} \leq x + \frac{d}{2}\}$	Figure 3.2(b)-(2)
	$x - \frac{d}{2} \leq x_{r+} - 2\Delta$ $x_{r+} + d_0 \leq x + \frac{d}{2}$	$\mathcal{X}_b^l = \{x_{b_i} : x - \frac{d}{2} \leq x_{b_i} < x - \frac{d}{2} + d_0\}$ $\mathcal{X}_b^r = \{x_{b_i} : x + \frac{d}{2} - d_0 < x_{b_i} \leq x + \frac{d}{2}\}$	Figure 3.2(b)-(3)
	$x_{r+} \leq x + \frac{d}{2} < x_{r+} + d_0$	$\mathcal{X}_b^l = \{x_{b_i} : x - \frac{d}{2} < x_{b_i} \leq x - \frac{d}{2} + d_0\}$ $\mathcal{X}_b^r = \{x_{b_i} : x_{r+} \leq x_{b_i} \leq x + \frac{d}{2}\}$	Figure 3.2(b)-(4)
	$x + \frac{d}{2} < x_{r+}$	$\mathcal{X}_b^l = \{x_{b_i} : x - \frac{d}{2} \leq x_{b_i} < x - \frac{d}{2} + d_0\}$ $\mathcal{X}_b^r = \varnothing$	Figure 3.2(b)-(5)

Table 3.1: The sets $\mathcal{X}_b^r(x)$ and $\mathcal{X}_b^l(x)$ as a function of the position and velocity.

Figure 3.2 illustrates the bristle-body contact scenarios described in Table 3.1. Figure 3.2(a) shows the bristle-body interaction starting at the instant the sign of the velocity changes from negative to positive. As the body moves, the bristles that contribute to the friction force change, and so do the sets $\mathcal{X}_b^r(x)$ and $\mathcal{X}_b^l(x)$. In Figure 3.2(a)-(1) the body starts moving to the right, and all the bristles in contact with the body are pivoted counterclockwise, that is, $\theta_i < 0$. The resulting friction force causes the body to accelerate to the right while $x + \frac{d}{2} < x_{r-} + \Delta$. The body encounters the first bristle to its right in Figure 3.2(a)-(2). As the body continues to move to the right, its right lower corner comes in contact with additional bristles since $x + \frac{d}{2} \geq x_{r-} + 2\Delta$, and bristles push on both lower corners of the body as shown in Figure 3.2(a)-(3). In Figure 3.2(a)-(4) the left lower corner of the body is in contact with the only remaining bristle with $\theta_i < 0$, located at x_{r-}. Finally, as the left lower corner of the body passes the base of the bristle located at x_{r-}, that is, $x - \frac{d}{2} > x_{r-}$, only bristles with $\theta_i > 0$ remain in contact with the body as shown in Figure 3.2(a)-(5). Figure 3.2(b) shows the bristle-body interaction starting at the instant the sign of the velocity changes from positive to negative. The direction reversal described in Figure 3.2(b) is analogous to Figure 3.2(a).

All simulations start at $t = t_0$ with the body position $x = x_0$, and the sets $\mathcal{X}_b^l$ and $\mathcal{X}_b^r$ are assumed to be empty at $t = t_0$. That is, at the beginning of all simulations, the only bristles contacting the body are the bristles contacting the bottom surface of the body and supporting the weight of the body. Therefore, no bristles are in contact with the right or left lower corners of the body at $t = t_0$. The friction force is thus zero and the body encounters bristles according to the rules outlined in Table 3.2.

Once the sets $\mathcal{X}_b^r(x)$ and $\mathcal{X}_b^l(x)$ are known, the horizontal component of the contact force due to all of the bristles in contact with the right lower corner of the body is

$$F_f^r = \frac{\kappa}{h}\Theta_r^{\mathrm{T}} \left(\cos\Theta_r \circ \cos\Theta_r\right), \tag{3.7}$$

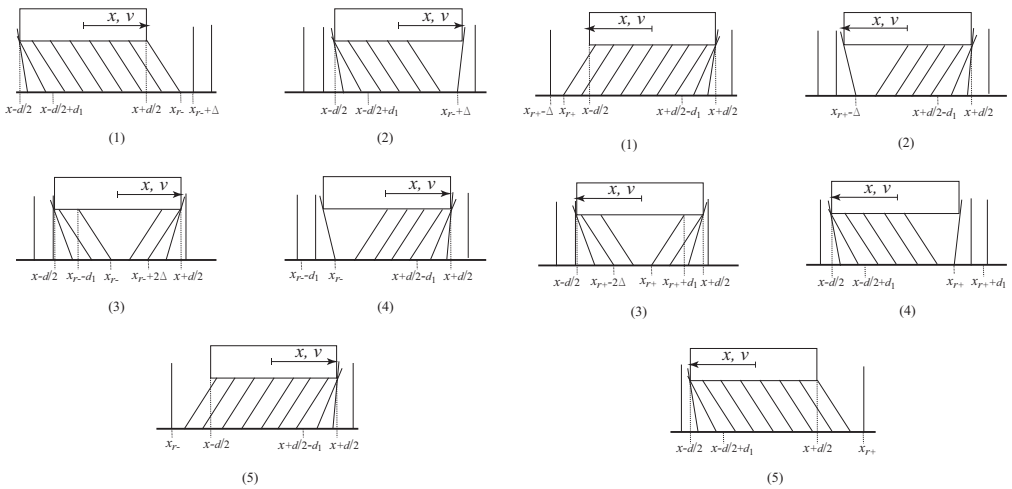

Figure 3.2: Interaction of the body and bristles during reversals of the body's motion. (a) shows the bristle-body interaction as the sign of the velocity of the body changes from negative to positive. Bristle-body interaction as the sign of velocity of the body changes from positive to negative is shown in (b).

Velocity	Position	$\mathcal{X}_b^r(x)$, $\mathcal{X}_b^l(x)$
$v \geq 0$	$x < x_0 + d_0$	$\mathcal{X}_b^l = \varnothing$ $\mathcal{X}_b^r = \{x_{b_i} : x_0 + \frac{d}{2} < x_{b_i} \leq x + \frac{d}{2}\}$
	$x \geq x_0 + d_0$	$\mathcal{X}_b^l = \varnothing$ $\mathcal{X}_b^r = \{x_{b_i} : x + \frac{d}{2} - d_0 < x_{b_i} \leq x + \frac{d}{2}\}$
$v < 0$	$x > x_0 - d_0$	$\mathcal{X}_b^l = \{x_{b_i} : x - \frac{d}{2} \geq x_{b_i} < x_0 - \frac{d}{2}\}$ $\mathcal{X}_b^r = \varnothing$
	$x \leq x_0 - d_0$	$\mathcal{X}_b^l = \{x_{b_i} : x - \frac{d}{2} \geq x_{b_i} < x - \frac{d}{2} + d_0\}$ $\mathcal{X}_b^r = \varnothing$

Table 3.2: Initialization of sets $\mathcal{X}_b^r$ and $\mathcal{X}_b^l$.

where "$\circ$" denotes component-wise vector multiplication and the function $\cos(\cdot)$ operates on each component of its vector argument. Likewise, the horizontal component of the contact force due to all of the bristles in contact with the left lower corner of

the body is

$$F_f^l = \frac{\kappa}{h}\Theta_l^{\mathrm{T}} \left(\cos\Theta_l \circ \cos\Theta_l\right). \tag{3.8}$$

The total friction force is thus

$$F_f = F_f^l + F_f^r, \tag{3.9}$$

where $\mathcal{X}_b^r(x)$ and $\mathcal{X}_b^l(x)$ are determined from tables 3.1 and 3.2.

For illustration, consider the body moving with the prescribed position $x(t) = A\sin(\omega t)$ and velocity $v(t) = A\omega\cos(\omega t)$, where $A = 5$ m and $\omega = 0.1$ rad/s. The remaining model parameters are $m = 1$ kg, $d = 1$ m, $\kappa = 0.1$ N-m/rad, $\Delta = 0.002$ m, $l_b = 0.1$ m, $h = 0.098$ m, $d_0 = 0.0199$ m. The resulting friction force as a function of position is shown in Figure 3.3(a) and as a function of velocity in Figure 3.3(b). The friction force is initially zero and increases as the mass moves and encounters bristles. The friction force drops slightly when a bristle reaches its maximum pivot angle $\theta_{\max}$ and increases when a new bristle comes in contact with the right lower corner of the body. The magnitude of the friction force oscillates around zero when a direction reversal occurs, since bristles push simultaneously on both the right and left lower corners of the body. In contrast with the Coulomb and LuGre friction models [6, 24, 28], Figure 3.3(b) shows that, as the velocity crosses zero, the friction force does not change sign.

3.2.3 Stick-slip behavior

To investigate stick-slip behavior, we simulate the system shown in Figure 3.4. The body of mass m is connected to a spring with stiffness K. The free end of the

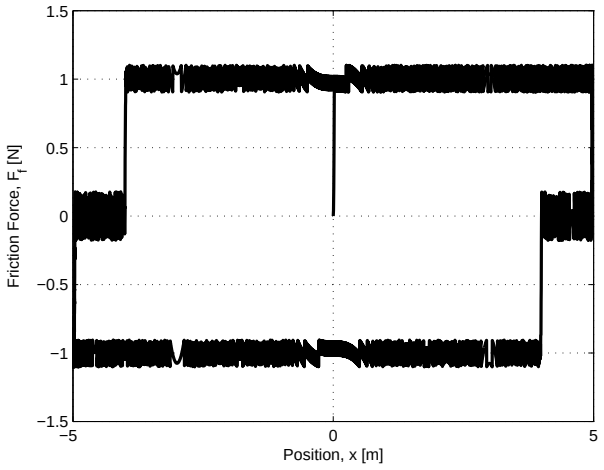

(a)

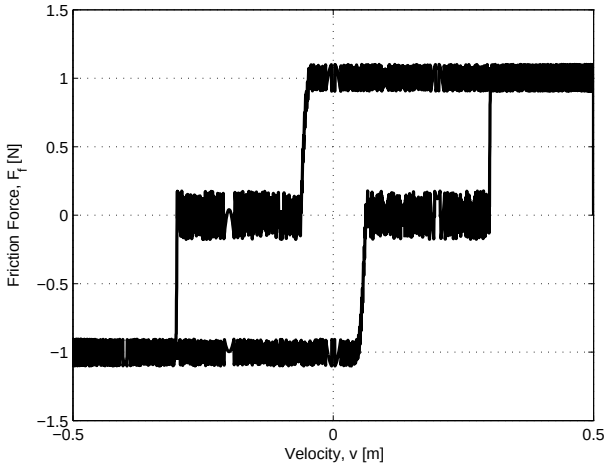

(b)

Figure 3.3: The friction force (3.7)-(3.9) of the rotating bristle model as a function of position (a) and velocity (b). The position of the body is prescribed to be $x(t) = A\sin(\omega t)$ and velocity $v(t) = A\omega\cos(\omega t)$, where $A = 5$ m, $\omega = 0.1$ rad/s.

spring moves at the constant speed v_p. The equations of motion are

$$\dot{x} = v, \tag{3.10}$$

$$\dot{v} = \frac{1}{m}(Kl - F_f), \tag{3.11}$$

$$\dot{l} = v_p - v, \tag{3.12}$$

where v is the velocity of the body relative to the ground, l is the length of the spring, and F_f is the friction force described by (3.7)-(3.9).

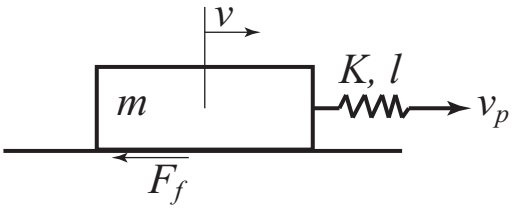

Figure 3.4: Body-spring configuration used to investigate the stick-slip properties of the rotating bristle model. The body of mass m is connected to a spring with stiffness K. The free end of the spring moves at the constant speed v_p. The friction force F_f is given by (3.7)-(3.9).

The results of the simulation of the system (3.10)-(3.12) with friction force described by (3.7)-(3.9) are shown in Figure 3.5. The velocity of the free end of the spring is $v_p = 0.5$ m/s, and the model parameters are $\kappa = 0.5$ N-m/rad, $m = 1$ kg, $K = 1$ N/m, $d = 1$ m, $\Delta = 0.01$ m, $d_0 = 0.0199$ m, $l_b = 0.1$ m, and $h = 0.098$ m. The trajectories projected onto the l-v plane form a limit cycle shown in Figure 3.5(a). The time histories of x, l, v, and F_f are shown in Figure 3.5(b). As the free end of the spring moves, the spring force overcomes the friction force and the mass accelerates to the right. This is the slip phase. However, as the mass accelerates, the spring length decreases and the friction force becomes larger than the spring force. The body decelerates, momentarily comes to rest, and reverses its direction of motion due to the bristles pushing on it from the right (see Figure 3.2(b)-(1)). This phase is called *quasi-stick* since, unlike exact stick, the body does not remain stationary. The body moves to the left, its left lower corner comes in contact with bristles, and it continues moving to the left until the friction force becomes negative, corresponding to Figure 3.2(b)-(5). At this instant, the friction force and the spring force are pushing the body in the same direction, and the body accelerates to the right.

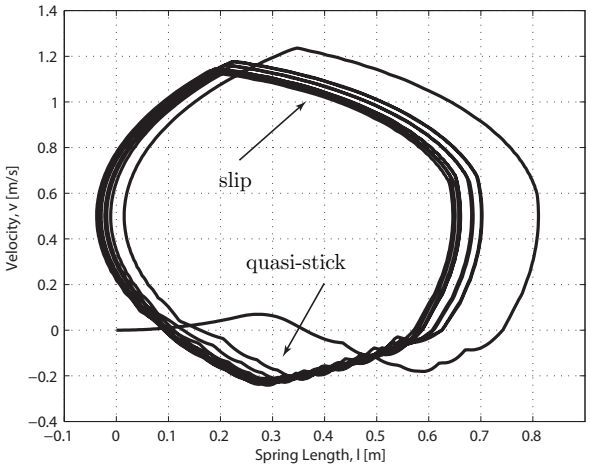

(a)

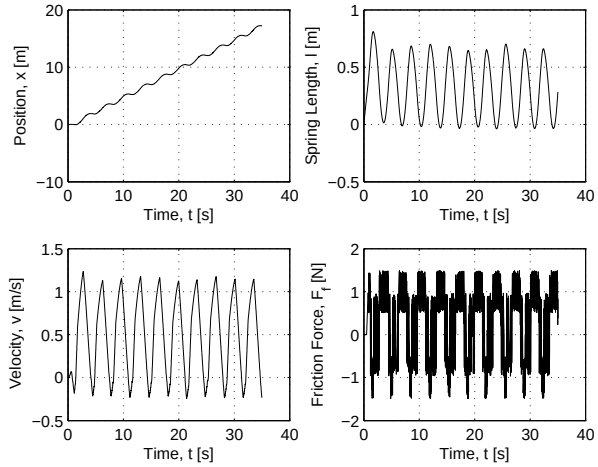

(b)

Figure 3.5: Quasi-stick-slip limit cycle of the rotating bristle model. The limit cycle in the l-v plane is shown in (a), and the time histories of x, l, v, and F_f are shown in (b).

3.3 Discontinuous Rotating Bristle Model

In this section, we introduce the discontinuous rotating bristle model (DRBM), which is identical to the rotating bristle model except during direction reversals. In particular, the details of the direction reversals arising in the rotating bristle model are replaced by a simplified model in the DRBM. Simplify the rotating bristle model

in hopes of observing the exact-stick-slip limit cycle, since the goal of this chapter is to investigate the origins of exact-stick-slip.

To construct the DRBM, we assume that when the velocity of the body passes through zero and changes sign from positive to negative, the configuration in which all of the bristles contacting the body are pivoted to the right, $\theta_i \geq 0$, jumps discontinuously to a configuration in which all of the bristles contacting it are pivoted to the left, $\theta_i \leq 0$. Similarly, when the velocity of the body passes through zero and changes sign from negative to positive, the configuration in which all of the bristles contacting the body are pivoted to the left, $\theta_i \leq 0$, jumps discontinuously to the configuration in which all of the bristles contacting it are pivoted to the right, $\theta_i \geq 0$. In figures 3.2(a) and 3.2(b) this is equivalent to an instantaneous transition from the configuration in Figure 3.2(a)-(1) and 3.2(b)-(1) to the configuration in Figure 3.2(a)-(5) and 3.2(b)-(5), respectively, without passing through the configurations described in figures 3.2(a)-(2), -(3), and -(4) and 3.2(b)-(2),-(3),-(4), respectively.

The DRBM friction force for $v \geq 0$ is given by

$$F_f = F_f^r, \tag{3.13}$$

where F_f^r is defined by (3.7) and the components of Θ_r are given by (3.2) with x_{b_i} in the set

$$\mathcal{X}_b^r(x) = \{x_{b_i} \,:\, x + \frac{d}{2} - d_0 < x_{b_i} \leq x + \frac{d}{2}\}. \tag{3.14}$$

Note that, for every value of x, the set $\mathcal{X}_b^r(x)$ is nonempty and is initialized from (3.14) based on the initial position $x(t_0)$. For $v < 0$, the DRBM friction force is given by

$$F_f = F_f^l, \tag{3.15}$$

where F_f^l is defined by (3.8) and the components of Θ_l are given by (3.3) with x_{b_i} in the set

$$\mathcal{X}_b^l(x) = \{x_{b_i} \,:\, x - \frac{d}{2} \leq x_{b_i} < x - \frac{d}{2} + d_0\}, \tag{3.16}$$

which, for all values of x, is nonempty and is initialized from (3.16) based on the initial position $x(t_0)$.

Due to the discontinuous jump from a configuration in which all of the pivot angles satisfy $\theta_i \geq 0$ to a configuration in which all of the pivot angles satisfy $\theta_i \leq 0$, and vice versa, we compare the value of F_f as $v \to 0^+$ with the value of F_f as $v \to 0^-$ in order to determine discontinuities of the friction force at zero velocity. The value of θ_i given by (3.2) with $x_{b_i} \in \mathcal{X}_b^r(x)$ defined by (3.14) is in the range

$$0 \leq \theta_i < \tan^{-1}\left(\frac{d_0}{h}\right). \tag{3.17}$$

Thus, it follows from (3.13) and (3.7) that $F_f \geq 0$ for all $v \geq 0$. However, since $\dfrac{d_0}{\Delta} > 1$, $\mathcal{X}_b^r(x)$ has at least one element, namely, the ith bristle with base at x_{b_i} and $\theta_i > 0$. The contribution of the ith bristle to the friction force F_f is thus nonzero and therefore $F_f > 0$ for all $v \geq 0$. On the other hand, the value of θ_i given by (3.3) with $x_{b_i} \in \mathcal{X}_b^l(x)$ defined by (3.16) satisfies

$$-\tan^{-1}\left(\frac{d_0}{h}\right) < \theta_i \leq 0. \tag{3.18}$$

It follows from (3.15) and (3.8) that $F_f \leq 0$ for all $v < 0$. However, since $\dfrac{d_0}{\Delta} > 1$, $\mathcal{X}_b^l(x)$ has at least one element, namely, the ith bristle with base at x_{b_i} and $\theta_i < 0$. The contribution of the ith bristle to the friction force F_f is thus nonzero and therefore $F_f < 0$ for all $v < 0$.

Since $F_f > 0$ for all $v \geq 0$ and $F_f < 0$ for all $v < 0$, we look for the minimum

value of (3.13) and maximum value of (3.15). The minimum value of F_f for $v \geq 0$ occurs when only the ith bristle is contributing to the friction force and thus $x_{b_i} = x + \frac{d}{2} - d_0 + \Delta$, $x_{b_i} \in \mathcal{X}_b^r(x)$, and $\theta_i = \tan^{-1}\left(\frac{d_0 - \Delta}{h}\right) > 0$. At this instant the pivot angle of the $(i-1)$th bristle reaches $\theta_{\max}$ and no longer contributes to the friction force, that is, $x_{b_{i-1}} = x + \frac{d}{2} - d_0$. Thus, the ith bristle is the only bristle contributing to the friction force, and the minimum value of F_f defined by (3.13) and (3.7) for $v \geq 0$ is

$$F_{f,\min} = \frac{k}{h}\tan^{-1}\left(\frac{d_0 - \Delta}{h}\right)\cos^2\left(\tan^{-1}\left(\frac{d_0 - \Delta}{h}\right)\right) > 0. \tag{3.19}$$

Similarly, the maximum value of F_f for $v < 0$ occurs when only the ith bristle contributes to the friction force and thus $x_{b_i} = x - \frac{d}{2} + d_0 - \Delta$, $x_{b_i} \in \mathcal{X}_b^l(x)$, and $\theta_i = -\tan^{-1}\left(\frac{d_0 - \Delta}{h}\right) < 0$. At this instant, the pivot angle of the $(i+1)$th bristle reaches $\theta_{\max}$ and no longer contributes to the friction force, that is $x_{b_{i+1}} = x - \frac{d}{2} + d_0$. Thus, the ith bristle is the only bristle contributing to the friction force, and the maximum value of F_f defined by (3.15) and (3.8) for $v < 0$ is

$$F_{f,\max} = -\frac{k}{h}\tan^{-1}\left(\frac{d_0 - \Delta}{h}\right)\cos^2\left(\tan^{-1}\left(\frac{d_0 - \Delta}{h}\right)\right) = -F_{f,\min} < 0. \tag{3.20}$$

Comparing (3.19) with (3.20) shows that, for all $v \geq 0$, $F_f \geq F_{f,\min} > 0$ whereas, for all $v < 0$, $F_f \leq F_{f,\max} < 0$, where $F_{f,\max} = -F_{f,\min}$. Therefore,

$$\lim_{v \to 0^-} F_f < 0 < \lim_{v \to 0^+} F_f, \tag{3.21}$$

which implies that the DRBM friction force F_f defined by (3.13)-(3.16) is discontinuous at $v = 0$.

As in the previous section, we consider the body moving with the prescribed position $x(t) = A\sin(\omega t)$ and velocity $v(t) = A\omega\cos(\omega t)$, where $A = 1$ m and $\omega = 0.01$

rad/s. The resulting DRBM friction force as a function of position is shown in Figure 3.6(a) and as a function of velocity in Figure 3.6(b). In Figure 3.6(a), a drop in the friction force appears when a bristle reaches the pivot angle $\theta_{\max}$, making the friction force look like a sawtooth function of position. The friction force of the DRBM does not oscillate around zero during direction reversals as in Figure 3.3(a). However, the direction of the friction force instantaneously switches while the magnitude remains unchanged, resulting in a discontinuity at $v = 0$ as shown in Figure 3.6(b). The velocity is zero at $t_1 = \dfrac{\pi}{2\omega}$ and $t_2 = \dfrac{3\pi}{2\omega}$, and thus, a discontinuity in friction force is also visible in Figure 3.6(a) at $x(t_1) = 1$ m and $x(t_2) = -1$ m.

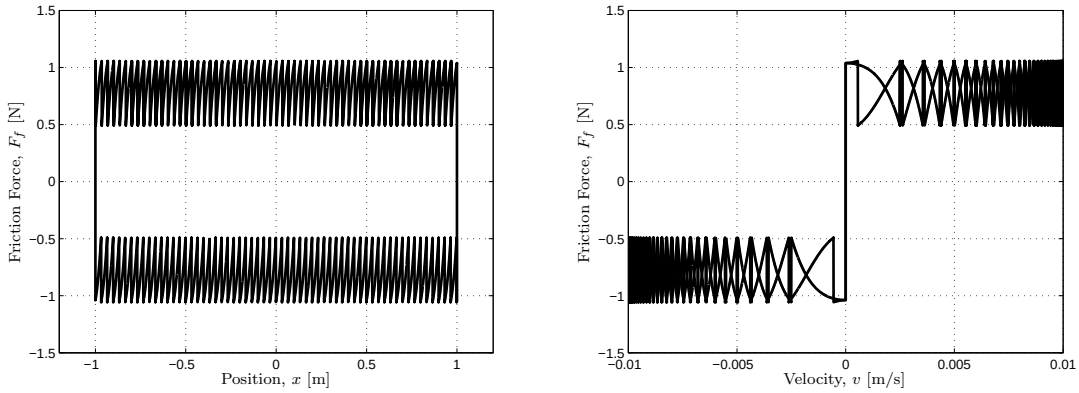

(a) (b)

Figure 3.6: The DRBM friction force (3.13)-(3.16) as a function of position (a) and velocity (b). The position of the body is prescribed to be $x = A\sin(\omega t)$, and the velocity $v = A\omega\cos(\omega t)$, where $A = 1$ m, $\omega = 0.01$ rad/s. As shown in (b) the DRBM friction force is discontinuous at $v = 0$.

3.3.1 Switch Model

Due to the discontinuity of the DRBM friction force (3.13)-(3.16) at $v = 0$, the integration of (3.10)-(3.12) with the friction force represented by the DRBM (3.13)-(3.16) requires special numerical techniques. In this section we describe the Switch Model [88, 95], which is a technique that smooths out the discontinuous dynamics

around the discontinuity $v = 0$. The modified equations can then be integrated using standard numerical integration techniques.

To begin, we rewrite the equations of motion in which the friction force is modeled by the DRBM as a differential inclusion [95]. Assume that the motion of the body is described by

$$\dot{\boldsymbol{x}} = \boldsymbol{f}(\boldsymbol{x}), \tag{3.22}$$

where $\boldsymbol{x} \in \mathbb{R}^m$ and $\boldsymbol{f} : \mathcal{V} \subset \mathbb{R}^m \to \mathbb{R}^m$ is a piecewise continuous vector field, and $\Sigma \triangleq \mathbb{R}^m \backslash \mathcal{V}$ is the set of points of discontinuity of $\boldsymbol{f}$. We assume that there exists a function $g : \mathbb{R}^m \to \mathbb{R}$ such that the discontinuity boundary Σ is given by the roots of g, that is

$$\Sigma = \{\boldsymbol{x} \in \mathbb{R}^m : \ g(\boldsymbol{x}) = 0\}. \tag{3.23}$$

We also define sets

$$\mathcal{V}_+ \triangleq \{\boldsymbol{x} \in \mathbb{R}^m : \ g(\boldsymbol{x}) > 0\}, \tag{3.24}$$

$$\mathcal{V}_- \triangleq \{\boldsymbol{x} \in \mathbb{R}^m : \ g(\boldsymbol{x}) < 0\}. \tag{3.25}$$

With these definitions, (3.22) can be rewritten as the differential inclusion [95, 96]

$$\dot{\boldsymbol{x}} \in \begin{cases} \boldsymbol{f}_+(\boldsymbol{x}), \ \boldsymbol{x} \in \mathcal{V}_+, \\ \alpha \boldsymbol{f}_+(\boldsymbol{x}) + (1-\alpha)\boldsymbol{f}_-(\boldsymbol{x}), \ \boldsymbol{x} \in \Sigma, \ \alpha \in [0,1], \\ \boldsymbol{f}_-(\boldsymbol{x}), \ \boldsymbol{x} \in \mathcal{V}_-. \end{cases} \tag{3.26}$$

The direction of the flow given by the vector fields $\boldsymbol{f}_+(\boldsymbol{x})$ and $\boldsymbol{f}_-(\boldsymbol{x})$ can lead to three types of sliding modes across Σ. If the flow is such that the solutions of

(3.26) are pushed to Σ in both $\mathcal{V}_+$ and $\mathcal{V}_-$, then the sliding mode is *attractive*. If the solutions cross Σ, then the sliding mode is *transversal*. Finally, if the solutions diverge from Σ, the sliding mode is *repulsive* [95].

The Switch Model smooths out the dynamics of the differential inclusion (3.26) by constructing a *stick band* within the set $\mathcal{G} \triangleq \{\boldsymbol{x} : |g(\boldsymbol{x})| \leq \eta\}$, where η is a small positive constant. (Note that the term "stick band" is not related to stick-slip friction.) The dynamics outside of the stick band remain the same. The dynamics inside the stick band depend on the type of sliding mode across the discontinuity boundary. If the sliding mode is attractive, that is,

$$\boldsymbol{n}^{\mathrm{T}}\boldsymbol{f}_-(\boldsymbol{x}) > 0 \text{ and } \boldsymbol{n}^{\mathrm{T}}\boldsymbol{f}_+(\boldsymbol{x}) < 0, \quad \boldsymbol{x} \in \Sigma, \tag{3.27}$$

where $\boldsymbol{n} \triangleq \nabla g(\boldsymbol{x})$ is the normal to Σ, then the stick-band dynamics are given by

$$\dot{\boldsymbol{x}} = \alpha\boldsymbol{f}_+(\boldsymbol{x}) + (1-\alpha)\boldsymbol{f}_-(\boldsymbol{x}), \; \boldsymbol{x} \in \mathcal{G}. \tag{3.28}$$

The value of the parameter α is chosen such that it pushes the solutions of (3.27) toward the middle of the stick band, that is, toward $g(\boldsymbol{x}) = 0$. Thus, inside the stick band, g satisfies

$$\dot{g}(\boldsymbol{x}) = -\tau g(\boldsymbol{x}), \tag{3.29}$$

where $\tau > 0$ is a time constant. Since

$$\dot{g}(\boldsymbol{x}) = \frac{dg(\boldsymbol{x})}{d\boldsymbol{x}}\frac{d\boldsymbol{x}}{dt} = \nabla\boldsymbol{g}^T\dot{\boldsymbol{x}} \tag{3.30}$$

$$= \boldsymbol{n}^T\left(\alpha\boldsymbol{f}_+(\boldsymbol{x}) + (1-\alpha)\boldsymbol{f}_-(\boldsymbol{x})\right), \tag{3.31}$$

setting (4.35) equal to (4.37) and solving for α gives

$$\alpha = \frac{\boldsymbol{n}^T \boldsymbol{f}_-(\boldsymbol{x}) + \tau^{-1} g(\boldsymbol{x})}{\boldsymbol{n}^T (\boldsymbol{f}_-(\boldsymbol{x}) - \boldsymbol{f}_+(\boldsymbol{x}))}. \tag{3.32}$$

If the sliding mode is transversal, that is,

$$(\boldsymbol{n}^{\mathrm{T}} \boldsymbol{f}_-(\boldsymbol{x}))(\boldsymbol{n}^{\mathrm{T}} \boldsymbol{f}_+(\boldsymbol{x})) > 0, \quad \boldsymbol{x} \in \Sigma, \tag{3.33}$$

then the stick-band dynamics are defined by

$$\dot{\boldsymbol{x}} = \begin{cases} \boldsymbol{f}_-(\boldsymbol{x}), \text{ if } \boldsymbol{n}^{\mathrm{T}} \boldsymbol{f}_-(\boldsymbol{x}) < 0 \text{ and } \boldsymbol{n}^{\mathrm{T}} \boldsymbol{f}_+(\boldsymbol{x}) < 0\,,\ \boldsymbol{x} \in \mathcal{G}, \\ \boldsymbol{f}_+(\boldsymbol{x}), \text{ if } \boldsymbol{n}^{\mathrm{T}} \boldsymbol{f}_-(\boldsymbol{x}) > 0 \text{ and } \boldsymbol{n}^{\mathrm{T}} \boldsymbol{f}_+(\boldsymbol{x}) > 0\,,\ \boldsymbol{x} \in \mathcal{G}. \end{cases} \tag{3.34}$$

Finally, if the sliding mode is repulsive, that is,

$$\boldsymbol{n}^{\mathrm{T}} \boldsymbol{f}_-(\boldsymbol{x}) < 0 \text{ and } \boldsymbol{n}^{\mathrm{T}} \boldsymbol{f}_+(\boldsymbol{x}) > 0, \quad \boldsymbol{x} \in \Sigma, \tag{3.35}$$

than the dynamics are defined by

$$\dot{\boldsymbol{x}} = \boldsymbol{f}_+(\boldsymbol{x})\,,\ \boldsymbol{x} \in \mathcal{G}. \tag{3.36}$$

Outside of the stick band, the dynamics are defined by

$$\dot{\boldsymbol{x}} = \begin{cases} \boldsymbol{f}_+(\boldsymbol{x}),\ \boldsymbol{x} \in \mathcal{G}_+, \\ \boldsymbol{f}_-(\boldsymbol{x}),\ \boldsymbol{x} \in \mathcal{G}_-, \end{cases} \tag{3.37}$$

where $\mathcal{G}_+ \triangleq \{\boldsymbol{x} : g(\boldsymbol{x}) > \eta\}$ and $\mathcal{G}_- \triangleq \{\boldsymbol{x} : g(\boldsymbol{x}) < \eta\}$. More details about the Switch Model (3.27)-(3.37) and a pseudocode are given in [95].

3.3.2 Stick-slip behavior

We use the Switch Model (3.27)-(3.37) to simulate the system shown in Figure 3.4 and defined by (3.10)-(3.12) with friction force defined by the DRBM (3.13)-(3.16). The system (3.10)-(3.12) with friction force modeled by (3.13)-(3.16) can be formulated as a differential inclusion (3.26) with $\boldsymbol{x} \triangleq \begin{bmatrix} x & v & l \end{bmatrix}^{\mathrm{T}}$, the set Σ defined by the roots of the function $g(\boldsymbol{x}) = v$, the normal to Σ defined by $\boldsymbol{n} = \nabla g(\boldsymbol{x}) = \begin{bmatrix} 0 & 1 & 0 \end{bmatrix}^{\mathrm{T}}$, and the vector fields $\boldsymbol{f}_+(\boldsymbol{x})$ and $\boldsymbol{f}_-(\boldsymbol{x})$ defined by

$$\boldsymbol{f}_+(\boldsymbol{x}) \triangleq \begin{bmatrix} v \\ \frac{1}{m}(Kl - F_{f+}) \\ v_p - v \end{bmatrix}, \tag{3.38}$$

$$\boldsymbol{f}_-(\boldsymbol{x}) \triangleq \begin{bmatrix} v \\ \frac{1}{m}(Kl - F_{f-}) \\ v_p - v \end{bmatrix}, \tag{3.39}$$

where $F_{f+} = F_f^r$ is the DRBM friction force for $v \geq 0$ defined by (3.13) and $F_{f-} = F_f^l$ is the DRBM friction force for $v < 0$ defined by (3.15).

We use the Switch Model (3.27)-(3.37) to simulate the differential inclusion (3.26) with $\boldsymbol{f}_+(\boldsymbol{x})$ and $\boldsymbol{f}_-(\boldsymbol{x})$ defined by (3.38) and (3.39) with $m = 1$ kg, $K = 1$ N/m, $v_p = 0.002$ m/s, $d = 0.5$ N, $\kappa = 0.1$ N-m/rad, $h = 0.0995$ m, $l_b = 0.1$ m, $d_0 = 0.01$ m, $\Delta = 0.005$ m, and $\eta = 10^{-8}$. Part (a) of Figure 3.7 shows the limit cycle obtained by projecting the trajectories onto the l-v plane, and Figure 3.7(b) shows the time histories of x, l, v, and F_f. The exact stick-slip motion is represented by the limit cycle in the l-v plane. The quasi-stick phase of the rotating bristle model shown in Figure 3.5(a) is replaced by sticking, indicated by the line segment in which $v = 0$ and $\dot{l} = v_p$. The exact stick-slip behavior of the DRBM is a consequence of the drop in friction force that occurs when the bristle pivot angle reaches $\theta_{\max}$.

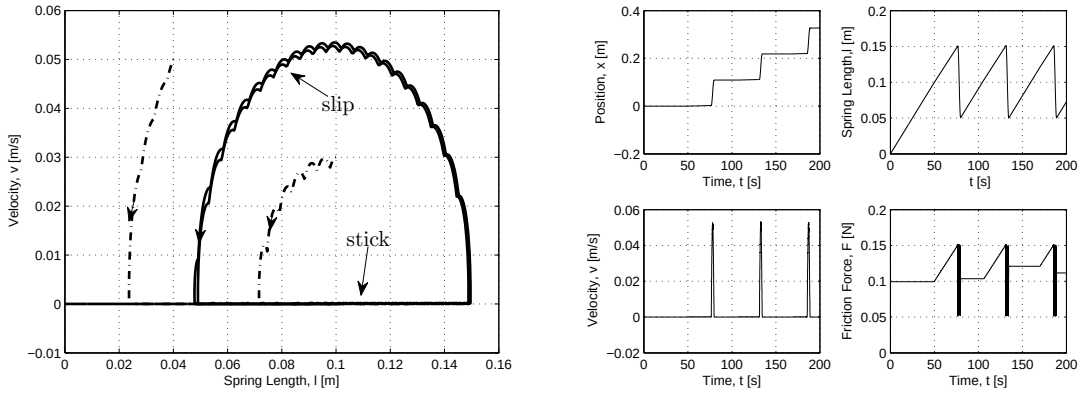

(a) (b)

Figure 3.7: The exact stick-slip limit cycle of (3.38)-(3.39) with friction force modeled by the DRBM (3.13)-(3.16). (a) shows the stable limit cycle in the l-v plane. The trajectories starting inside and outside of the limit cycle converge to it. (b) shows the time histories of x, l, v, and F_f with zero initial conditions. The parameter values are $m = 1$ kg, $K = 1$ N/m, $v_p = 0.002$ m/s, $d = 0.5$ N, $\kappa = 0.1$ N-m/rad, $h = 0.0995$ m, $l_b = 0.1$ m, $d_0 = 0.01$ m, $\Delta = 0.005$ m, and $\eta = 10^{-8}$.

3.3.3 Hysteresis map

We consider the mass-spring system shown in Figure 3.8. The body of mass m is attached to the wall by means of a spring with stiffness coefficient K. A periodic force input $u(t)$ acts on the body causing it to move over the horizontal surface. The friction force between the body and the surface is represented by the DRBM (3.13) - (3.16). The equations of motion are

$$\dot{x} = v, \tag{3.40}$$

$$\dot{v} = \frac{1}{m}(-Kx + u - F_f). \tag{3.41}$$

To formulate (3.40)-(3.41) with F_f defined by (3.13)-(3.16) as a differential inclusion (3.26), we define vector fields $\boldsymbol{f}_+(\boldsymbol{x})$ and $\boldsymbol{f}_-(\boldsymbol{x})$ corresponding to (3.40), (3.41)

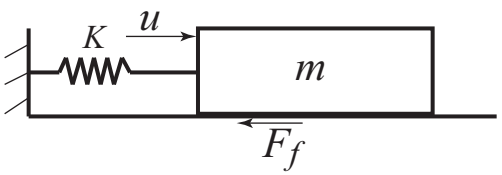

Figure 3.8: Body-spring configuration represented by (3.40)-(3.41). The body of mass m is connected to the wall by a means of a spring with stiffness K and is acted on by an external force input u.

by

$$\boldsymbol{f}_+(\boldsymbol{x}) \triangleq \begin{bmatrix} v \\ \frac{1}{m}(-Kx + u - F_{f+}) \end{bmatrix}, \tag{3.42}$$

$$\boldsymbol{f}_-(\boldsymbol{x}) \triangleq \begin{bmatrix} v \\ \frac{1}{m}(-Kx + u - F_{f-}) \end{bmatrix}, \tag{3.43}$$

where $\boldsymbol{x} = \begin{bmatrix} x & v \end{bmatrix}^{\mathrm{T}}$, $F_{f+} = F_f^r$ is the DRBM friction force for $v \geq 0$ defined by (3.13), and $F_{f-} = F_f^l$ is the DRBM friction force for $v < 0$ defined by (3.15). The set Σ is defined by the roots of the function $g(\boldsymbol{x}) = v$, so that $\boldsymbol{n} = \nabla g(\boldsymbol{x}) = \begin{bmatrix} 0 & 1 \end{bmatrix}^{\mathrm{T}}$.

We utilize the Switch Model (3.27)-(3.37) to simulate (3.26) with $\boldsymbol{f}_+(\boldsymbol{x})$ and $\boldsymbol{f}_-(\boldsymbol{x})$ defined by (3.42), (3.43), and the force input $u(t) = \sin(\omega t)$. The system parameters used are $m = 1$ kg, $K = 1$ N/m, $l_b = 0.1$ m, $\kappa = 0.1$ N-m/rad, $d = 1$ m, $h = 0.0995$ m, $\Delta = 0.01$ m, and $\eta = 10^{-6}$. The input-output map of (3.42)-(3.43) with $\omega = 0.05$ rad/s is shown in Figure 3.9(a) and with $\omega = 0.001$ rad/s is shown in Figure 3.9(b). At low input frequencies, the input-output map forms a loop, showing that the system is hysteretic. The input-output map $\mathcal{H}$, called the hysteresis map, is rate-dependent since its shape changes with the frequency of the input [55]. The staircase shape of the hysteresis map, also observed with the LuGre model, indicates exact stick-slip behavior [22]. The time histories of x, v, u, and F_f for $\omega = 0.001$ rad/s are shown in

Figure 3.9(c).

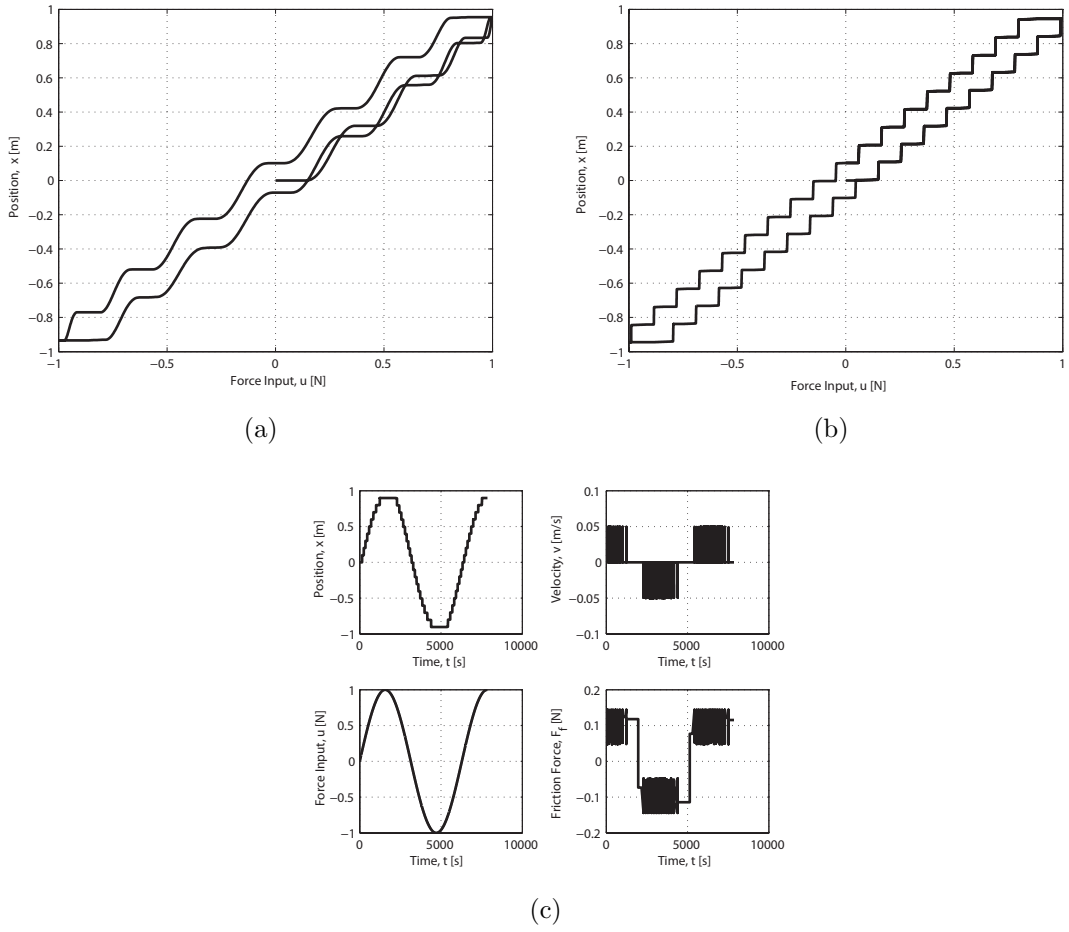

Figure 3.9: Simulation of (3.42)-(3.43) with friction force modeled by the DRBM with $u(t) = \sin(\omega t)$ N, $m = 1$ kg, $K = 1$ N/m, $l_b = 0.1$ m, $\kappa = 0.1$ N-m/rad, $d = 1$ m, $h = 0.0995$ m, $\Delta = 0.01$ m, and $\eta = 10^{-6}$. (a) shows the input-output map with $\omega = 0.05$ rad/s and (b) shows the input-output map with $\omega = 0.001$ rad/s. The shape of the input-output map at low frequencies indicates exact stick-slip behavior. The time histories of x, v, u, and F_f with $\omega = 0.001$ rad/s are shown in (c).

Since the input-output map of (3.42)-(3.43) is hysteretic, we can calculate the energy dissipated during one cycle of operation. The area $\mathcal{A}$ of the hysteresis map $\mathcal{H}$ shown in Figure 3.9(b) is equal to the energy loss during one cycle. To demonstrate, we begin with the expression for work done by the force $u(t)$ during one cycle and

use Green's theorem

$$E = \oint_{\mathcal{H}} u dx = \int\int_{\mathcal{A}} du dx = \mathcal{A} \tag{3.44}$$

to show that the work done E is equal to the area $\mathcal{A}$ of the hysteresis map. The energy dissipated based on the area of the hysteresis loop shown in Figure 3.9(b) is $E = 0.35647$ J.

Alternatively, we can calculate the dissipated energy by summing the potential energy stored in each torsional spring during the motion of the body. As each bristles pivots, energy is stored in its torsional spring, and is subsequently dissipated by the dashpot after the body passes beyond the bristle and the bristle is suddenly released. The total energy stored in the bristles is

$$E_{\text{stored}} = \frac{1}{2} N_e \kappa \theta_{\max}^2, \tag{3.45}$$

where N_e is the number of bristles that the mass contacts during one cycle of motion. Based on the minimum $x_{\min}$ and maximum $x_{\max}$ value of x during one cycle of motion and the spacing of the bristles, N_e is given by

$$N_e = 2 \left\lfloor \frac{x_{\max} - x_{\min}}{\Delta} \right\rfloor, \tag{3.46}$$

where $\lfloor \cdot \rfloor$ denotes integer part. The dissipated energy calculated from (3.45) is $E_{\text{stored}} = 0.35566$ J.

3.3.4 Approximation of the friction force

The calculation of the DRBM friction force (3.13)-(3.16) requires keeping track of the position of each bristle relative to the body. In order to simplify the calculation of F_f, we note that the friction force of the DRBM is a function of position that resembles

a sawtooth wave as shown in Figure 3.6(a). Thus, the friction force (3.13)-(3.16) can be approximated by the sawtooth wave

$$F_f = \begin{cases} F_f^r,\ v \geq 0, \\ F_f^l,\ v < 0, \end{cases} \tag{3.47}$$

$$F_f^r \approx F_{\min} + \frac{F_{\max} - F_{\min}}{\Delta} \mathrm{mod}\left(x, \Delta\right), \tag{3.48}$$

$$F_f^l \approx -\left(F_{\min} + \frac{F_{\max} - F_{\min}}{\Delta} \mathrm{mod}\left(-x, \Delta\right)\right), \tag{3.49}$$

so that

$$F_f \approx \mathrm{sign}(v)\left(F_{\min} + \frac{F_{\max} - F_{\min}}{\Delta} \mathrm{mod}\left(\mathrm{sign}(v)x, \Delta\right)\right), \tag{3.50}$$

where the constants $F_{\min}$ and $F_{\max}$ determine the minimum and maximum magnitudes of the friction force. The force F_f given by (3.50) is shown as a function of position in Figure 3.10(a) and as a function of velocity in Figure 3.10(b), where the position is prescribed to be $x(t) = A\sin(\omega t)$ and the velocity is $v(t) = A\omega\cos(\omega t)$, where $A = 1$ m and $\omega = 0.01$ rad/s.

3.3.5 Equilibria map

In this section we determine the equilibria of (3.40)-(3.41) arising from the friction force (3.47)-(3.49). The equilibria are found for each constant value $\bar{u}$ of the input $u(t)$. Due to the discontinuity of the friction force for $v = 0$, we use the approach of [96, 97] to analyze the equilibria.

We reformulate (3.40)-(3.41) as a differential inclusion (3.26) with $\boldsymbol{x} = \begin{bmatrix} x & v \end{bmatrix}^{\mathrm{T}}$ and vector fields $\boldsymbol{f}_+(\boldsymbol{x})$ and $\boldsymbol{f}_-(\boldsymbol{x})$ defined by (3.42) and (3.43), respectively. However, $F_{f+} = F_f^r$ and $F_{f-} = F_f^l$ are defined by (3.48) and (3.49), respectively. We set the input $u(t) = \bar{u}$ and determine the equilibria in the sets $\mathcal{V}_+$, $\mathcal{V}_-$, and Σ defined

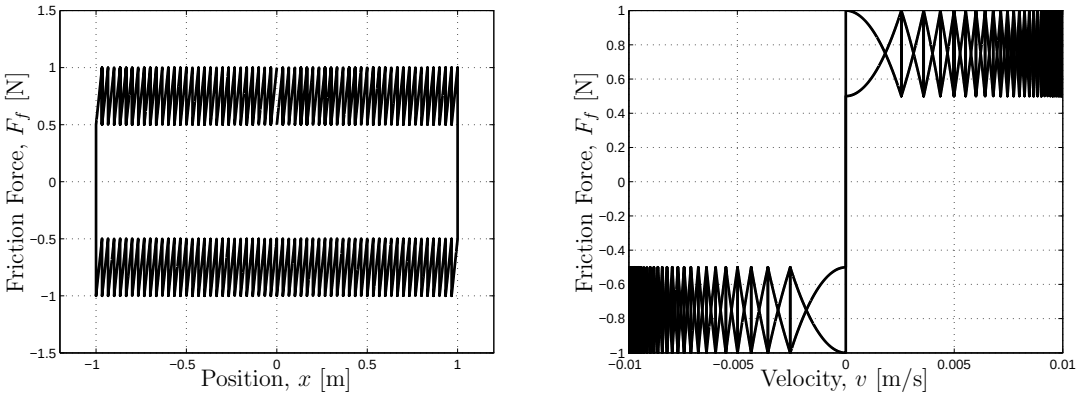

(a) (b)

Figure 3.10: The approximation of the DRBM friction force (3.50) as a function of position (a) and velocity (b). The position is prescribed to be $x(t) = A\sin(\omega t)$ and velocity $v(t) = A\omega\cos(\omega t)$, where $A = 1$ m and $\omega = 0.01$ rad/s. The friction force parameters are $F_{\min} = 0.5$ N, $F_{\max} = 1$ N, and $\Delta = 0.033$ m.

by (3.23), (3.24), and (3.25), respectively, with $g(\boldsymbol{x}) = v$. *The equilibria map* $\mathcal{E}(\bar{u})$ is the set of all points $(\bar{u}, \bar{x}) \in \mathbb{R}^2$, such that $\bar{\boldsymbol{x}} = \begin{bmatrix} \bar{x} & \bar{v} \end{bmatrix}^{\mathrm{T}}$ is an equilibrium of (3.26) corresponding to $u(t) = \bar{u}$.

To find equilibria in $\mathcal{V}_+$, we set $\boldsymbol{f}_+(\boldsymbol{x}) = 0$, which yields

$$\bar{x} = \frac{1}{K}(\bar{u} - F_{f+}), \tag{3.51}$$

$$\bar{v} = 0. \tag{3.52}$$

However, since $\mathcal{V}_+ = \{(x, v) : x \in \mathbb{R},\, v > 0\}$ and $\bar{v} = 0$, the equilibrium $(\bar{x}, \bar{v})$ defined by (3.51) and (3.52) is not an element of $\mathcal{V}_+$, and thus there are no equilibria in $\mathcal{V}_+$. To find the equilibria in $\mathcal{V}_-$, we set $\boldsymbol{f}_-(\boldsymbol{x}) = 0$, which yields

$$\bar{x} = \frac{1}{K}(\bar{u} - F_{f-}), \tag{3.53}$$

$$\bar{v} = 0. \tag{3.54}$$

However, since $\mathcal{V}_- = \{(x, v) : x \in \mathbb{R}, v < 0\}$ and $\bar{v} = 0$, the equilibrium $(\bar{x}, \bar{v})$ defined by (3.53) and (3.54) is not an element of $\mathcal{V}_-$, and thus there are no equilibria in $\mathcal{V}_-$. Finally, to find the equilibria in Σ, we set

$$\mathbf{0} = \alpha \boldsymbol{f}_+(\boldsymbol{x}) + (1 - \alpha)\boldsymbol{f}_-(\boldsymbol{x}), \tag{3.55}$$

for all $\alpha \in [0, 1]$, which yields

$$\bar{x} \in \bar{\mathcal{X}}(\bar{u}) \triangleq \left\{ \frac{\bar{u} - (\alpha F_{f+} + (1 - \alpha)F_{f-})}{K} : \alpha \in [0, 1] \right\}, \tag{3.56}$$

$$\bar{v} = 0. \tag{3.57}$$

Since $\Sigma = \{(x, v) : x \in \mathbb{R}, v = 0\}$, it follows that all of the equilibria of (3.26) with $\boldsymbol{f}_+(\boldsymbol{x})$ and $\boldsymbol{f}_-(\boldsymbol{x})$ defined by (3.42) and (3.43), respectively, are elements of Σ. The equilibria map $\mathcal{E}(\bar{u})$ on the sliding manifold Σ is therefore given by

$$\mathcal{E} \triangleq \{(\bar{u}, \bar{x}) : \bar{u} \in \mathbb{R}, \bar{x} \in \bar{\mathcal{X}}(\bar{u})\}, \tag{3.58}$$

where $\bar{\mathcal{X}}(\bar{u})$ is defined by (3.56). The equilibria $(\bar{u}, \bar{x})$ in Σ are called *pseudo-equilibria* for $\alpha \in (0, 1)$ and *boundary equilibria* for $\alpha = 0$ or $\alpha = 1$ [97]. The set $\mathcal{E}$ is shown in Figure 3.11. The shaded region represents the pseudo-equilibria, and the black lines represent the boundary equilibria. For each constant input $\bar{u}$ there is an infinite number of corresponding pseudo-equilibria $\bar{x} \in \bar{\mathcal{X}}(\bar{u})$. The hysteresis map is also shown in Figure 3.11. Except for the vertical portions, the hysteresis map is a subset of the equilibria map. The vertical portions of the hysteresis map, which correspond to the slip phase, are not completely contained in the equilibria map since they occur at the points of bifurcations. For more details, see [63].

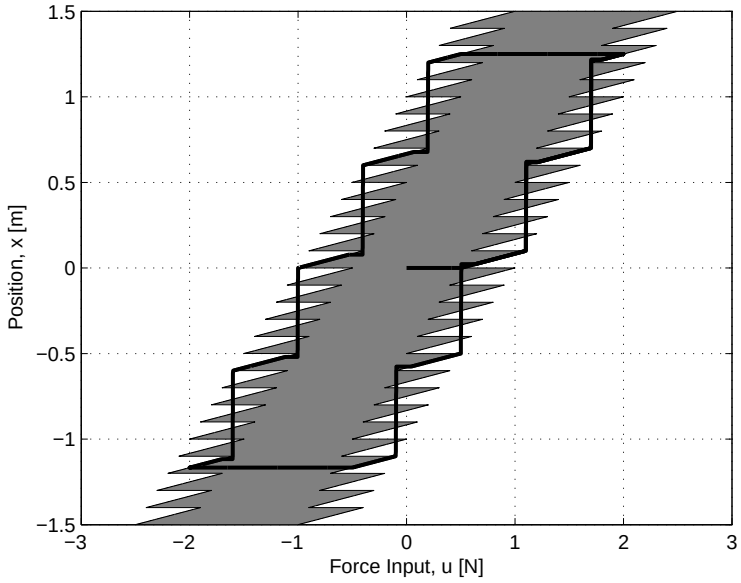

Figure 3.11: Equilibria and hysteresis maps of (3.40)-(3.41) with the friction force modeled by (3.47)-(3.49). The shaded area represents the pseudo-equilibria of the system. The boundary equilibria form the boundary of the shaded area. The hysteresis map, shown in black, is a subset of the equilibria map. The parameters used are $m = 1$ kg, $K = 1$ N/m, $\Delta = 0.1$ m, $F_{\min} = 0.5$ N, and $F_{\max} = 1$ N.

3.4 DRBM-Based Single-State Models

In this section we introduce two simplified versions of the DRBM, namely, the friction-force-based model (FFBM) and the mean-pivot-angle-based model (MPABM). These versions eliminate the need for the Switch Model and yet capture the stick-slip behavior of the DRBM. The FFBM and MPABM are both single-state models [83,93], as described below.

3.4.1 Single-state models

Single-state friction models such as the Dahl and LuGre model involve a state variable z that represents the internal friction mechanism. These models have the

form

$$\dot{z} = v\left(1 - \alpha(v,z)\text{sign}(v)\frac{z}{z_{ss}(v)}\right), \tag{3.59}$$

$$F_f = \sigma_0 z + \sigma_1 \dot{z} + \sigma_2 v, \tag{3.60}$$

where σ_0, σ_1, σ_2 are positive constants, z is the internal friction state, $z_{ss}(v)$ determines the shape of the steady-state z curve, and F_f is the friction force. The function $\alpha(v,z)$ determines the presence and type of elastoplastic presliding displacement [93, 98]. For simplicity, we set $\alpha(v,z) = 1$ and rewrite (3.59)-(3.60) as

$$\dot{z} = v - \frac{|v|}{z_{ss}(v)}z, \tag{3.61}$$

$$F_f = \sigma_0 z + \sigma_1 \dot{z} + \sigma_2 v. \tag{3.62}$$

Setting $z_{ss}(v)$ to be

$$z_{ss}(v) = \frac{1}{\sigma_0}\left(F_c + (F_s - F_c)e^{-(v/v_s)^2}\right), \tag{3.63}$$

where F_c, F_s, and v_s are constants, yields the LuGre model [25, 26], which exhibits stick-slip, hysteresis, and the Stribeck effect.

In steady-state motion, $\dot{z} = 0$, and thus $z = \text{sign}(v)z_{ss}(v)$. Furthermore, if $\sigma_1 = \sigma_2 = 0$, then

$$F_f = \sigma_0 z = \text{sign}(v)\sigma_0 z_{ss}(v). \tag{3.64}$$

3.4.2 Friction-force-based model (FFBM)

The friction-force-based model (FFBM) is formulated by using the approximation (3.50) of the DRBM friction force to define z_{ss}. Equating (3.50) with (3.64) yields

$$z_{ss}(v,x) = \frac{1}{\sigma_0}\left(F_{\min} + \frac{F_{\max}-F_{\min}}{\Delta}\mathrm{mod}\left(\mathrm{sign}(v)x,\Delta\right)\right), \tag{3.65}$$

and thus (3.61)-(3.62) become

$$\dot{z} = v - \sigma_0 \frac{|v|}{F_{\min} + \frac{F_{\max}-F_{\min}}{\Delta}\mathrm{mod}(\mathrm{sign}(v)x,\Delta)} z, \tag{3.66}$$

$$F_f = \sigma_0 z. \tag{3.67}$$

In this case, z has the units of force and can be viewed as the contribution of one bristle to the total friction force, while the total number of bristles contributes to the friction force through the parameter σ_0. Note that, unlike $z_{ss}(v)$ in (3.61), the term $z_{ss}(v,x)$ in (3.65) depends on both position and velocity.

We now consider the system shown in Figure 3.8 and described by (3.40)-(3.41) with the external force $u(t)$ and the friction force modeled by (3.66)-(3.67). The complete system of equations is

$$\dot{x} = v, \tag{3.68}$$

$$\dot{v} = \frac{1}{m}(-Kx + u - F_f), \tag{3.69}$$

$$\dot{z} = v - \sigma_0 \frac{|v|}{F_{\min} + \frac{F_{\max}-F_{\min}}{\Delta}\mathrm{mod}(\mathrm{sign}(v)x,\Delta)} z, \tag{3.70}$$

$$F_f = \sigma_0 z. \tag{3.71}$$

For each constant force input $u(t) = \bar{u}$ the equilibria of (3.68)-(3.71) are

$$\bar{x} = \frac{1}{K}(\bar{u} - \sigma_0 \bar{z}), \tag{3.72}$$

$$\bar{v} = 0, \tag{3.73}$$

$$\bar{z} = \text{sign}(0)\frac{1}{\sigma_0}\left(F_{\min} + \frac{F_{\max} - F_{\min}}{\Delta}\text{mod}\left(\text{sign}(0)\bar{x}, \Delta\right)\right). \tag{3.74}$$

By viewing sign(0) as the interval $[-1,\ 1]$ we rewrite (3.74) as

$$\bar{z} \in \bar{\mathcal{Z}} \triangleq \left\{(2\alpha - 1)\frac{1}{\sigma_0}\left(F_{\min} + \frac{F_{\max} - F_{\min}}{\Delta}\text{mod}\left((2\alpha - 1)\bar{x}, \Delta\right)\right) :\ \alpha \in [0, 1]\right\}. \tag{3.75}$$

Note that (3.75) is equivalent to

$$\bar{z} \in \bar{\mathcal{Z}} \triangleq \left\{\frac{1}{\sigma_0}\left(\alpha F_f^r + (1 - \alpha)F_f^l\right) :\ \alpha \in [0, 1]\right\}, \tag{3.76}$$

where F_f^r and F_f^l are defined by (3.48) and (3.49), respectively. Substituting (3.76) into (3.72) gives the equilibria map of (3.68)-(3.71)

$$\mathcal{E} = \{(\bar{u}, \bar{x}) :\ \bar{u} \in \mathbb{R},\ \bar{x} \in \bar{\mathcal{X}}(\bar{u})\}, \tag{3.77}$$

where

$$\bar{\mathcal{X}}(\bar{u}) = \left\{\frac{\bar{u} - (\alpha F_f^r + (1 - \alpha)F_f^l)}{K} : \alpha \in [0, 1]\right\}, \tag{3.78}$$

which is identical to the equilibria set (3.58) for the DRBM on the sliding manifold.

The equilibria set and the hysteresis map of (3.68)-(3.71) are shown in Figure 3.12. The system is hysteretic and exhibits exact stick-slip, where the exact stick-slip is demonstrated by the staircase-shaped hysteresis map. The parameters used are

$m = 1$ kg, $K = 1$ N/m, $F_{\min} = 1$ N, $F_{\max} = 1.5$ N, $\Delta = 0.05$ m, $u(t) = 2\sin(\omega t)$ N, $\omega = 0.01$ rad/s, $\sigma_0 = 10^5$. The hysteresis map is a subset of the equilibria set, except for the vertical portions, which correspond to the slip phases and occur at bifurcation points [63].

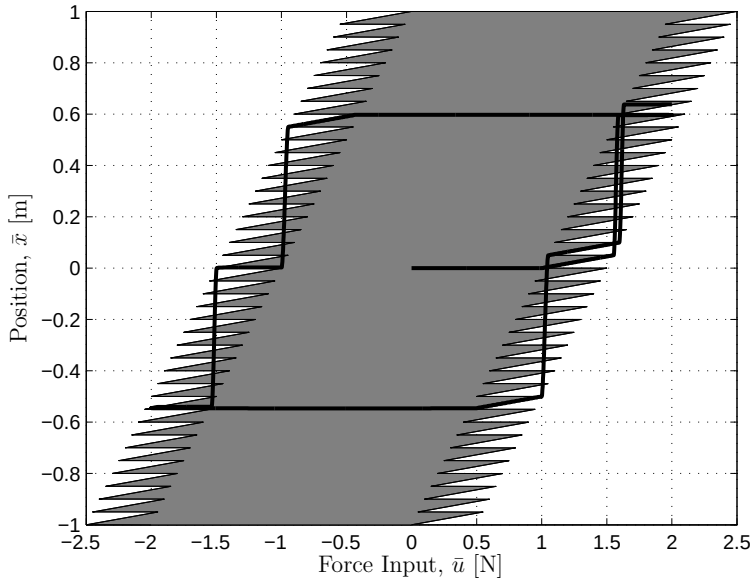

Figure 3.12: Equilibria map and hysteresis map of (3.68)-(3.71) with force input $u(t) = 2\sin(\omega t)$ with $m = 1$ kg, $K = 1$ N/m, $F_{\min} = 1$ N, $F_{\max} = 1.5$ N, $\Delta = 0.05$ m, $\omega = 0.01$ rad/s, and $\sigma_0 = 10^5$.

3.4.3 Mean-pivot-angle-based model (MPABM)

We develop the mean-pivot-angle-based model (MPABM) by assuming that the sum θ_s of the pivot angles θ_i of all of the bristles contributing to the friction force can be approximated by its exponentially weighted moving average (EWMA) $\overline{\theta}$ [99, 100]. The goal is to express $\overline{\theta}$ as a function of v, so that setting $z_{ss}(v) = \overline{\theta}(v)$ yields a single-state friction model.

To find $\overline{\theta}$ at each discrete time step t_j, we use

$$\overline{\theta}(t_j) = \beta\theta_s(t_j) + (1-\beta)\overline{\theta}(t_j - 1), \tag{3.79}$$

where $\beta \in [0,1]$ is a constant, $\overline{\theta}(0) = \theta_s(0)$, and the weighting for the data point $\theta_s(t_j - i)$ is $\beta(1-\beta)^{i-1}$, that is, the weighting for prior data points decreases exponentially [99, 100].

Since $\overline{\theta}$ can be interpreted as a pivot angle of a single bristle that is contributing to the friction force, the vectors Θ_r and Θ_l used to calculate F_f in (3.13) and (3.15) are replaced by $\overline{\theta}$, and (3.13) and (3.15) are replaced by

$$F_f = \frac{\kappa\overline{\theta}(\cos\overline{\theta})^2}{h} \approx \frac{\kappa}{h}\overline{\theta}, \tag{3.80}$$

for small angles $\overline{\theta}$.

We use (3.79) to find $\overline{\theta}$ for the differential inclusion (3.26) with $\boldsymbol{f}_+$ and $\boldsymbol{f}_-$ defined by (3.38)-(3.39), respectively. The sum θ_s of all of the bristle pivot angles is shown in Figure 3.13(a). The model parameters are $m = 1$ kg, $K = 1$ N/m, $v_p = 0.002$ m/s, $d = 0.5$ N, $\kappa = 0.1$ N-m/rad, $h = 0.0995$ m, $l_b = 0.1$ m, $d_0 = 0.01$ m, $\Delta = 0.005$ m, and $\eta = 10^{-8}$. Figure 3.13(b) shows $\overline{\theta}(t_j)$ found from (3.79) with $\beta = 0.05$, as a function of time and Figure 3.13(c) as a function of velocity. The two traces in Figure 3.13(c) represent $\overline{\theta}(t_j)$ corresponding to increasing and decreasing velocity.

As shown by the dashed line in Figure 3.14, the dependence of $\overline{\theta}$ on velocity shown in Figure 3.13(c) can be approximated by

$$\overline{\theta} \approx \hat{\overline{\theta}}(v) \triangleq \text{sign}(v)\left(\hat{\theta}_{\min} + (\hat{\theta}_{\max} - \hat{\theta}_{\min})e^{-(v/\hat{v}_s)^2}\right), \tag{3.81}$$

where $\hat{\theta}_{\min} = 0.1$ rad, $\hat{\theta}_{\max} = 0.133$ rad, and $\hat{v}_s = 0.01$ m/s. The parameters $\hat{\theta}_{\max}$ and $\hat{\theta}_{\min}$ are determined by the values of $\overline{\theta}$ for $v = 0$ m/s and $v \to \infty$, respectively. In addition, the parameter $\hat{v}_s$ reflects the decay rate of $\overline{\theta}$, which is determined by the choice of β. Combining (3.80) and (3.81) yields the mean friction force expression

$$\overline{F_f} = \frac{\kappa}{h}\text{sign}(v)\left(\hat{\theta}_{\min} + (\hat{\theta}_{\max} - \hat{\theta}_{\min})e^{-(v/\hat{v}_s)^2}\right), \tag{3.82}$$

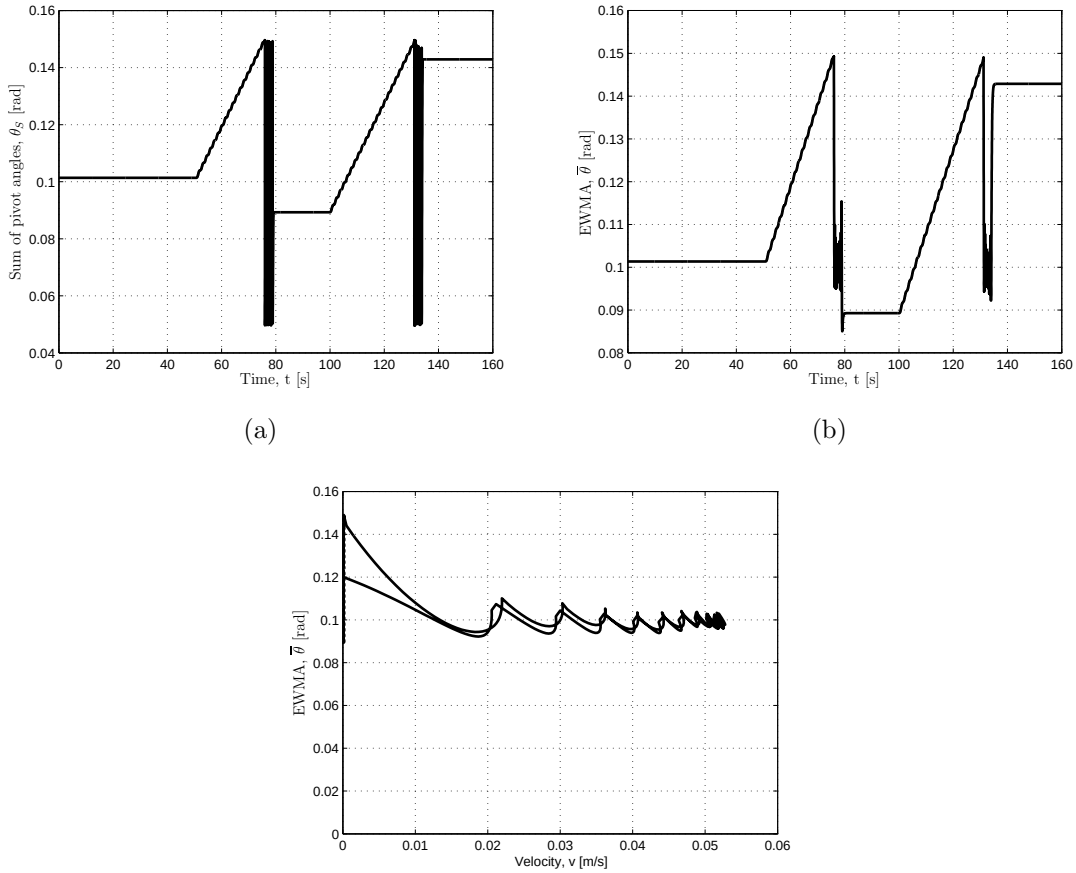

Figure 3.13: Sum of the pivot angles θ_s of all of the bristles contributing to the friction force (a), the EWMA of θ_s as a function of time (b) and as a function of velocity (c). The pivot angle data are obtained from the simulation of (3.38) and (3.39) with parameters $m = 1$ kg, $K = 1$ N/m, $v_p = 0.002$ m/s, $d = 0.5$ N, $\kappa = 0.1$ N-m/rad, $h = 0.0995$ m, $l_b = 0.1$ m, $d_0 = 0.01$ m, $\Delta = 0.005$ m, and $\eta = 10^{-8}$. The EWMA is found from (3.79) with $\beta = 0.05$. The two traces in (c) represent $\overline{\theta}(t_j)$ for increasing and decreasing values of velocity.

so that

$$z_{ss}(v) = \frac{1}{\sigma}\left(\hat{\theta}_{\min} + (\hat{\theta}_{\max} - \hat{\theta}_{\min})e^{-(v/\hat{v}_s)^2}\right), \tag{3.83}$$

and the single-state friction model equations are

$$\dot{z} = v - \sigma \frac{|v|}{\hat{\theta}_{\min} + (\hat{\theta}_{\max} - \hat{\theta}_{\min}) e^{-(v/\hat{v}_s)^2}} z, \tag{3.84}$$

$$F_f = \sigma_0 z, \tag{3.85}$$

where $\sigma_0 = \frac{\kappa}{h}\sigma$. The single-state friction model (3.84)-(3.85) is the LuGre model (3.61)-(3.63) with $\sigma = \sigma_0$, $\sigma_1 = 0$, $\sigma_2 = 0$. Note that, the Stribeck effect of the MPABM is an artifact of the approximation of θ_s by its EWMA $\overline{\theta}$ and is not a property inherited from the DRBM.

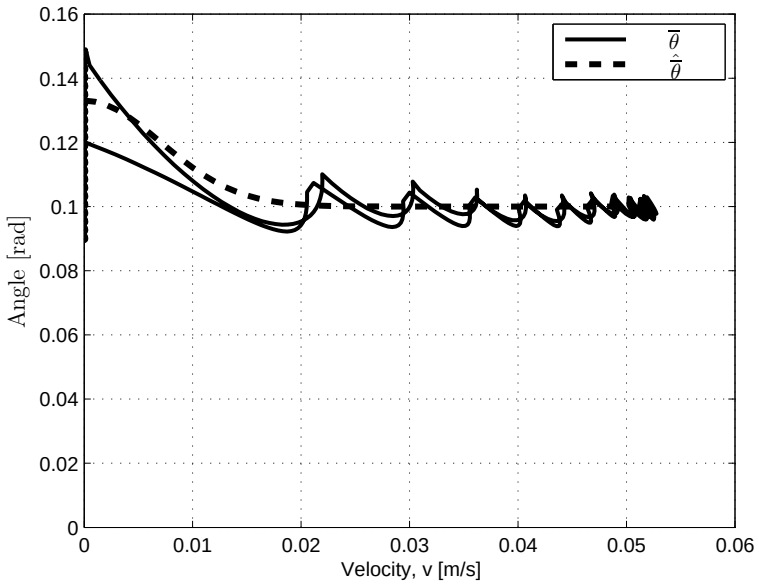

Figure 3.14: The EWMA $\overline{\theta}$ (solid) of the sum of all pivot angles and its approximation $\hat{\overline{\theta}}$ (dashed). The EWMA is found from (3.79) with $\beta = 0.05$ and can be approximated by $\hat{\overline{\theta}} = \text{sign}(v)\left(\hat{\theta}_{\min} + (\hat{\theta}_{\max} - \hat{\theta}_{\min}) e^{-(v/\hat{v}_s)^2}\right)$, where $\hat{\theta}_{\min} = 0.1$ rad, $\hat{\theta}_{\max} = 0.133$ rad, and $\hat{v}_s = 0.01$ m/s.

We use (3.84) and (3.85) to represent the friction force of the system shown in

Figure 3.8 and described by (3.40)-(3.41). The complete description is

$$\dot{x} = v, \tag{3.86}$$

$$\dot{v} = \frac{1}{m}(-Kx + u - F_f), \tag{3.87}$$

$$\dot{z} = v - \sigma \frac{|v|}{\hat{\theta}_{\min} + (\hat{\theta}_{\max} - \hat{\theta}_{\min})e^{-(v/\hat{v}_s)^2}} z, \tag{3.88}$$

$$F_f = \sigma_0 z, \tag{3.89}$$

and, for each constant value of the input $u(t) = \bar{u}$, the equilibria of this system are

$$\bar{x} = \frac{1}{K}(\bar{u} - \sigma_0 \bar{z}), \tag{3.90}$$

$$\bar{v} = 0, \tag{3.91}$$

$$\bar{z} = \text{sign}(0)\frac{1}{\sigma}\hat{\theta}_{\max}. \tag{3.92}$$

By viewing sign(0) as the interval $[-1, 1]$, the equilibria map of (3.86)-(3.89) is the set

$$\mathcal{E} = \{(\bar{u}, \bar{x}) : \bar{u} \in \mathbb{R}, \bar{x} \in \bar{\mathcal{X}}(\bar{u})\}, \tag{3.93}$$

where

$$\bar{\mathcal{X}}(\bar{u}) = \left\{ \frac{1}{K}\left(\bar{u} - \frac{\kappa}{h}(2\alpha - 1)\hat{\theta}_{\max}\right) : \alpha \in [0, 1] \right\}. \tag{3.94}$$

The equilibria set (3.93) and the hysteresis map of the system (3.86)-(3.89) are shown in Figure 3.15 with parameters $u(t) = 2\sin(\omega t)$, $m = 1$ kg, $K = 2$ N/m, $\theta_{\min} = 0.5$ rad, $\theta_{\max} = 0.75$ rad, $\omega = 0.01$ rad/s, $\sigma_0 = 10^5$ N/rad, $\sigma = 10^5$, and $v_s = 0.001$ m/s. The equilibria set is the region shaded gray. For each constant force input $\bar{u}$ there is an infinite number of corresponding equilibria points. Thus, the system is

hysteretic and the hysteresis map is a subset of the equilibria map. Furthermore, the staircase-shaped hysteresis map indicates exact stick-slip motion.

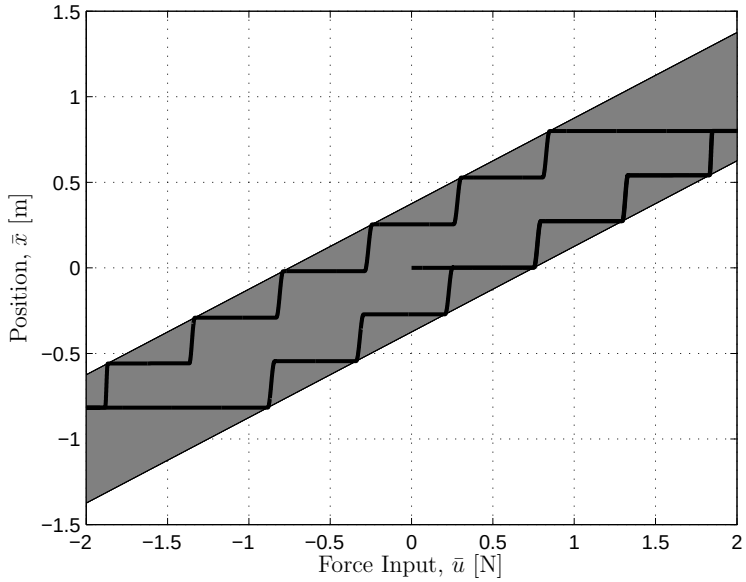

Figure 3.15: Equilibria map and hysteresis map of (3.86)-(3.89) with force input $u(t) = 2\sin(\omega t)$ with $m = 1$ kg, $K = 2$ N/m, $\theta_l = 0.5$ rad, $\theta_h = 0.75$ rad, $\omega = 0.01$ rad/s, $\sigma_0 = 10^5$ N/rad, $\sigma = 10^5$, and $v_s = 0.001$ m/s. The equilibria map forms a continuum shown in gray shade and the hysteresis map is shown in thick black.

3.5 Conclusions

In this chapter we developed an asperity-based friction model. The friction model is based on the frictionless and lossless interaction of a body with a row of rigid bristles that represent the roughness of the contacting surfaces. Each bristle in the rotating bristle model is attached to the ground through a torsional spring and a dashpot. As the body moves, the bristles pivot and counteract its motion, and energy is used to compress the spring at the base of each bristle. As the body passes over each bristle, it is suddenly released, and the energy stored in its spring is dissipated by a dashpot. The resulting energy loss occurs regardless of how slowly the mass moves.

Consequently, the bristle model is hysteretic.

The rotating bristle model exhibits quasi-stick-slip, similar to exact stick-slip but where the stick phase is replaced by reverse motion. Thus, we introduce the discontinuous rotating bristle model (DRBM), which exhibits exact stick-slip and hysteresis and is identical to the rotating bristle model except during direction reversals. The physical mechanism that gives rise to the exact-stick-slip of the DRBM model is the drop in the friction force which occurs when a bristle transitions from contacting the lower corner of the body to contacting the bottom surface of the body. This insight can be used in development of experimentally based friction models that exhibit exact-stick-slip.

We then simplify the DRBM to obtain single-state friction models that are continuous and have the same stick-slip properties as the DRBM. For the FFBM single-state model, the internal friction state represents the contribution of each bristle to the friction force. For the MPABM, the internal friction state is given by the exponentially weighted moving average of the sum of the pivot angles of all of the bristles contributing to the friction force. The FFBM and MPABM models exhibit exact stick-slip and hysteresis and are closely related to the LuGre model. Thus, we show that the frictionless interaction of the bristles and a body results in the friction force that has the properties of experimentally based friction models such as LuGre.

CHAPTER IV

A Frictionless Bristle-Based Friction Model That Exhibits Hysteresis and Dynamic Stribeck Effect

In this chapter we investigate the origin of the Stribeck effect, that is, the drop in the friction force which occurs as velocity increases from zero. We develop an asperity-based friction model and show that the vertical motion of a sliding body leads to the Stribeck effect. The friction model is hysteretic, and the energy-dissipation mechanism is the sudden release of the compressed bristles. We relate this model to the LuGre model. We investigate the Stribeck effect in hopes that a better understanding of this effect leads to a better understanding and prediction of friction. If the origins of the Stribeck effect are known, then this knowledge can be applied in development of experimentally based models, so that they can predict a broad spectrum of behaviors.

4.1 Introduction

Experimental observations provide the primary approach to understanding how friction depends on material properties and the relative motion between the contacting surfaces [8, 20, 21]. For example, the classic paper [21] measures the effect of relative speed, contact pressure, and surface separation on the friction force. Experimental observations lead to the development of empirical models that capture

the macroscopic properties of friction [6, 22, 24–28, 101]. The LuGre model captures stick-slip friction when a sliding object is connected to a stiffness. The LuGre model also exhibits the Stribeck effect [25, 28], which predicts a drop in the friction force as the speed increases.

The approach we take to modeling friction is neither experimental nor empirical, but rather is motivated by asperity-based models [5,31,32,102], in which the asperities represent the microscopic roughness of the contacting surfaces. In this conceptual approach, the goal is to postulate a model consisting of many degrees of freedom (for example, bristle deflections), where each component has precisely defined mechanical properties. The analysis and simulation of this model then gives rise to an emergent macroscopic friction force whose properties can be traced back to the properties of the components.

An advantage of this approach is that the hysteretic energy-dissipation mechanism is exposed. For example, in the compressed bristle model presented here, the energy dissipation at asymptotically low frequency [55] is due to the sudden release of the compressed bristles, just as in the rotating bristle model discussed in [94, 103]. As the body encounters each bristle, energy is stored in the compressed spring and is subsequently dissipated by the dashpot due to the post-release oscillation of the bristle. Although the LuGre model [22] is hysteretic, the hysteretic mechanism is not exposed. Additionally, since the bristles represent the asperities of the contacting surface, the compression of the bristles is analogous to plastic deformation of the asperities, which also results in the loss of energy.

The goal of the present paper is to construct a bristle model that exhibits both stick-slip behavior and the Stribeck effect. Stick-slip behavior is exhibited by the rotating bristle model given in [94, 103]; however, the Stribeck effect was not found to be a property of that model.

The Stribeck effect is the apparent drop in the friction force as the velocity in-

creases. In wet friction, the Stribeck effect can be attributed to the phenomenon of *planing* [104–106], where the friction between a tire and a wet surface decreases with velocity, resulting in a dangerous situation. For a boat on water, the same phenomenon is more apparent since the boat rises as its speed increases, thus reducing its contact area, which in turn reduces the drag due to the water, that is, the viscous friction force. For a vehicle immersed in a fluid, such as an aircraft, however, we would not expect to see the Stribeck effect. The Stribeck effect thus depends on contact at the boundary of a fluid and motion orthogonal to the surface of the fluid.

In modeling dry friction, which is the objective of a bristle model, it seems plausible in analogy with wet friction that the Stribeck effect would be observed as long as the mass is given a vertical degree of freedom. In particular, by extending the bristle model in [94,103] to include a vertical degree of freedom, we would expect to observe the Stribeck effect due to the fact that the moment arm is increased—and thus the friction force is decreased—as the height of the mass above the contacting surface increases.

Rather than revisit the rotating bristle model of [94, 103], in the present paper we develop an alternative bristle model in which each bristle has a vertical degree of freedom rather than a rotational degree of freedom. This model gives rise to the Stribeck effect. Somewhat surprisingly, and unlike the Stribeck effect captured empirically by the LuGre model [94,103], the Stribeck effect captured by this bristle model is dynamic in the sense that the speed/friction-force curve forms a loop. We call this the *dynamic Stribeck effect*.

The contents of the paper are as follows. In Section 4.2 we introduce the compressed bristle model, derive the governing equations and show that the compressed bristle model exhibits stick-slip, hysteresis, and the dynamic Stribeck effect. Based on the observations in Section 4.2, we capture the steady-state characteristics of the compressed bristle model in the form of a single-state friction model in Section 4.3.

We show that a simplified version of the compressed bristle model is equivalent to the LuGre model.

4.2 Compressed Bristle Model

In this section we present the compressed bristle model, which is based on the frictionless contact between a body and a row of bristles. The friction force of the compressed bristle model is generated through the frictionless interaction between a body and bristles as shown in Figure 4.1. We assume that the body has mass m, length d, and thickness w, and that its front end is slanted from the vertical by the angle α. The body is allowed to move in the horizontal and vertical directions, but it does not rotate. The horizontal position of the midline of the body is denoted by x, and the vertical position of the midline of the body is denoted by y. The bristles consist of a frictionless roller, a spring with stiffness coefficient k, and a dashpot with damping coefficient c. The damping coefficient provides viscous energy dissipation but negligible force. The mass of the roller is assumed to be negligible compared to the mass of the body. Therefore, the interaction between each bristle and the body is dominated by the stiffness of the bristle. The distance between adjacent bristles is Δ, the position of the ith bristle is denoted by x_{b_i}, and its length is h_i. Each bristle has length h_0 when relaxed. As the body moves, the bristles are compressed, which results in a reaction force at the point of contact between the bristle and the body. The friction force is the sum of all horizontal components of the forces exerted by all of the bristles contacting the slanted surface of the body. The vertical components of the forces exerted by the bristles contacting the body affect the vertical motion of the body.

As the body moves, there is a frictionless reaction force between each bristle and the body at the point of contact. This force is due to the compression of the bristle. We assume that the force on the body due to contact with the bristle is perpendicular

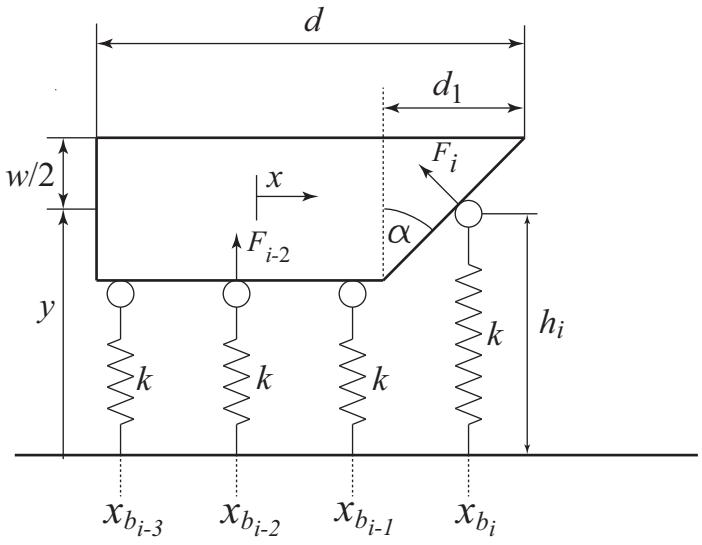

Figure 4.1: Schematic representation of the compressed bristle model. Each bristle consists of a frictionless roller of negligible mass, a linear spring with stiffness coefficient k, and a dashpot with damping coefficient c (not shown). As the body moves over the bristles, the springs in the bristles are compressed, and a reaction force occurs at the point of contact.

to the surface of the body. The sum of all horizontal forces exerted by the bristles at each instant is defined to be the friction force. Since the bristle-body contact is frictionless, the direction of the reaction force between the body and each bristle contacting the horizontal surface of the body is vertical, and thus these bristles do not contribute to the friction force. Only the bristles that are in contact with the slanted surface of the body contribute to the friction force.

The force between the body and each bristle is calculated based on the position of the bristle relative to the body and the resulting length of the compressed bristle. The reaction forces due to the dashpot are neglected. The dashpots and mass of the bristles provide the mechanism for dissipating the energy stored in the compressed springs, but otherwise play no role in the bristle-body interactions.

In simulations of the compressed bristle model we assign numerical values to the bristle-related parameters, such as Δ and k. However, these values do not necessarily

represent physically meaningful quantities, but rather serve only to illustrate the interaction between the body and the asperities.

4.2.1 Friction Force

In this section we analyze the interaction between the body and the bristles, and we derive equations for the friction force of the compressed bristle model. For simplicity, we assume that at the instant the velocity of the body passes through zero, the body instantaneously rotates about the vertical axis that defines the horizontal position x of the body, so that its slanted surface always points in the direction of motion and such that x and y remain constant during the direction reversal.

The length h_i of the ith bristle contacting the slanted surface of the body is a function of the horizontal position x and velocity v of the body as described by

$$h_i(x, v, y) \triangleq \begin{cases} h_{i+}(x, y), \; v \geq 0, \\ h_{i-}(x, y), \; v < 0, \end{cases} \tag{4.1}$$

where

$$h_{i+}(x, y) = y - \frac{w}{2} + \frac{w}{d_1}\left(x_{b_i} - \left(x + \frac{d}{2} - d_1\right)\right), \tag{4.2}$$

$$h_{i-}(x, y) = y - \frac{w}{2} + \frac{w}{d_1}\left(x - \frac{d}{2} + d_1 - x_{bi}\right), \tag{4.3}$$

and $d_1 \triangleq w \tan(\alpha)$ as shown in Figure 4.1. The magnitude of the force due to the ith bristle is

$$F_i(x, v, y) = k(h_0 - h_i(x, v, y)). \tag{4.4}$$

The magnitude of the horizontal component of the reaction force due to the ith bristle

is

$$F_{ix}(x, v, y) = k\cos(\alpha)(h_0 - h_i(x, v, y)), \tag{4.5}$$

while the magnitude of the vertical component of reaction force due to the ith bristle is

$$F_{iy}(x, v, y) = k\sin(\alpha)(h_0 - h_i(x, v, y)). \tag{4.6}$$

The friction force is the sum of all of the horizontal components of the reaction forces between the bristles and the body. Only the bristles that are in contact with the slanted surface of the body exert a force with a horizontal component. The base positions x_{b_i} of the bristles that contribute to the friction force for $v \geq 0$ are in the set

$$\mathcal{X}_{b+}(x) = \{x_{b_i} : x + \frac{d}{2} - d_1 \leq x_{b_i} \leq x + \frac{d}{2}\}, \tag{4.7}$$

and, for $v < 0$, are in the set

$$\mathcal{X}_{b-}(x) = \{x_{b_i} : x - \frac{d}{2} \leq x_{b_i} \leq x - \frac{d}{2} + d_1\}. \tag{4.8}$$

Thus, for $v \geq 0$, the friction force is

$$F_f(x, v, y) = F_{f+}(x, y), \tag{4.9}$$

where

$$F_{f+}(x, y) = k\cos(\alpha)\sum_{i=1}^{n_+}(h_0 - h_{i+}(x, v, y)), \tag{4.10}$$

and n_+ is the number of elements of $\mathcal{X}_{b+}(x)$. For $v < 0$, the friction force is

$$F_f(x, v, y) = F_{f-}(x, y), \tag{4.11}$$

where

$$F_{f-}(x, y) = -k \cos(\alpha) \sum_{i=1}^{n_-} (h_0 - h_{i-}(x, v, y)), \tag{4.12}$$

where n_- is the number of elements of $\mathcal{X}_{b-}(x)$. Expressions (4.9) and (4.11) can be combined, so that $F_f(x, v, y)$ is given by

$$F_f(x, v, y) = \text{sign}(v) k \cos(\alpha) \sum_{i=1}^{n} (h_0 - h_i(x, v, y)), \tag{4.13}$$

where n is the number of elements of $\mathcal{X}_{b+}(x)$ for $v \geq 0$ and of $\mathcal{X}_{b-}(x)$ for $v < 0$. Note that, due to the function sign(v), (4.13) is discontinuous at $v = 0$.

The vertical force due to the bristles contacting the slanted surface of the body is equal to the sum of all of the vertical components of the reaction forces between the body and the bristles contacting the slanted surface of the body. We define the vertical force due to bristles contacting the slanted surface of the body as

$$F_{ys}(x, v, y) = \begin{cases} F_{ys+}(x, y), \ v \geq 0, \\ F_{ys-}(x, y), \ v < 0, \end{cases} \tag{4.14}$$

where

$$F_{ys+}(x, y) = k \sin(\alpha) \sum_{i=1}^{n_+} (h_0 - h_{i+}(x, v, y)), \tag{4.15}$$

$$F_{ys-}(x, y) = k \sin(\alpha) \sum_{i=1}^{n_-} (h_0 - h_{i-}(x, v, y)). \tag{4.16}$$

The magnitude of the vertical force due to the bristles contacting the horizontal surface of the body is

$$F_{yb}(y) = \sum_{i=1}^{N} k\left(h_0 - \left(y - \frac{w}{2}\right)\right) = Nk\left(h_0 - y + \frac{w}{2}\right), \tag{4.17}$$

where $N \triangleq \frac{d - d_1}{\Delta} + 1$ is the number of bristles that are in contact with the horizontal surface of the body.

4.2.2 Equations of motion

The goal is to investigate the stick-slip and input-output properties of the compressed bristle model. To investigate the emergence of stick-slip, we consider the system shown in Figure 4.2. The body of mass m is connected to a spring with stiffness K, and the free end of the spring moves at the constant speed v_p. The equations of motion describing the mass-spring system in Figure 4.2 are

$$\dot{x}(t) = v(t), \tag{4.18}$$

$$\dot{v}(t) = \frac{1}{m}(Kl(t) - F_f(x, v, y)), \tag{4.19}$$

$$\dot{l}(t) = v_p - v(t), \tag{4.20}$$

where l is the length of the spring and $F_f(x, v, y)$ is the friction force (4.13).

Since the compressed bristle model accounts for horizontal and vertical motion of the body, we augment (4.18)-(4.20) with vertical-direction equations of motion. The vertical motion of the body is described by

$$m\ddot{y} = -mg + F_y(x, v, y), \tag{4.21}$$

$$F_y(x, v, y) = F_{ys}(x, v, y) + F_{yb}(y), \tag{4.22}$$

where F_{ys} and F_{yb} are defined by (4.14) and (4.17), respectively. Note that (4.21)-(4.22) can be rewritten as

$$m\ddot{y}(t) + k_{uo}y(t) = f(t), \tag{4.23}$$

where, for $v \geq 0$, $k_{uo} = Nk + n_+ k \sin\alpha$ and

$$f = Nk(h_0 + \frac{w}{2}) - mg + k\sin\alpha \sum_{i=1}^{n_+} \left(h_0 + \frac{w}{2} - \frac{w}{d_1}\left(x_{b_i} - x - \frac{d}{2} + d_1 \right) \right), \tag{4.24}$$

and, for $v < 0$, $k_{uo} = Nk + n_- k \sin\alpha$ and

$$f = Nk(h_0 + \frac{w}{2}) - mg + k\sin\alpha \sum_{i=1}^{n_-} \left(h_0 + \frac{w}{2} - \frac{w}{d_1}\left(x - \frac{d}{2} + d_1 - x_{b_i} \right) \right). \tag{4.25}$$

Thus (4.21)-(4.22) describe an undamped oscillator.

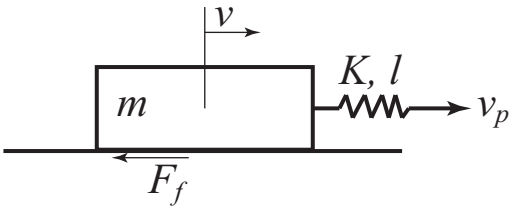

Figure 4.2: Schematic representation of the mass-spring system used to investigate the stick-slip properties of the compressed bristle model. The body of mass m is connected to a spring with stiffness K. The free end of the spring moves at constant speed v_p. The friction force F_f is given by (4.13).

To investigate the input-output properties and the emergence of hysteresis, we consider the mass-spring system shown in Figure 4.3. The body of mass m is connected to a wall by means of a spring with stiffness K and acted on by the force input

$u(t)$. The equations of motion are

$$\dot{x}(t) = v(t), \tag{4.26}$$

$$\dot{v}(t) = \frac{1}{m}(-Kx(t) + u(t) - F_f(x, v, y)), \tag{4.27}$$

where $F_f(x, v, y)$ is the compressed bristle model friction force (4.13). Furthermore, the vertical motion of the body is described by (4.21)-(4.22).

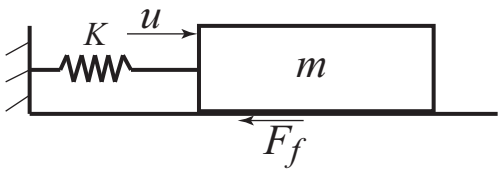

Figure 4.3: Body-spring configuration used to investigate the input-output properties of the compressed bristle model. The body of mass m is connected to the wall by a means of a spring with stiffness K and is acted on by the periodic force input $u(t)$. The friction force F_f is given by (4.13).

4.2.3 Switch Model

Due to the discontinuity of the compressed bristle model friction force (4.13) at $v = 0$, the integration (4.18)-(4.22) and (4.22)-(4.27) with the friction force represented by the compressed bristle model (4.13) requires special numerical techniques. In this section we describe the Switch Model [88, 95], which is a technique that smooths out the discontinuous dynamics around the discontinuity $v = 0$. The modified equations can then be integrated using standard numerical integration techniques.

To begin, we rewrite the equations of motion in which the friction force is modeled by the compressed bristle model as a differential inclusion [95]. Assume that the motion of the body is described by

$$\dot{\boldsymbol{x}} = \boldsymbol{f}(\boldsymbol{x}), \tag{4.28}$$

where $\boldsymbol{x} \in \mathbb{R}^m$ and $\boldsymbol{f} : \mathcal{V} \subset \mathbb{R}^m \to \mathbb{R}^m$ is a piecewise continuous vector field, and $\Sigma \triangleq \mathbb{R}^m \backslash \mathcal{V}$ is the set of points of discontinuity of $\boldsymbol{f}$. We assume that there exists a function $g : \mathbb{R}^m \to \mathbb{R}$ such that the discontinuity boundary Σ is given by the roots of g, that is

$$\Sigma = \{\boldsymbol{x} \in \mathbb{R}^m : \ g(\boldsymbol{x}) = 0\}. \tag{4.29}$$

We also define sets

$$\mathcal{V}_+ \triangleq \{\boldsymbol{x} \in \mathbb{R}^m : \ g(\boldsymbol{x}) > 0\}, \tag{4.30}$$

$$\mathcal{V}_- \triangleq \{\boldsymbol{x} \in \mathbb{R}^m : \ g(\boldsymbol{x}) < 0\}. \tag{4.31}$$

With these definitions, (4.28) can be rewritten as the differential inclusion [95, 96]

$$\dot{\boldsymbol{x}} \in \begin{cases} \boldsymbol{f}_+(\boldsymbol{x}), \ \boldsymbol{x} \in \mathcal{V}_+, \\ \alpha \boldsymbol{f}_+(\boldsymbol{x}) + (1-\alpha)\boldsymbol{f}_-(\boldsymbol{x}), \ \boldsymbol{x} \in \Sigma, \ \alpha \in [0,1], \\ \boldsymbol{f}_-(\boldsymbol{x}), \ \boldsymbol{x} \in \mathcal{V}_-. \end{cases} \tag{4.32}$$

The direction of the flow given by the vector fields $\boldsymbol{f}_+(\boldsymbol{x})$ and $\boldsymbol{f}_-(\boldsymbol{x})$ can lead to three types of sliding modes across Σ. If the flow is such that the solutions of (4.32) are pushed to Σ in both $\mathcal{V}_+$ and $\mathcal{V}_-$, then the sliding mode is *attractive*. If the solutions cross Σ, then the sliding mode is *transversal*. Finally, if the solutions diverge from Σ, the sliding mode is *repulsive* [95].

The Switch Model smooths out the dynamics of the differential inclusion (4.32) by constructing a *stick band* within the set $\mathcal{G} \triangleq \{\boldsymbol{x} : |g(\boldsymbol{x})| \leq \eta\}$, where η is a small positive constant. (Note that the term "stick band" is not related to stick-slip friction.) The dynamics outside of the stick band remain the same. The dynamics inside the stick band depend on the type of sliding mode across the discontinuity

boundary. If the sliding mode is attractive, that is,

$$\boldsymbol{n}^{\mathrm{T}}\boldsymbol{f}_{-}(\boldsymbol{x}) > 0 \text{ and } \boldsymbol{n}^{\mathrm{T}}\boldsymbol{f}_{+}(\boldsymbol{x}) < 0, \quad \boldsymbol{x} \in \Sigma, \tag{4.33}$$

where $\boldsymbol{n} \triangleq \nabla g(\boldsymbol{x})$ is the normal to Σ, then the stick-band dynamics are given by

$$\dot{\boldsymbol{x}} = \alpha \boldsymbol{f}_{+}(\boldsymbol{x}) + (1-\alpha)\boldsymbol{f}_{-}(\boldsymbol{x}), \; \boldsymbol{x} \in \mathcal{G}. \tag{4.34}$$

The value of the parameter α is chosen such that it pushes the solutions of (4.33) toward the middle of the stick band, that is, toward $g(\boldsymbol{x}) = 0$. Thus, inside the stick band, g satisfies

$$\dot{g}(\boldsymbol{x}) = -\tau g(\boldsymbol{x}), \tag{4.35}$$

where $\tau > 0$ is a time constant. Since

$$\dot{g}(\boldsymbol{x}) = \frac{dg(\boldsymbol{x})}{d\boldsymbol{x}}\frac{d\boldsymbol{x}}{dt} = \nabla \boldsymbol{g}^{T}\dot{\boldsymbol{x}} \tag{4.36}$$

$$= \boldsymbol{n}^{T}\left(\alpha \boldsymbol{f}_{+}(\boldsymbol{x}) + (1-\alpha)\boldsymbol{f}_{-}(\boldsymbol{x})\right), \tag{4.37}$$

setting (4.35) equal to (4.37) and solving for α gives

$$\alpha = \frac{\boldsymbol{n}^{T}\boldsymbol{f}_{-}(\boldsymbol{x}) + \tau^{-1}g(\boldsymbol{x})}{\boldsymbol{n}^{T}(\boldsymbol{f}_{-}(\boldsymbol{x}) - \boldsymbol{f}_{+}(\boldsymbol{x}))}. \tag{4.38}$$

If the sliding mode is transversal, that is,

$$(\boldsymbol{n}^{\mathrm{T}}\boldsymbol{f}_{-}(\boldsymbol{x}))(\boldsymbol{n}^{\mathrm{T}}\boldsymbol{f}_{+}(\boldsymbol{x})) > 0, \quad \boldsymbol{x} \in \Sigma, \tag{4.39}$$

then the stick-band dynamics are defined by

$$\dot{\boldsymbol{x}} = \begin{cases} \boldsymbol{f}_-(\boldsymbol{x}), \text{ if } \boldsymbol{n}^{\mathrm{T}}\boldsymbol{f}_-(\boldsymbol{x}) < 0 \text{ and } \boldsymbol{n}^{\mathrm{T}}\boldsymbol{f}_+(\boldsymbol{x}) < 0\,,\ \boldsymbol{x} \in \mathcal{G}, \\ \boldsymbol{f}_+(\boldsymbol{x}), \text{ if } \boldsymbol{n}^{\mathrm{T}}\boldsymbol{f}_-(\boldsymbol{x}) > 0 \text{ and } \boldsymbol{n}^{\mathrm{T}}\boldsymbol{f}_+(\boldsymbol{x}) > 0\,,\ \boldsymbol{x} \in \mathcal{G}. \end{cases} \tag{4.40}$$

Finally, if the sliding mode is repulsive, that is,

$$\boldsymbol{n}^{\mathrm{T}}\boldsymbol{f}_-(\boldsymbol{x}) < 0 \text{ and } \boldsymbol{n}^{\mathrm{T}}\boldsymbol{f}_+(\boldsymbol{x}) > 0, \quad \boldsymbol{x} \in \Sigma, \tag{4.41}$$

than the dynamics are defined by

$$\dot{\boldsymbol{x}} = \boldsymbol{f}_+(\boldsymbol{x})\,,\ \boldsymbol{x} \in \mathcal{G}. \tag{4.42}$$

Outside of the stick band, the dynamics are defined by

$$\dot{\boldsymbol{x}} = \begin{cases} \boldsymbol{f}_+(\boldsymbol{x}),\ \boldsymbol{x} \in \mathcal{G}_+, \\ \boldsymbol{f}_-(\boldsymbol{x}),\ \boldsymbol{x} \in \mathcal{G}_-, \end{cases} \tag{4.43}$$

where $\mathcal{G}_+ \triangleq \{\boldsymbol{x} : g(\boldsymbol{x}) > \eta\}$ and $\mathcal{G}_- \triangleq \{\boldsymbol{x} : g(\boldsymbol{x}) < \eta\}$. More details about the Switch Model (4.33)-(4.43) and a pseudocode are given in [95].

4.2.4 Stick-slip behavior

In this section we consider the stick-slip behavior of the compressed bristle model (4.13) by investigating the existence of a stable limit cycle when the compressed bristle model is used to represent the friction force in the system (4.18)-(4.20) shown in Figure 4.2 with the vertical motion described by (4.21)-(4.22).

We use the Switch Model (4.33)-(4.43) to simulate the system (4.18)-(4.22) with friction force defined by (4.13). The system (4.18)-(4.22) can be formulated as

the differential inclusion (4.32) with $\boldsymbol{x} = \begin{bmatrix} x & v & l & y & \dot{y} \end{bmatrix}^{\mathrm{T}}$, the set Σ defined by the roots of the function $g(\boldsymbol{x}) = v$, the normal to Σ defined by $\boldsymbol{n} \triangleq \nabla g(\boldsymbol{x}) = \begin{bmatrix} 0 & 1 & 0 & 0 & 0 \end{bmatrix}^{\mathrm{T}}$, and the vector fields $\boldsymbol{f}_+(\boldsymbol{x})$ and $\boldsymbol{f}_-(\boldsymbol{x})$ defined as

$$\boldsymbol{f}_+(\boldsymbol{x}) \triangleq \begin{bmatrix} v \\ \frac{1}{m}(Kl - F_{f+}(x,y)) \\ v_p - v \\ \dot{y} \\ -mg + F_{y+}(x,y) \end{bmatrix}, \tag{4.44}$$

$$\boldsymbol{f}_-(\boldsymbol{x}) \triangleq \begin{bmatrix} v \\ \frac{1}{m}(Kl - F_{f-}(x,y)) \\ v_p - v \\ \dot{y} \\ -mg + F_{y-}(x,y) \end{bmatrix}, \tag{4.45}$$

where $F_{f+}(x,y)$ and $F_{f-}(x,y)$ are defined by (4.10) and (4.12), respectively, and

$$F_{y+}(x,y) \triangleq F_{ys+}(x,y) + F_{yb}(y), \tag{4.46}$$

$$F_{y-}(x,y) \triangleq F_{ys-}(x,y) + F_{yb}(y), \tag{4.47}$$

where $F_{ys+}(x,y)$ is defined by (4.15) and $F_{ys-}(x,y)$ by (4.16).

Figure 4.4(a) shows the projection of the trajectories of (4.44)-(4.45) onto the l-v plane, obtained by using the Switch Model (4.33)-(4.43), with parameter values $m = 1$ kg, $w = 1$ m, $d = 2$ m, $\alpha = 15°$, $K = 5$ N/m, $N = 500$, $k = 0.01$ N/m, $h_0 = 2.69$ m, $\eta = 10^{-6}$, and $v_p = 0.1$ m/s. In this plane, the trajectory converges to a stable limit cycle that includes a line segment on which the motion is given by $v = 0$ and $\dot{l} = v_p$. This segment corresponds to the "stick" phase, during which the body is stationary.

The "slip" phase corresponds to the curved part of the limit cycle for which $v \neq 0$. The time histories of the spring length, velocity, height, and position of the body are shown in Figure 4.4(b). Note that the velocity is characterized by segments in which the velocity is zero and segments in which velocity quickly increases. This behavior is typical for stick-slip motion.

The time history of the friction force and plots of the friction force versus height y and versus velocity v are shown in Figure 4.5. This figure also shows the relationship between the height y and velocity v. The friction force is a decreasing function of height, which is consistent with the experimental results presented in [6, 20, 21] as well as the expression (4.13). In the compressed bristle model, as the height increases, compression of the bristles from their relaxed length h_0 decreases. Thus, the friction force decreases also. Furthermore, the friction force decreases as the velocity increases. The velocity/friction-force curve forms a loop, which we refer to as the *dynamic Stribeck effect*. The height versus velocity plot in Figure 4.5 shows that the velocity increases with height. That is, the body moves higher as it speeds up, and it moves lower as it slows down. This is planing.

4.2.5 Physical mechanism that leads to the dynamic Stribeck effect

In the vertical direction, the system consisting of the body and the bristles described by (4.21)-(4.22) represents an undamped oscillator. Thus, if the body is initially not in a vertical equilibrium or if it is slightly disturbed from an equilibrium position, then it oscillates vertically whether or not it is moving horizontally. Since the friction force (4.13) depends linearly on the height y through $h_i(x, v, y)$, the vertical oscillation of the body results in oscillation of the magnitude of the friction force F_f defined by (4.13). The oscillations in F_f are visible in Figure 4.5. The horizontal velocity increases with y because the friction force F_f decreases as y increases, and thus the horizontal acceleration of the body increases. The opposite happens when y

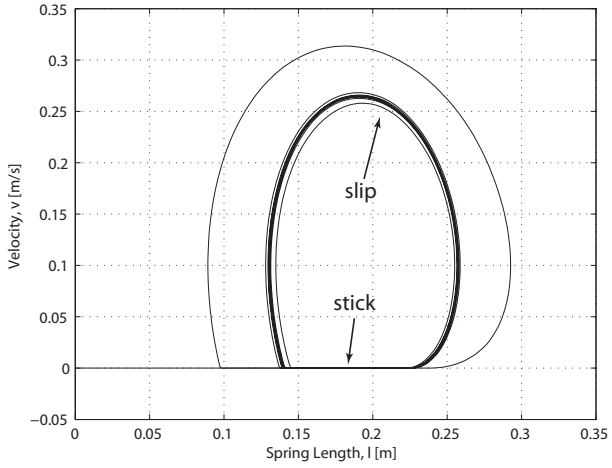

(a)

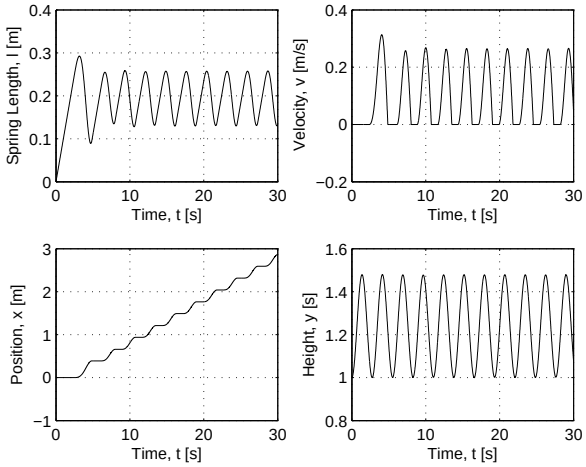

(b)

Figure 4.4: The stick-slip limit cycle and time histories of the spring length l, velocity v, position x, and height y for the system (4.44)-(4.45) with F_f modeled by (4.13). (a) shows the limit cycle and (b) shows the time histories of the states. The trajectories projected onto the l-v plane form a stable limit cycle. The parameter values are $m = 1$ kg, $w = 1$ m, $d = 2$ m, $\alpha = 15°$, $K = 5$ N/m, $N = 500$, $k = 0.01$ N/m, $h_0 = 2.69$ m, $\eta = 10^{-6}$, and $v_p = 0.1$ m/s.

decreases.

Furthermore, as seen in Figure 4.5, the drop in the friction force that occurs when a single bristle transitions from contacting the slanted surface of the body to contacting

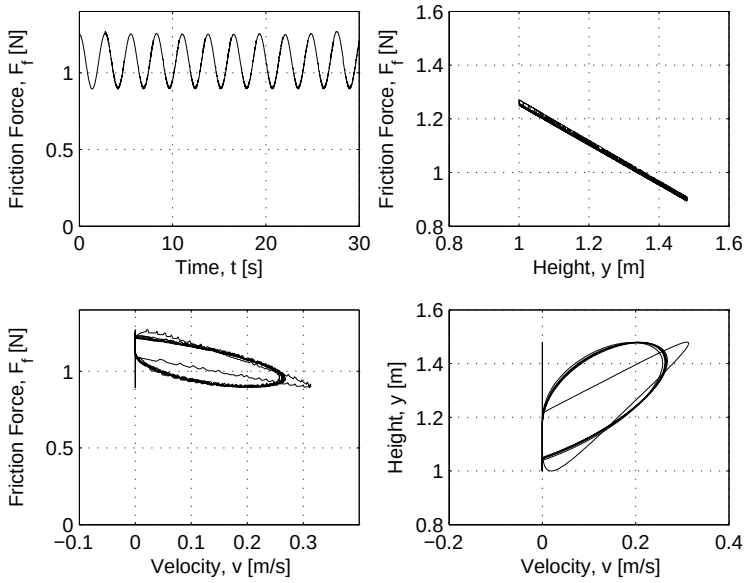

Figure 4.5: The friction force of the compressed bristle model. The figure shows the dependence of the friction force on time t, height y, and velocity v. The bottom left plot shows the dynamic Stribeck effect, while the bottom right plot shows the velocity-height curve.

the horizontal surface of the body is small compared to the amplitude of oscillation of the friction force due to vertical oscillation of the body. As the amplitude of the vertical oscillation of the body decreases, the change in friction force due to a bristle transition from contacting the slanted surface of the body to contacting the horizontal surface of the body becomes the mechanism that leads to stick-slip. In comparison with the discontinuous rotating bristle model [94, 103], the individual bristles do not have a visible effect on the stick-slip behavior or the dynamic Stribeck effect of the compressed bristle model.

To demonstrate, we simulate (4.18)-(4.20) with the friction force (4.13). However, in the vertical direction we assume that the body oscillates according to $y(t) = A\sin(\omega t)$. We use the Switch Model (4.33)-(4.43), and reformulate (4.18)-(4.20) as a

differential inclusion with $\boldsymbol{f}_+$ and $\boldsymbol{f}_-$ defined by

$$\boldsymbol{f}_+(\boldsymbol{x}) \stackrel{\triangle}{=} \begin{bmatrix} v \\ \frac{1}{m}(Kl - F_{f+}(x,y)) \\ v_p - v \end{bmatrix}, \tag{4.48}$$

$$\boldsymbol{f}_-(\boldsymbol{x}) \stackrel{\triangle}{=} \begin{bmatrix} v \\ \frac{1}{m}(Kl - F_{f-}(x,y)) \\ v_p - v \end{bmatrix}, \tag{4.49}$$

where $F_{f+}(x,y)$ is defined by (4.10) and $F_{f-}(x,y)$ is defined by (4.12).

The results are shown in Figure 4.6 for $A = 0.3$ m and $A = 1.3$ m and for $\omega = 6.8$ rad/s. This frequency of oscillation is approximately equal to the natural frequency of the vertical oscillations of the body shown in Figure 4.4(b). The parameter values used are $m = 1$ kg, $K = 2$ N/m, $w = 1$ m, $d = 2$ m, $\alpha = 15°$, $N = 100$, $k = 0.05$ N/m, and $h_0 = 4.46$ m. Note that the dynamic Stribeck effect as well as the dependence of velocity on the height y of the body are more prominent for larger values of A. Also, once the body begins moving horizontally, the friction force becomes less smooth, that is, there are small drops in the friction force that correspond to the transition of a bristle from contacting the slanted surface of the body to contacting the horizontal surface of the body.

4.2.6 Hysteresis map

In this section we analyze the input-output properties of the compressed bristle model. We consider the mass-spring configuration shown in Figure 4.3 and described by (4.21)-(4.27). We use the Switch Model (4.33)-(4.43) to smooth out the discontinuity in the compressed bristle model friction force (4.13).

The system (4.21)-(4.27) can be formulated as a differential inclusion (4.32) with

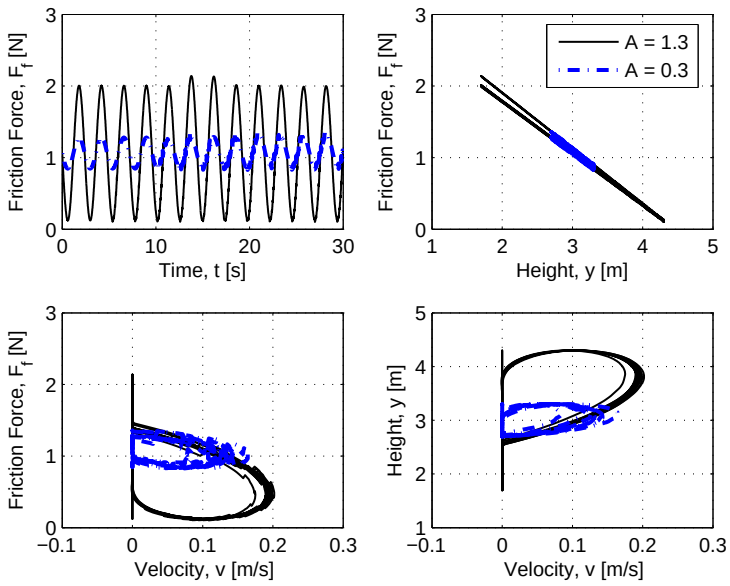

Figure 4.6: Simulations of (4.44)-(4.45) with a prescribed height trajectory $y = A\sin(\omega t)$ where $A = 0.3$ m, and $A = 1.3$ m and $\omega = 6.8$ rad/s and F_f modeled by (4.13). The parameter values used are $m = 1$ kg, $K = 2$ N/m, $w = 1$ m, $d = 2$ m, $\alpha = 15°$, $N = 100$, $k = 0.05$ N/m, and $h_0 = 4.46$ m. The dynamic Stribeck effect is more pronounced in the simulation with a larger amplitude of vertical motion.

$\boldsymbol{x} = \begin{bmatrix} x & v & y & \dot{y} \end{bmatrix}^{\mathrm{T}}$, the set Σ defined by the roots of function $g(\boldsymbol{x}) = v$, the normal to Σ defined by $\boldsymbol{n} \triangleq \nabla g(\boldsymbol{x}) = \begin{bmatrix} 0 & 1 & 0 & 0 \end{bmatrix}^{\mathrm{T}}$, and vector fields $\boldsymbol{f}_+(\boldsymbol{x})$ and $\boldsymbol{f}_-(\boldsymbol{x})$ defined as

$$\boldsymbol{f}_+(\boldsymbol{x}) \triangleq \begin{bmatrix} v \\ \frac{1}{m}(-Kx + u - F_{f+}(x,y)) \\ \dot{y} \\ -mg + F_{y+}(x,y) \end{bmatrix}, \tag{4.50}$$

$$\boldsymbol{f}_-(\boldsymbol{x}) \triangleq \begin{bmatrix} v \\ \frac{1}{m}(-Kx + u - F_{f-}(x,y)) \\ \dot{y} \\ -mg + F_{y-}(x,y) \end{bmatrix}, \tag{4.51}$$

where $F_{f+}(x,y)$ and $F_{f-}(x,y)$ are defined by (4.10) and (4.12), respectively, and $F_{y+}(x,y)$ and $F_{y-}(x,y)$ are defined by (4.46) and (4.47), respectively.

The input-output map of (4.50)-(4.51), obtained from the Switch Model (4.33)-(4.43), with parameter values $m = 1$ kg, $K = 2$ N/m, $w = 1$ m, $d = 2$ m, $\alpha = 15°$, $g = 10$ m/s^2, $N = 500$, $\Delta = 0.0035$ m, $h_0 = 1.65$ m, $k = 0.01$ N/m, $\eta = 10^{-6}$, and $u(t) = 2\sin(0.01t)$ N is shown in Figure 4.7(a). The time histories of the states and the friction force are shown in Figure 4.7(b). Since the plot of the input $u(t)$ versus position of the body x forms a loop at a low frequency of the input, the system (4.50)-(4.51) with friction force described by (4.13) is hysteretic [55]. During the motion, the energy is stored in the bristles and dissipated by the oscillation of the bristles once the mass passes over them. The energy dissipation is manifested in the force-position hysteresis loop, whose area 2.384 J is equal to the amount of dissipated energy. Note that the hysteresis map has a staircase shape typical of stick-slip motion. Furthermore the time history of the velocity shows jumps in the velocity, which means that the body goes through periods of sticking, where the velocity is zero, followed by slipping, where the velocity is nonzero.

The plots in Figure 4.8 show the height and velocity versus the friction force. In accordance with [21] the magnitude of the friction force decreases with height. Furthermore, the magnitude of the friction force drops with an increase in velocity, and the friction force-velocity curve forms a loop as shown in Figure 4.8, which indicates the presence of the dynamic Stribeck effect.

4.3 Simplified Compressed Bristle Model

In this section we introduce a simplified version of the compressed bristle model, which eliminates the need for the Switch Model. The simplified compressed bristle model (SCBM) is a single-state model [83,87,93,98] that captures the stick-slip properties and the characteristics of the friction force-height, friction force-velocity, and

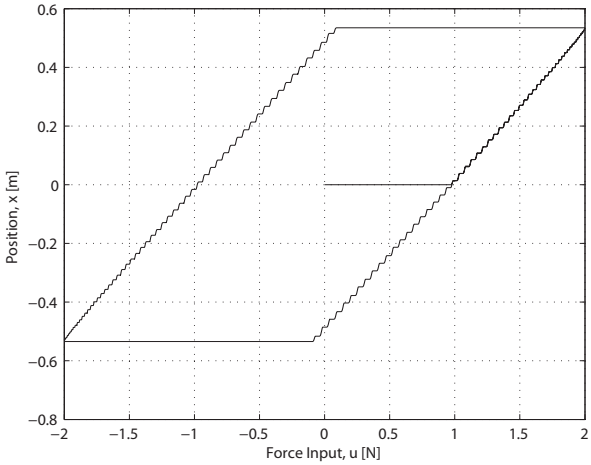

(a)

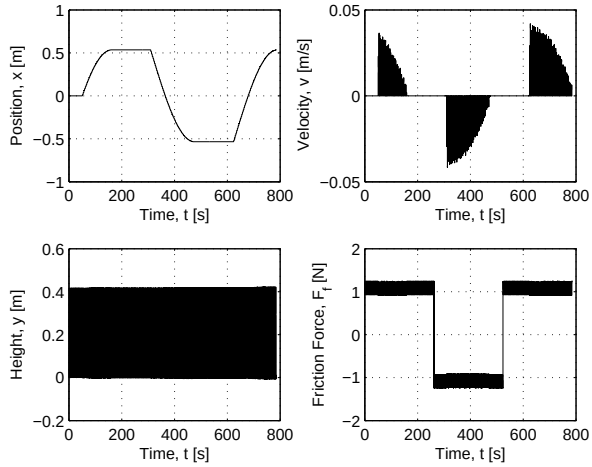

(b)

Figure 4.7: The input-output map and time histories of the position x, velocity v, height y, and friction force F_f of the mass-spring system shown in Figure 4.3 with the friction force modeled by (4.13). The input-output map is hysteretic due to the energy dissipated in order to compress the bristle springs. The energy dissipated is equal to the area of the hysteresis map.

velocity-height relationships of the compressed bristle model.

4.3.1 Single-state friction models

Single-state friction models such as the Dahl and LuGre model involve a state variable z that represents the internal friction mechanism. These models have the

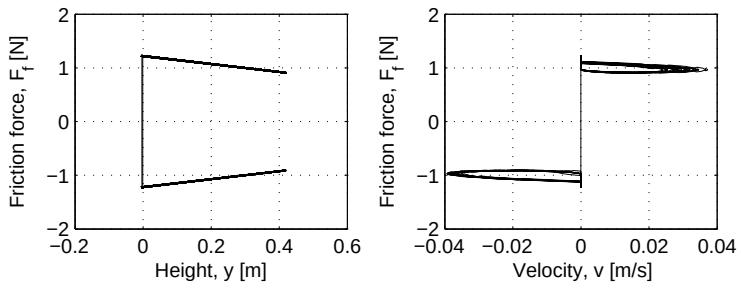

Figure 4.8: Dependence of friction force on height and velocity. The magnitude of the friction force decreases with increasing height and velocity. The drop in friction force with increased velocity is the Stribeck effect.

form

$$\dot{z} = v\left(1 - \alpha(v,z)\text{sign}(v)\frac{z}{z_{ss}(v)}\right), \tag{4.52}$$

$$F_f = \sigma_0 z + \sigma_1 \dot{z} + \sigma_2 v, \tag{4.53}$$

where σ_0, σ_1, σ_2 are positive constants, z is the internal friction state, $z_{ss}(v)$ determines the shape of the steady-state z curve, and F_f is the friction force. The function $\alpha(v,z)$ determines the presence and type of elastoplastic presliding displacement [93, 98]. For simplicity, we set $\alpha(v,z) = 1$ and rewrite (4.52)-(4.53) as

$$\dot{z} = v - \frac{|v|}{z_{ss}(v)}z, \tag{4.54}$$

$$F_f = \sigma_0 z + \sigma_1 \dot{z} + \sigma_2 v. \tag{4.55}$$

Setting $z_{ss}(v)$ to be

$$z_{ss}(v) = \frac{1}{\sigma_0}\left(F_c + (F_s - F_c)e^{-(v/v_s)^2}\right), \tag{4.56}$$

where F_c, F_s, and v_s are constants, yields the LuGre model [25, 26], which exhibits stick-slip, hysteresis, and the Stribeck effect.

In steady-state motion, $\dot{z} = 0$, and thus $z = \text{sign}(v)z_{ss}(v)$. Furthermore, if $\sigma_1 = \sigma_2 = 0$, then

$$F_f = \sigma_0 z = \text{sign}(v)\sigma_0 z_{ss}(v). \tag{4.57}$$

4.3.2 Mean friction force

The goal in formulating the SCBM is to capture the characteristics of the friction force-height, friction force-velocity, and velocity-height relationships of the compressed bristle model, while redefining the compressed bristle model equations as a continuous model. As shown in Figure 4.5, the friction force-velocity and height-velocity curves form loops. To model these loops, we fit a function to the mean values of each loop and then reformulate the compressed bristle model equations in the form of a single-state friction model.

First, we find the mean value of the friction force as a function of height y. For all $v \geq 0$, the bristle height $h_{i+}(x, y)$ is calculated from (4.2), and the ith bristle contributes to the friction force if $x_{b_i} \in \mathcal{X}_{b+}(x)$ defined by (4.7), that is,

$$x + \frac{d}{2} - d_1 \leq x_{b_i} \leq x + \frac{d}{2}. \tag{4.58}$$

Thus, over all relevant values of x_{b_i}, $h_{i+}(x, y)$ takes on the maximum and minimum values

$$h_{i+,\max}(x, y) = y - \frac{w}{2} + \frac{w}{d_2}\left(x + \frac{d}{2} - d_1 - \left(x + \frac{d}{2} - d_1\right)\right) = y - \frac{w}{2}, \tag{4.59}$$

$$h_{i-,\min}(x, y) = y - \frac{w}{2} + \frac{w}{d_2}\left(x + \frac{d}{2} - \left(x + \frac{d}{2} - d_1\right)\right) = y + \frac{w}{2}. \tag{4.60}$$

Similarly, for all $v < 0$, the bristle height $h_{i-}(x)$ is found from (4.3), and the ith

bristle contributes to the friction force if $x_{b_i} \in \mathcal{X}_{b-}(x)$ defined by (4.8), that is,

$$x - \frac{d}{2} \leq x_{b_i} \leq x - \frac{d}{2} + d_1. \tag{4.61}$$

Thus, over all relevant values of x_{b_i}, $h_{i-}(x, y)$ takes on the maximum and minimum values

$$h_{i-,\max}(x, y) = y - \frac{w}{2} + \frac{w}{d}\left(x - \frac{d}{2} + d_1 - \left(x - \frac{d}{2} + d_1\right)\right) = y - \frac{w}{2}, \tag{4.62}$$

$$h_{i-,\min}(x, y) = y - \frac{w}{2} + \frac{w}{d}\left(x - \frac{d}{2} + d_1 - \left(x - \frac{d}{2}\right)\right) = y + \frac{w}{2}. \tag{4.63}$$

Thus, for all $v \in \mathbb{R}$, the mean value of the ith bristle height $h_i(x, v, y)$ is

$$\overline{h_i}(y) = \frac{1}{2}\left(y + \frac{w}{2} + y - \frac{w}{2}\right) = y, \tag{4.64}$$

and the mean value of the friction force is

$$\overline{F_f}(x, v, y) = \begin{cases} k\cos(\alpha)\sum_{i=1}^{n_+} \overline{h_0 - h_i} = n_+ k\cos(\alpha)(\overline{h_0 - h_i}), \text{ if } v \geq 0, \\ -k\cos(\alpha)\sum_{i=1}^{n_-} \overline{h_0 - h_i} = -n_- k\cos(\alpha)(\overline{h_0 - h_i}), \text{ if } v < 0. \end{cases} \tag{4.65}$$

where $\overline{h_0 - h_i}$ denotes the mean value of $h_0 - h_i$. To find $\overline{h_0 - h_i}$, we use

$$\overline{h_0 - h_i} = \frac{\sum_{i=1}^{n}(h_0 - h_i)}{n} = h_0 - \frac{\sum_{i=1}^{n} h_i}{n} = h_0 - \overline{h_i} = h_0 - y, \tag{4.66}$$

so that

$$\overline{F_f}(y, v) = \text{sign}(v) kn\cos(\alpha)(h_0 - y) = \text{sign}(v)\tilde{k}(h_0 - y), \tag{4.67}$$

where $\tilde{k} = kn\cos(\alpha)$ and we assume that $n_+ = n_- = n$. Equation (4.67) describes the friction force as a function of height.

4.3.3 Velocity-height curve fits

In order to obtain an expression for friction force as a function of velocity we now formulate the height y as a function of velocity v. We can then use $y(v)$ in (4.67) to obtain $F_f(v)$.

Instead of a function that approximates the velocity-height loop, we find a function that approximates the mean value of y as a function of velocity. The actual and mean values of the height y shown in Figure 4.9 are obtained from simulating (4.44)-(4.45) with the Switch Model (4.33)-(4.43) and parameters $m = 1$ kg, $K = 5$ N/m, $w = 1$ m, $d = 2$ m, $\alpha = 15^\circ$, $g = 10$ m/s^2, $N = 500$, $k = 0.01$ N/m, $\Delta = 0.0035$ m, $h_0 = 1.65$ m, $\eta = 10^{-6}$, and $v_p = \pm 0.1$ m/s. Note that y is limited to the range $0 \leq y \leq h_0$ since the bristles do not stretch beyond their relaxed length h_0 or compress beyond the level of the ground.

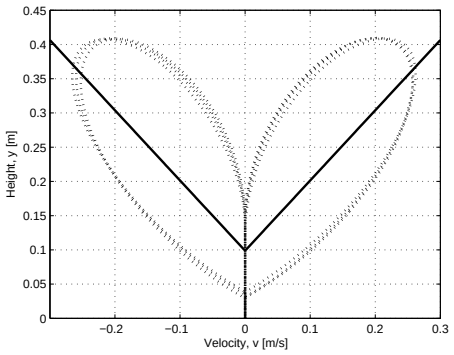

Figure 4.9: The velocity-height curve and its mean value. The mean value is shown by the solid line, and the simulation result is shown by the dashed line.

To approximate the mean value of the velocity-height curve, we choose two different functions, namely, hyperbolic secant and exponential. The hyperbolic secant expression is

$$\overline{y}(v) = y_1 - y_2 \text{sech}\left(\frac{v}{v_s}\right), \tag{4.68}$$

where y_1 and y_2 determine the maximum and minimum values of $\overline{y}$ and v_s is the

velocity at which the height increases from y_1 to y_2. If $\overline{y}(v)$ is defined by (4.68), then the approximation of the mean friction force is

$$\overline{F_f}(v) = \text{sign}(v)\tilde{k}\left(h_0 - y_1 + y_2\text{sech}\left(\frac{v}{v_s}\right)\right). \tag{4.69}$$

Figure 4.10(a) shows the approximation of the mean height $\overline{y}$ as the function of velocity defined by (4.68), while Figure 4.10(b) shows the approximation of the mean friction force $\overline{F_f}$ as the function of velocity defined by (4.69) with the parameter values $y_1 = 0.4$ m, $y_2 = 0.3$ m, $v_s = \frac{0.6}{2\pi}$ m/s, $\tilde{k} = 0.75$ N/m, and $h_0 = 1.64$ m. Figure 4.10 also shows the actual and mean values of the height y and the friction force F_f obtained from simulating (4.44)-(4.45) with parameters $m = 1$ kg, $K = 5$ N/m, $w = 1$ m, $d = 2$ m, $\alpha = 15°$, $g = 10$ m/s^2, $N = 500$, $k = 0.01$ N/m, $\Delta = 0.0035$ m, $h_0 = 1.65$ m, $\eta = 10^{-6}$, and $v_p = \pm 0.1$ m/s

Alternatively, we can approximate the mean height by the exponential function of velocity

$$\overline{y}(v) = y_1 - y_2 e^{-(v/v_s)^2}, \tag{4.70}$$

where y_1 and y_2 are the maximum and minimum values of mean height, respectively, and v_s is the velocity at which the mean height increases from y_2 to y_1. If $\overline{y}$ is defined by (4.70), then the approximation of the mean friction force is

$$\overline{F_f}(v) = \text{sign}(v)\tilde{k}\left(h_0 - y_1 + y_2 e^{-(v/v_s)^2}\right). \tag{4.71}$$

Figure 4.11(a) shows the approximation of the mean height $\overline{y}$ as the function of velocity defined by (4.70), while Figure 4.11(b) shows the approximation of the mean friction force $\overline{F_f}$ as the function of velocity defined by (4.71) with parameters $y_1 = 0.4$ m, $y_2 = 0.3$ m, $v_s = 0.1$ m/s, $\tilde{k} = 0.75$ N/m, and $h_0 = 1.7$ m. Figure 4.10 also shows

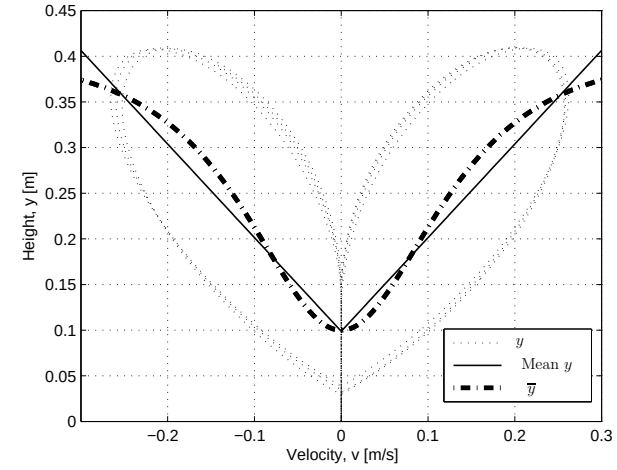

(a)

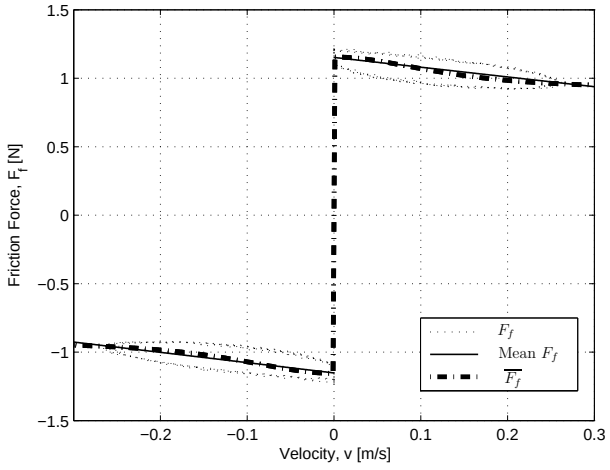

(b)

Figure 4.10: Approximation of the mean height (4.68) and mean friction force (4.69) of the SBM friction model (dash-dot) obtained by approximating the mean height by hyperbolic secant function of velocity. (a) shows the approximation of the mean height $\overline{y}$ as the function of velocity defined by (4.68), (b) shows the approximation of the mean friction force $\overline{F_f}$ as the function of velocity defined by (4.69). The actual and mean values of the height y and friction force F_f are also shown by the dotted and solid lines, respectively.

the actual and mean values of the height y and the friction force F_f obtained from simulating (4.44)-(4.45) with parameters $m = 1$ kg, $K = 5$ N/m, $w = 1$ m, $d = 2$ m, $\alpha = 15°$, $g = 10$ m/s^2, $N = 500$, $k = 0.01$ N/m, $\Delta = 0.0035$ m, $h_0 = 1.65$ m,

$\eta = 10^{-6}$, and $v_p = \pm 0.1$ m/s

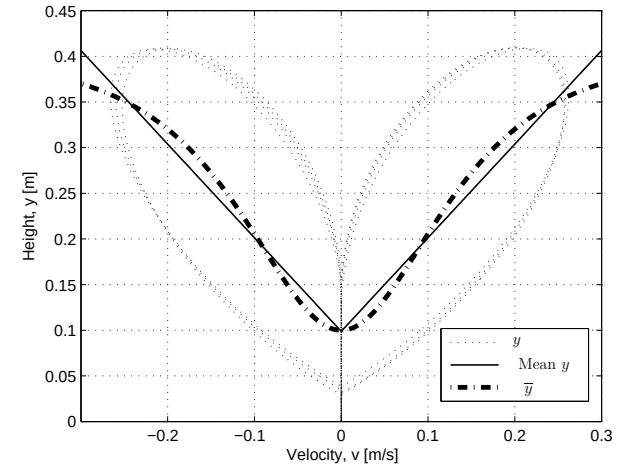

(a)

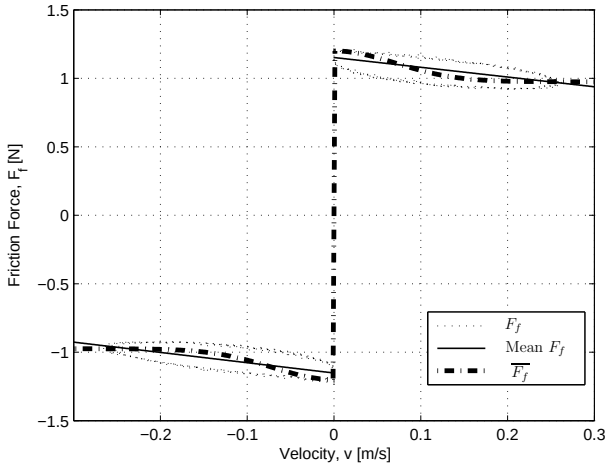

(b)

Figure 4.11: Approximation of the mean height (4.70) and mean friction force (4.71) of the SBM friction model (dash-dot) obtained by approximating the mean height by an exponential function of velocity with parameters $y_1 = 1$ m, $y_2 = 0.5$ m, $v_s = 0.1$ m/s, $\tilde{k} = 1$ N/m, and $h_0 = 2$ m. (a) shows the approximation of the mean height $\overline{y}$ as the function of velocity defined by (4.70), (b) shows the approximation of the mean friction force $\overline{F_f}$ as the function of velocity defined by (4.71). The actual and mean values of the height y and friction force F_f are also shown by the dotted and solid lines, respectively.

Combining (4.57) and (4.69) yields

$$z_{ss}(v) = \frac{\tilde{k}}{\sigma_0}\left(h_0 - y_1 + y_2 \text{sech}\left(\frac{v}{v_s}\right)\right), \tag{4.72}$$

and the single-state friction model

$$\dot{z} = v - \sigma_0 \frac{|v|}{\tilde{k}\left(h_0 - h_1 + h_2 \text{sech}\left(\frac{v}{v_s}\right)\right)} z, \tag{4.73}$$

$$F_f = \sigma_0 z. \tag{4.74}$$

Furthermore, combining (4.57) and (4.71) gives the alternative expression

$$z_{ss} = \frac{\tilde{k}}{\sigma_0}\left(h_0 - y_1 + y_2 e^{-(v/v_s)^2}\right), \tag{4.75}$$

and the alternative single-state friction model

$$\dot{z} = v - \sigma_0 \frac{|v|}{\tilde{k}\left(h_0 - y_1 + y_2 e^{-(v/v_s)^2}\right)} z, \tag{4.76}$$

$$F_f = \sigma_0 z. \tag{4.77}$$

The equations (4.76)-(4.77) are identical to the LuGre equations (4.54)-(4.56) with $\sigma_1 = \sigma_2 = 0$, $\tilde{k}(h_0 - y_1) = F_c$, and $\tilde{k}y_2 = F_s - F_c$. In order to further demonstrate the similarity of the LuGre model and the simplified compressed bristle model, we simulate the systems of equations (4.18)-(4.20) and (4.26)-(4.27) with the friction force (4.76)-(4.77). The output of the system (4.18)-(4.20) with the friction force (4.76)-(4.77) and input velocity $v_p = 0.1$ m/s is shown in Figure 4.12(a). The parameter values are $m = 1$ kg, $K = 1$ N/m, $y_1 = 1$ m, $y_2 = 0.5$ m, $v_s = 0.1$ m/s, $\tilde{k} = 1$ N/m, $\sigma = 10^5$, and $h_0 = 2$ m. The results of simulating (4.26)-(4.27) with the friction force (4.76)-(4.77) and input defined by $u(t) = 5\sin(0.01t)$ N, are shown in Figure 4.12(b).

The stick-slip behavior is visible in both simulations, and the system is hysteretic as shown by the hysteretic input-output map.

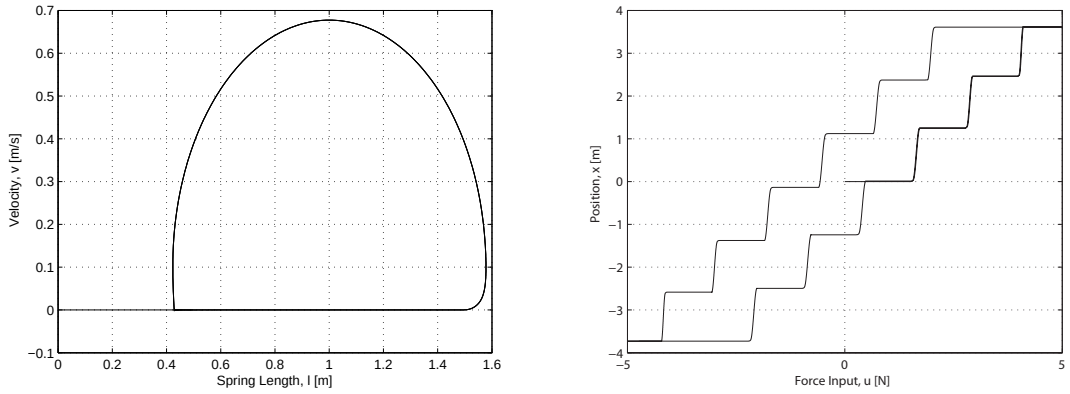

(a) (b)

Figure 4.12: The stick-slip limit cycle of (4.18)-(4.20) and the hysteresis map of (4.26)-(4.27) with friction force modeled by (4.76)-(4.77). The stick-slip limit cycle in the l-v plane is shown in (a). (b) shows the hysteresis map with stair-step shape typical of stick-slip motion.

4.4 Conclusions

In this chapter we developed the compressed bristle model, an asperity-based friction model in which the friction force arises through the frictionless and lossless interaction of a body with an endless row of bristles that represent the microscopic roughness of the contacting surfaces. The bristles consist of a frictionless roller attached to the ground through a spring. The body is allowed to move horizontally and vertically over the bristles, which are compressed and thus apply a reaction force at the point of contact. The friction force is the sum of all horizontal components of the contact forces between all of the bristles and the body. As the body passes over the compressed bristles, they are suddenly released, and the energy stored in each spring is dissipated by viscous dashpot regardless of how slowly the body moves. Thus, energy is dissipated in the limit of DC operation and the system is hysteretic.

In the vertical direction, the body and the bristles form an undamped oscillator. The body oscillates vertically regardless of whether it is moving horizontally or not. During the vertical oscillations, as the body rises, the friction force decreases, and the body speeds up. This mechanism gives rise to the dynamic Stribeck effect, which refers to the fact that the friction force-velocity curve forms a loop.

Furthermore, we showed that the compressed bristle model exhibits stick-slip friction and that the compressed bristle model equations can be simplified to give a single-state friction model. The simplified compressed bristle model (SCBM) retains the stick-slip and hysteresis properties of the original model. The internal friction state of the SCBM can be interpreted as the average deflection of the bristles from their relaxed length. The simplified compressed bristle model is equivalent to the LuGre model.

CHAPTER V

Why Are Some Hysteresis Loops Shaped Like a Butterfly?

The contribution of this chapter is a framework for relating butterfly-shaped hysteresis maps to simple (single-looped) hysteresis maps, which are typically easier to model and more amenable to control design. In particular, a unimodal mapping is used to transform simple loops to butterfly loops. For the practically important class of piecewise monotone hysteresis maps, we provide conditions for producing butterfly-shaped maps and examine the properties of the resulting butterflies. Conversely, we present conditions under which butterfly-shaped maps can be converted to simple piecewise monotone hysteresis maps to facilitate hysteresis compensation and control design. Examples of a preloaded two-bar linkage mechanism and a magnetostrictive actuator illustrate the theory and its utility for understanding, modeling, and controlling systems with butterfly-shaped hysteresis.

5.1 Introduction

Hysteresis is a property of a nonlinear system whose periodic steady-state response retains a nontrivial input-output map (called the hysteresis map) as the frequency of periodic excitation approaches zero. The underlying mechanism that gives rise

to hysteresis is multistability, which refers to the existence of multiple attracting equilibria. Under slow excitation, the state of the system is attracted to different equilibria depending on the direction of the input [39].

Hysteretic systems arise in a vast range of applications, such as ferromagnetics, smart materials, biological systems, and aerodynamics [63, 84, 107–110]. In some applications, the dynamic response is independent of the frequency of excitation, and thus the dynamic response map is identical to the hysteresis map. Such systems have rate-independent hysteresis. In most applications, however, the dynamic response depends on the frequency of excitation, and thus the dynamic response is distinct from the hysteresis map. Such systems have rate-dependent hysteresis. For details, see [55]. In this chapter, we ignore the transient response of the system and focus only on the hysteresis map, that is, on the periodic steady-state response at asymptotically low frequency.

This chapter focuses on butterfly-shaped hysteresis maps, which arise in many applications, such as optics and smart materials [40, 41, 60–62, 111–114]. A hysteresis map is a butterfly when it consists of two loops of opposite orientation. In some applications, the shape of the hysteresis map is reminiscent of butterfly wings, which explains the terminology.

Although butterfly hysteresis is widely observed in the literature, we are not aware of any explanations of the significance or origin of the characteristic shape of these maps. In this chapter we show that certain simple (that is, single-loop) hysteresis maps can be transformed into a multi-loop hysteresis map with alternating loop orientation by means of a unimodal mapping of the output variable. When more than two loops appear, we call the hysteresis map a multibutterfly. In particular, we provide an example in which a unimodal map transforms a simple closed curve into a triple-loop butterfly.

It is not possible to transform any simple hysteresis map into a butterfly. In

particular, we show that only a special type of symmetric simple curves can form butterflies, but that symmetric simple closed curves can form multibutterflies. We determine conditions on the unimodal functions that can transform piecewise monotonic hysteresis loops into butterflies. We show that if a butterfly satisfies specific conditions, then there exists a unimodal map that transforms a simple closed curve into this butterfly.

To facilitate control design, we can minimize the effects of butterfly hysteresis by transforming the butterfly map into a simple hysteresis map. The simple map can be fitted with a Preisach or a Prandtl-Ishlinskii model [64, 66, 70–72, 115]. Once the model of the hysteresis is available we can construct the inverse of the known hysteresis to cancel its effects.

To illustrate these ideas, we consider the preloaded two-bar linkage, which is a classical example of elastic instability [116]. The hysteretic nature of this mechanism is studied in [23], where the hysteresis map is shown to be a simple closed curve in terms of the force input and linkage joint displacement. In this chapter, we consider an alternative output variable, namely, the displacement of the spring-loaded mass. In this case the resulting hysteresis map is a butterfly. This dual-loop hysteresis map with opposite orientation arises from the unimodal mapping between the linkage joint displacement and the displacement of the spring-loaded mass.

In a second example, we begin with butterfly hysteresis between the applied current and change in length of the specimen observed in a magnetostrictive actuator and presented in [117]. We use a quadratic law to relate the change of length of the specimen to the magnetization along the rod direction, as well as to transform the butterfly map into a simple hysteresis map. We fit a Preisach-Ishlinskii model to the simple map, which facilitates the design of an inverse compensator for canceling the hysteresis effect.

The contents of the chapter are as follows. In Section 5.2 we show that asymmetric

oriented simple closed curves can be transformed into a butterfly or a multibutterfly through a unimodal map. In Section 5.3 we state conditions under which it is possible to transform symmetric or piecewise monotonic simple closed curves into butterflies. In Section 5.4 we consider the preloaded two-bar linkage mechanism studied in [23] and demonstrate that an alternative output variable corresponds to a mapping that transforms the simple hysteresis map into a butterfly. In Section 5.5, we revisit an example of butterfly hysteresis in magnetostrictive actuators given in [117]. We find the inverse of the unimodal map that converts the butterfly map into a simple hysteresis map, and we approximate the simple hysteresis map with a generalized Prandtl-Ishlinskii model. A preliminary version of some of the results of this chapter is given in [118].

5.2 Transformation From a Simple Closed Curve to a Multi-Loop Curve

In this section we illustrate the transformation from a simple closed curve to a butterfly with several examples. Recall that every simple closed curve divides the plane into three sets, namely, the interior region, the exterior region, and the curve itself [119].

Throughout this chapter, let $\mathcal{C}$ be an oriented simple closed curve and let $[x_0, x_1] \times [y_0, y_1]$ be the smallest rectangle with sides parallel to the x- and y-axes containing $\mathcal{C}$. We assume throughout this chapter that, for each $x \in (x_0, x_1)$, there exists a unique pair of points $(x, y_{\min}(x))$, $(x, y_{\max}(x)) \in \mathcal{C}$ such that $y_{\min}(x) < y_{\max}(x)$. The following definitions are needed.

Definition 5.2.1. A continuous map $f : [y_0, y_1] \to \mathbb{R}$ is $\wedge$-*unimodal* if there exists $y_c \in (y_0, y_1)$ such that f is increasing on $[y_0, y_c)$ and decreasing on $(y_c, y_1]$. f is $\vee$-*unimodal* if there exists $y_c \in (y_0, y_1)$ such that f is decreasing on $[y_0, y_c)$ and

increasing on $(y_c, y_1]$. f is *unimodal* if it is either $\vee$-unimodal or $\wedge$-unimodal.

Definition 5.2.2. A *butterfly* is the union of two oriented simple closed curves with disjoint interiors, a single point of intersection, and opposite orientation, such that the curves are contained in the rectangle $[x_0, x_1]\times[q_0, q_1]$ and for each $x \in (x_0, x_1)$, the intersection of the curves and the vertical line through x consists of at most two points. A *multibutterfly* contained in the rectangle $[x_0, x_1] \times [q_0, q_1]$ is the union of three or more oriented simple closed curves with disjoint interiors and such that each curve has a point of intersection with at least one and at most two other curves. Furthermore, each pair of intersecting curves have opposite orientation and for each $x \in (x_0, x_1)$, the intersection of the curves and the vertical line through x consist of at most two points.

For $f : [y_0, y_1] \to \mathbb{R}$, define $f(\mathcal{C}) \triangleq \{(x, f(y)) : (x, y) \in \mathcal{C}\}$.

The following result is immediate.

Fact 5.2.1. Let $f : [y_0, y_1] \to \mathbb{R}$ be unimodal. Then $\mathcal{C}' = f(\mathcal{C})$ is a butterfly if and only if there exist disjoint open intervals $\mathcal{I}_1$ and $\mathcal{I}_2$ such that $[x_0, x_1] = \mathrm{cl}(\mathcal{I}_1) \cup \mathrm{cl}(\mathcal{I}_2)$, and such that, for all $x \in \mathcal{I}_1$ and all $x' \in \mathcal{I}_2$,

$$[f(y_{\min}(x)) - f(y_{\max}(x))][f(y_{\min}(x')) - f(y_{\max}(x'))] < 0. \tag{5.1}$$

We use the notation cl to denote the closure of a set. Note that $\mathrm{cl}(\mathcal{I}_1) \cap \mathrm{cl}(\mathcal{I}_2)$ is a single point.

Example 5.2.1. Let $\mathcal{C}$ be the circle centered at the origin as shown in Figure 5.1(a), and note that $\mathcal{C}$ is a doubly (that is, up-down and left-right) symmetric simple closed curve. The set of points corresponding to $y_{\max}(x)$ is shown as the dashed curve, while the set of points corresponding to $y_{\min}(x)$ is shown as the solid curve. Figure 5.1(b) shows the $\wedge$-unimodal mapping $f(y) = 1 - |y|$ applied to $\mathcal{C}$. Note that f is

continuous and increasing to the left of $y_c = 0$ and decreasing to the right of $y_c = 0$. The curve $\mathcal{C}' = f(\mathcal{C})$ is shown in Figure 5.1(c). However, $\mathcal{C}'$ is not a butterfly because, for all values of $x \in [-1, 1]$, $f(y_{\min}(x)) = f(y_{\max}(x))$ and, thus, the left hand side of (5.1) is zero. In fact, $\mathcal{C}'$ is not a closed curve but rather collapses into the degenerate curve shown in Figure 5.1(c). □

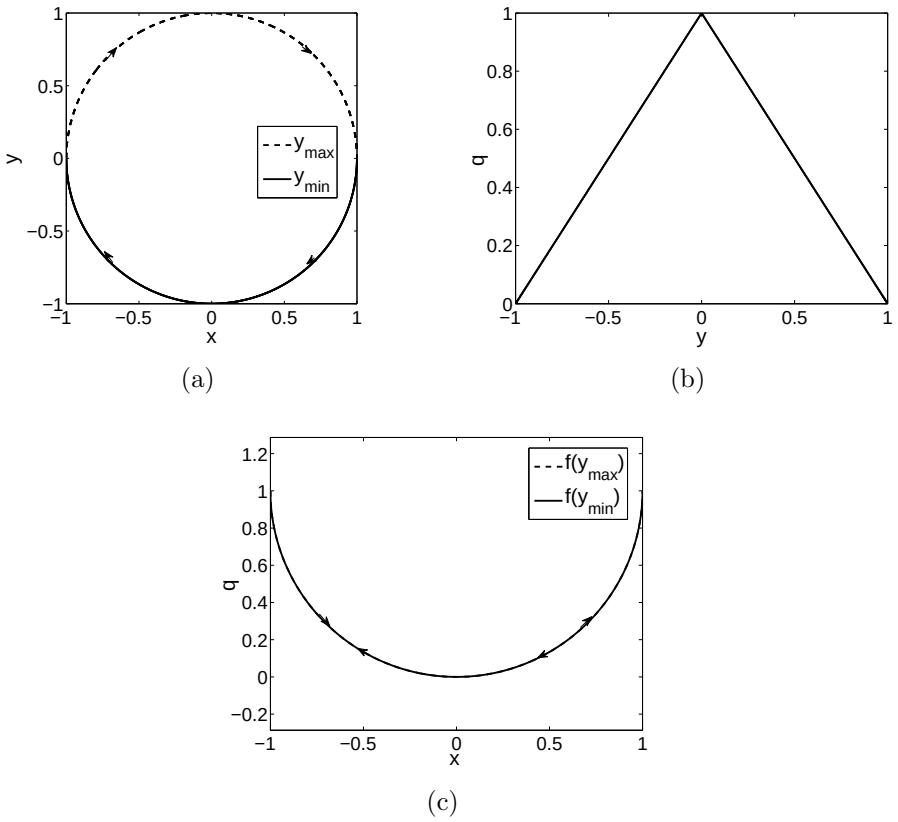

Figure 5.1: Transformation that gives a degenerate curve. The original simple closed curve $\mathcal{C}$ in (a) is transformed by the mapping $f(y) = 1 - |y|$ shown in (b). The resulting curve shown in (c) is degenerate.

Example 5.2.2. Consider $\mathcal{C}$ shown in Figure 5.2(a). The set of points corresponding to $y_{\max}(x)$ is shown as the dashed curve, while the set of points corresponding to $y_{\min}(x)$ is shown as the solid curve. Figure 5.2(b) shows the same $\wedge$-unimodal mapping f used in Example 5.2.1. The curve $\mathcal{C}' = f(\mathcal{C})$ is shown in Figure 5.2(c). However, the curve $\mathcal{C}'$ is not a butterfly because, for all x in $\mathrm{cl}(\mathcal{I}_1) \cup \mathrm{cl}(\mathcal{I}_2)$, where

$\mathcal{I}_1 = (-1, 0)$ and $\mathcal{I}_2 = (0, 1)$, the left hand side of (5.1) is positive. Note that, although $\mathcal{C}'$ has two loops, both loops have the same orientation, and thus $\mathcal{C}'$ is not a butterfly. $\square$

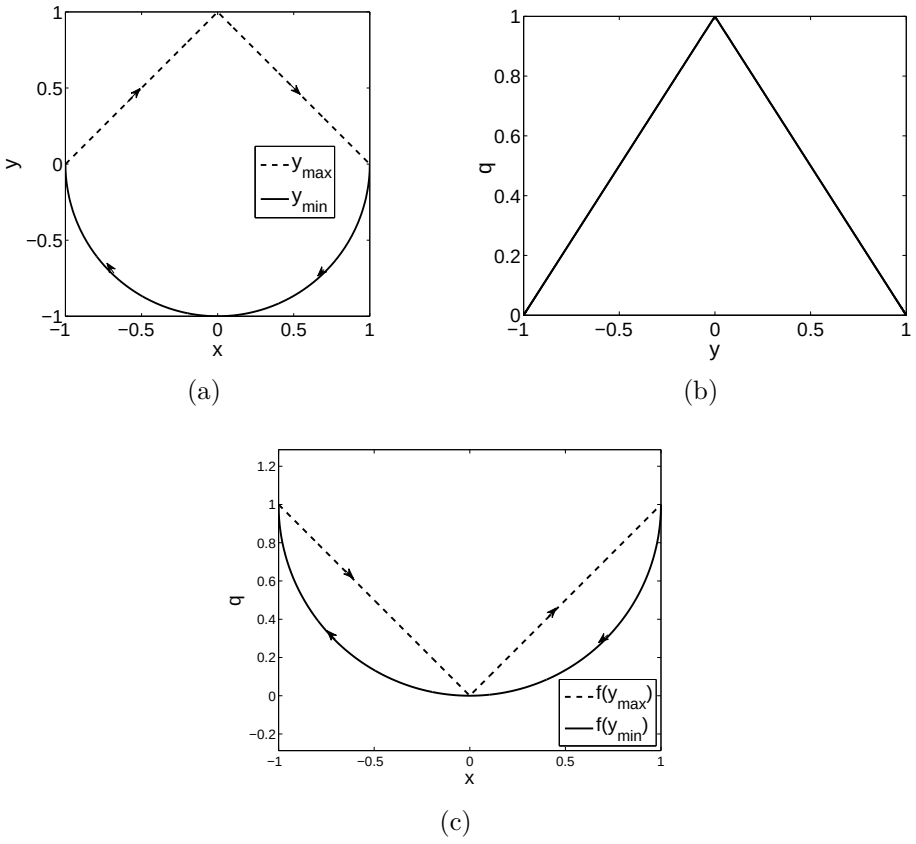

Figure 5.2: Transformation that gives a two-loop curve that is not a butterfly. The original simple closed curve $\mathcal{C}$ shown in (a) is transformed by the mapping $f(y) = 1 - |y|$ shown in (b). The resulting curve shown in (c) has two loops but is not a butterfly since both curves have the same orientation.

Example 5.2.3. Consider $\mathcal{C}$ shown in Figure 5.3(a). The set of points corresponding to $y_{\max}(x)$ is shown as the dashed curve, while the set of points corresponding to $y_{\min}(x)$ is shown as the solid curve. We use the same $\wedge$-unimodal mapping $f(y) = 1 - |y|$ as in Example 5.2.2 (see Figure 5.3(b)). The curve $\mathcal{C}' = f(\mathcal{C})$ is shown in Figure 5.3(c). In this case, for all values of x in the interval $\mathcal{I}_1 = (-1, 0)$, $f(y_{\max}(x)) > f(y_{\min}(x))$, whereas, for all values of x' in the interval $\mathcal{I}_2 = (0, 1)$,

$f(y_{\max}(x')) < f(y_{\min}(x'))$ and inequality (5.1) is satisfied. Therefore, Fact 5.2.1 implies that $\mathcal{C}'$ is a butterfly as shown in Figure 5.3(c). □

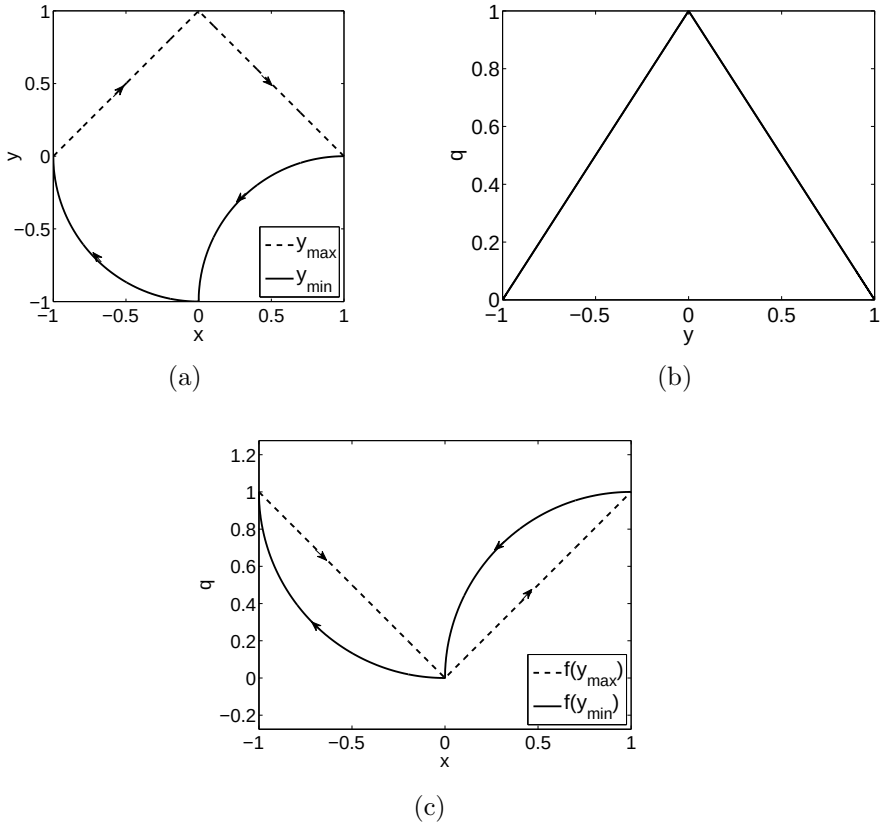

Figure 5.3: Transformation of a simple closed curve into a butterfly. The simple closed curve $\mathcal{C}$ shown in (a) is transformed by the $\wedge$-unimodal mapping $f(y) = 1 - |y|$ shown in (b). The resulting curve is the butterfly $\mathcal{C}'$ shown in (c).

Fact 5.2.2. Let $f : [y_0, y_1] \to \mathbb{R}$ be unimodal. Then $\mathcal{C}' = f(\mathcal{C})$ is a multibutterfly if and only if there exist disjoint open intervals $\mathcal{I}_1, \ldots, \mathcal{I}_n$ such that $[x_0, x_1] = \mathrm{cl}(\mathcal{I}_1) \cup \cdots \cup \mathrm{cl}(\mathcal{I}_n)$, and such that, for each pair of adjacent intervals $\mathcal{I}_i$, $\mathcal{I}_j$, it follows that, for all $x \in \mathcal{I}_i$ and all $x' \in \mathcal{I}_j$

$$[f(y_{\min}(x)) - f(y_{\max}(x))][f(y_{\min}(x')) - f(y_{\max}(x'))] < 0. \tag{5.2}$$

To illustrate this concept, the following example shows the transformation of a

non-symmetric simple closed curve into a multibutterfly.

Example 5.2.4. Consider $\mathcal{C}$ as in Example 5.2.3 (see Figure 5.4(a)). The set of points corresponding to $y_{\max}(x)$ is shown by the dashed curve, while the set of points corresponding to $y_{\min}(x)$ is shown by the solid curve. Figure 5.4(b) shows the $\wedge$-unimodal mapping f applied to $\mathcal{C}$. The function f is continuous and increasing to the left of $y_c = -0.5$ and decreasing to the right of $y_c = -0.5$. The curve $\mathcal{C}' = f(\mathcal{C})$ is shown in Figure 5.4(c). Inequality (5.2) is satisfied for all values of x in the intervals $\mathcal{I}_1 = (-1, -0.675)$, $\mathcal{I}_2 = (-0.675, 0)$, and $\mathcal{I}_3 = (0, 1)$, and thus $\mathcal{C}'$ is a three-loop multibutterfly.

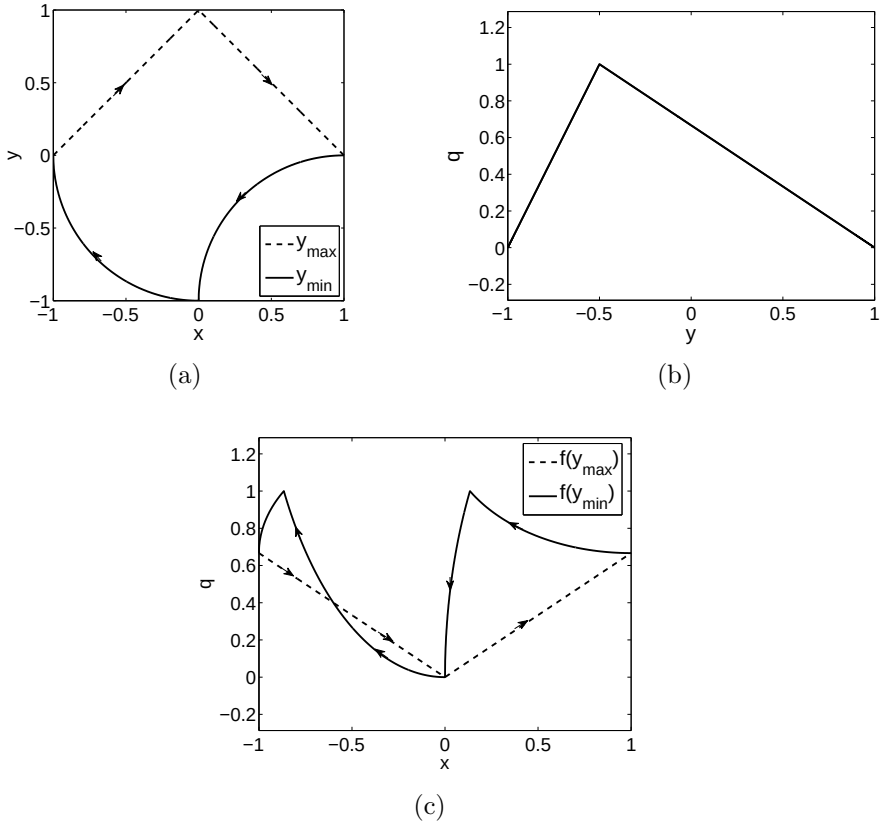

Figure 5.4: Transformation of a simple closed curve into a multibutterfly. The counterclockwise-oriented simple closed curve $\mathcal{C}$ shown in (a) is transformed by the $\wedge$-unimodal map f shown in (b). The resulting curve is the multibutterfly shown in (c).

□

5.3 Analysis of Unimodal Transformations

In this section we state conditions under which it is possible to transform a simple closed curve into a butterfly, and we highlight the types of butterfly loops that can be obtained by a unimodal transformation of a simple closed curve. It turns out that certain symmetric simple closed curves cannot be transformed into butterflies. However, we show that every symmetric simple closed curve can be transformed into a multibutterfly.

Proposition 5.3.1. If $\mathcal{C}$ is left-right symmetric, then there does not exist a unimodal map that transforms $\mathcal{C}$ into a butterfly.

Proof. Let $\mathcal{J}_1 = (x_0, \bar{x}_0)$ be an interval, where $\bar{x}_0 < \frac{x_0+x_1}{2}$. Due to the symmetry of $\mathcal{C}$, for each $x \in \mathcal{J}_1$ there exists $x' \in \mathcal{J}_2 = (\bar{x}_1, x_1)$ such that $\bar{x}_1 > \frac{x_0+x_1}{2}$, $y_{\min}(x) = y_{\min}(x')$, and $y_{\max}(x) = y_{\max}(x')$. Furthermore, $f(y_{\min}(x)) = f(y_{\min}(x'))$ and $f(y_{\max}(x)) = f(y_{\max}(x'))$, that is,

$$[f(y_{\min}(x)) - f(y_{\max}(x))][f(y_{\min}(x')) - f(y_{\max}(x'))] > 0 \tag{5.3}$$

for all $x \in \mathcal{J}_1$ and $x' \in \mathcal{J}_2$. Let $\mathcal{I}_1$ and $\mathcal{I}_2$ be disjoint open intervals such that $[x_0, x_1] = \mathrm{cl}(\mathcal{I}_1) \cup \mathrm{cl}(\mathcal{I}_2)$. $\mathcal{I}_1$ contains at least a portion of $\mathcal{J}_1$, and $\mathcal{I}_2$ contains at least a portion of $\mathcal{J}_2$. Since (5.1) is not satisfied on $\mathcal{J}_1$ and $\mathcal{J}_2$, (5.1) cannot be satisfied for all $x \in \mathcal{I}_1$ and all $x' \in \mathcal{I}_2$, and, thus, $\mathcal{C}$ cannot be transformed into a butterfly. □

Proposition 5.3.2. Suppose that $\mathcal{C}$ is up-down symmetric and assume that there exist unique $y(x_0)$ and $y(x_1)$ such that $(x_0, y(x_0)) \in \mathcal{C}$ and $(x_1, y(x_1)) \in \mathcal{C}$. Then there does not exist a unimodal map that transforms $\mathcal{C}$ into a butterfly.

Proof. Let $\mathcal{J}_1 = (x_0, \bar{x}_0)$ be an interval such that $\bar{x}_0 \in (x_0, x_1)$, $y_{\min}(\bar{x}_0) > y_0$, and $y_{\max}(\bar{x}_0) < y_1$. Due to the up-down symmetry of $\mathcal{C}$, for each $x \in \mathcal{J}_1$ there exists $x' \in \mathcal{J}_2 = (\bar{x}_1, x_1)$ such that $y_{\min}(x) = y_{\min}(x')$ and $y_{\max}(x) = y_{\max}(x')$ and $\bar{x}_1 \in (\bar{x}_0, x_1)$. Following the same line of reasoning as in the proof of Proposition 5.3.1, we conclude that there do not exist two open disjoint intervals for which (5.1) is satisfied. Thus it is not possible to transform $\mathcal{C}$ into a butterfly. □

The following example provides an up-down symmetric simple closed curve that does not satisfy the conditions of Proposition 5.3.2, but can be transformed into a butterfly.

Example 5.3.1. Consider the up-down symmetric simple closed curve $\mathcal{C}$ shown in Figure 5.5(a). The set of points corresponding to $y_{\max}(x)$ is shown by the dashed curve, while the set of points corresponding to $y_{\min}(x)$ is shown by the solid curve. Figure 5.5(b) shows the $\wedge$-unimodal mapping f applied to $\mathcal{C}$. The function f is continuous, increasing to the left of $y_c = 0.25$, and decreasing to the right of $y_c = 0.25$. The curve $\mathcal{C}' = f(\mathcal{C})$ is shown in Figure 5.5(c). $\mathcal{C}'$ is the union of two simple closed curves of opposite orientation and thus is a butterfly. □

The following example shows that a symmetric simple closed curve can be transformed into a multibutterfly.

Example 5.3.2. Reconsider $\mathcal{C}$ as in Example 5.2.1 shown in Figure 5.6(a). The set of points corresponding to $y_{\max}(x)$ is shown by the dashed curve, while the set of points corresponding to $y_{\min}(x)$ is shown by the solid curve. The $\wedge$-unimodal mapping $f(y) = y + 1.5$ for $y \leq 0.5$ and $f(y) = -4y + 4$ for $y > 0.5$ is shown in Figure 5.6(b). The curve $\mathcal{C}' = f(\mathcal{C})$ is shown in Figure 5.6(c). The set $[x_0, x_1] = [-1, 1]$ can be divided into the subintervals $\mathcal{I}_1 = (-1, -0.553)$, $\mathcal{I}_2 = (-0.553, 0.553)$, and $\mathcal{I}_3 = (0.553, 1)$, such that, for all $x \in \mathcal{I}_1$ and all $x' \in \mathcal{I}_2$, inequality (5.2) holds, whereas, for all $x \in \mathcal{I}_2$ and all $x' \in \mathcal{I}_3$, inequality (5.2) holds. Thus $\mathcal{C}'$ is a multibutterfly. □

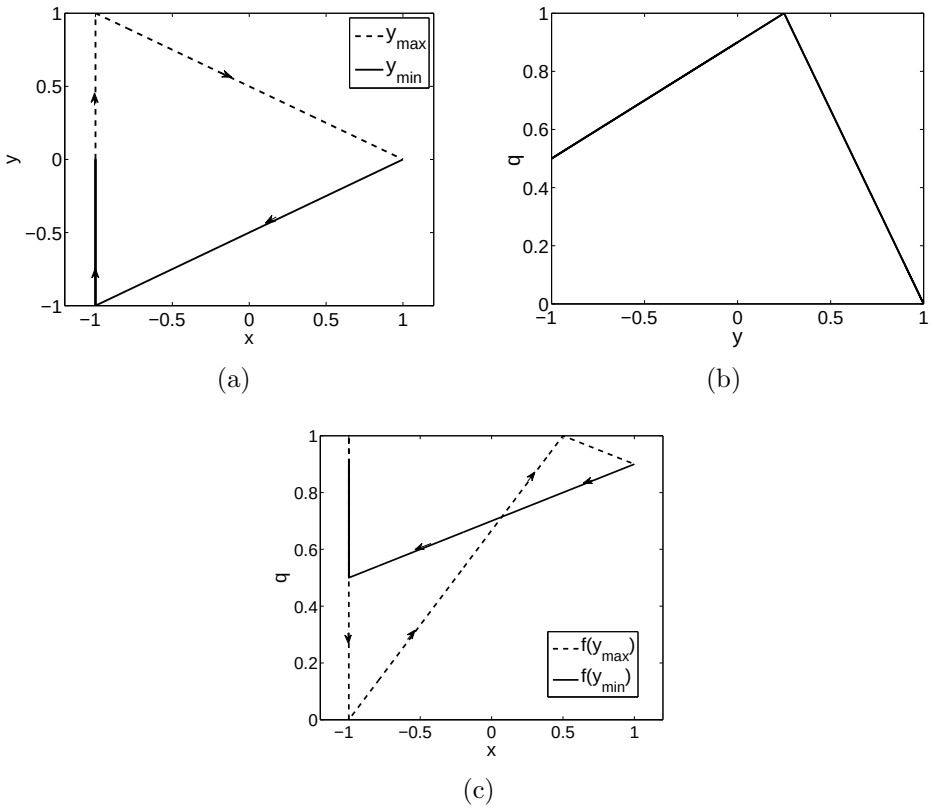

Figure 5.5: Transformation of an up-down symmetric closed curve into a butterfly. The symmetric simple closed curve $\mathcal{C}$ shown in (a) is transformed by the $\wedge$-unimodal map f shown in (b). The resulting curve is the butterfly shown in (c). Note that $\mathcal{C}$ does not satisfy the conditions of Proposition 5.3.2 since $y_{\min}(x_0)$ and $y_{\max}(x_0)$ are not unique.

The following discussion pertains to a special case of simple closed curves that are piecewise monotonic. This type of hysteresis map is common in smart materials.

Definition 5.3.1. Let $\mathcal{C}$ be an oriented simple closed curve such that, for each $x = x_0$, there exists a unique point $(x_0, y) \in \mathcal{C}$ and, for each $x = x_1$, there exists a unique point $(x_1, y) \in \mathcal{C}$. $\mathcal{C}$ is *piecewise monotonically decreasing* if $y_{\min}(x)$ and $y_{\max}(x)$ are decreasing functions of x. $\mathcal{C}$ is *piecewise monotonically increasing* if $y_{\min}(x)$ and $y_{\max}(x)$ are increasing functions of x. An oriented simple closed curve is *piecewise monotonic* if it is either piecewise monotonically decreasing or piecewise monotonically increasing.

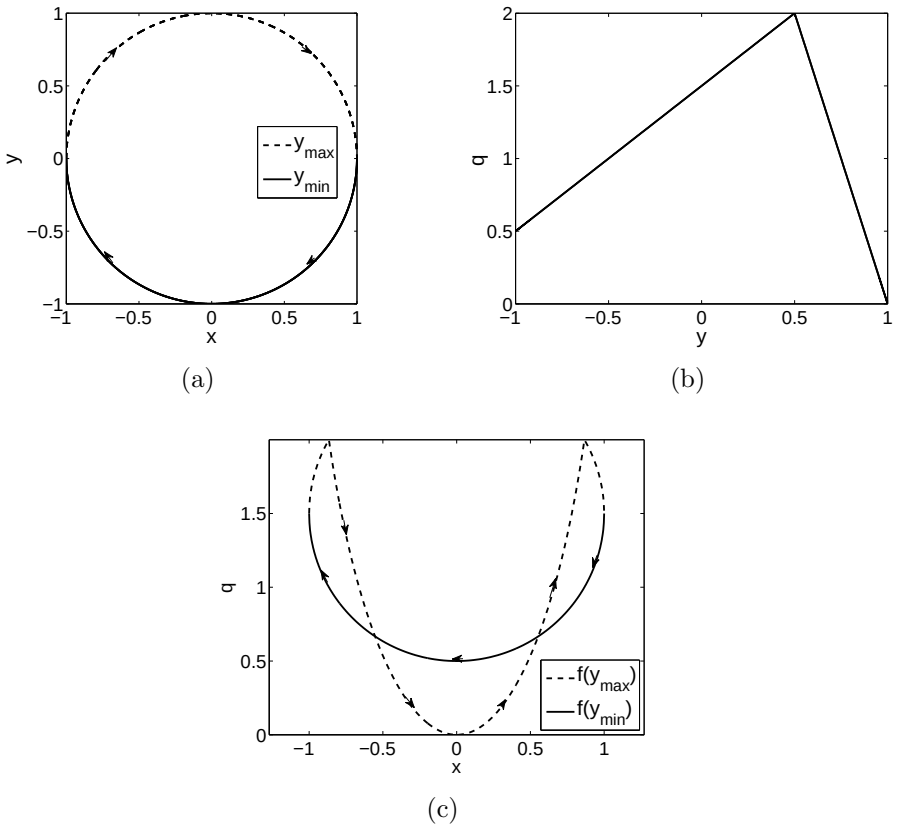

Figure 5.6: Transformation of a symmetric simple closed curve $\mathcal{C}$ into a multibutterfly. The simple closed curve $\mathcal{C}$ in (a), which is up-down and left-right symmetric, is transformed by the $\wedge$-unimodal mapping $f(y)$ shown in (b). The resulting curve shown in (c) is a multibutterfly.

The following lemma is necessary for further discussion.

Lemma 5.3.1. Let $\mathcal{S}$ be a closed polygonal region in a plane with vertices A, B, C, D, labeled consecutively. Let $\mathcal{C}_1$ be a continuous curve that connects A to C and satisfies $\mathcal{C}_1 \setminus \{\mathrm{A}, \mathrm{C}\} \subset \mathrm{int}(\mathcal{S})$. Let $\mathcal{C}_2$ be a continuous curve that connects B to D and satisfies $\mathcal{C}_2 \setminus \{\mathrm{B}, \mathrm{D}\} \subset \mathrm{int}(\mathcal{S})$. Then $\mathcal{C}_1 \cap \mathcal{C}_2 \neq \emptyset$. If, in addition, there exist coordinate axes with respect to which $\mathcal{C}_1$ is monotonically increasing (resp. decreasing) function and $\mathcal{C}_2$ is monotonically decreasing (resp. increasing) function, then $\mathcal{C}_1 \cap \mathcal{C}_2$ consists of a single point.

Proof. Because $\mathcal{C}_1$ is a continuous curve connecting A to C it divides the

rectangle $\mathcal{S}$ into two open disjoint regions R_1 and R_2, where B $\in R_1$ and D $\in R_2$. Since the curve $\mathcal{C}_2$ connects points B and D it must cross from region R_1 to region R_2. From the Jordan curve lemma $\mathcal{C}_2$ must cross the boundary between these regions, that is, the curve $\mathcal{C}_1$. Furthermore, if both of the curves are monotonic functions with respect to some axis, $\mathcal{C}_1$ increases (resp. decreases) from A to C and $\mathcal{C}_2$ decreases (resp. increases) from B to D, and thus, the curves $\mathcal{C}_1$ and $\mathcal{C}_2$ cross exactly once. □

Theorem 5.3.1. Let $\mathcal{C}$ be a piecewise monotonic simple closed curve. Furthermore, let f be a $\vee$-unimodal function with its minimum point $q_c(y_c)$ such that $y_c \in (y_0, y_1)$ or a $\wedge$-unimodal function with its maximum point $q_c(y_c)$, such that $y_c \in (y_0, y_1)$. Then $\mathcal{C}' = f(\mathcal{C})$ is a butterfly.

Proof. We assume that the map f is $\vee$-unimodal and that $\mathcal{C}$ is monotonically increasing; the remaining three cases are analogous. Let $\mathcal{J}_1 = (x_0, x_{c1})$, where $x_{c1} \in (x_0, x_1)$ and $y_{\max}(x_{c1}) = y_c$, and let $\mathcal{J}_2 = (x_{c2}, x_1)$, where $x_{c2} \in (x_0, x_1)$ and $y_{\min}(x_{c2}) = y_c$. Note that $x_{c1} < x_{c2}$. Because f is $\vee$-unimodal $f(y_a) < f(y_b)$ for $y_a, y_b \in [y_0, y_c]$ such that $y_a > y_b$, and furthermore, $f(y_a) > f(y_b)$ for $y_a, y_b \in [y_c, y_1]$ such that $y_a > y_b$. Thus, for all $x \in \mathcal{J}_1$, $f(y_{\max}(x)) < f(y_{\min}(x))$, and, for all $x \in \mathcal{J}_2$, $f(y_{\max}(x)) > f(y_{\min}(x))$.

Let $\mathcal{J}_3 = [x_{c1}, x_{c2}]$. Since $\mathcal{C}$ and f are piecewise monotonic, $\mathcal{C}_1 = \{(x, f(y_{\max}(x))) : x \in \mathcal{J}_3\}$ is monotonically increasing and $\mathcal{C}_2 = \{(x, f(y_{\min}(x))) : x \in \mathcal{J}_3\}$ is monotonically decreasing. Furthermore, it follows from Lemma 5.3.1 that $\mathcal{C}_1 \cap \mathcal{C}_2$ consists of a unique point (x_*, y_*). Now, for all $x \in \mathcal{I}_1 = (x_0, x_*)$, $f(y_{\max}(x)) < f(y_{\min}(x))$ while, for all $x \in \mathcal{I}_2 = (x_*, x_1)$, $f(y_{\max}(x)) > f(y_{\min}(x))$. Thus, (5.1) is satisfied for all $x \in \mathcal{I}_1$ and all $x' \in \mathcal{I}_2$, and thus $\mathcal{C}' = f(\mathcal{C})$ is a butterfly. □

We investigate the properties of the butterfly map created by applying a unimodal map to an oriented simple closed curve $\mathcal{C}$. The following definition is needed.

Definition 5.3.2. Let $\mathcal{C}$ be a simple closed curve or a butterfly and let $[x_0, x_1] \times$

$[y_0, y_1]$ be the smallest rectangle containing $\mathcal{C}$. A point $(x, y_0) \in \mathcal{C}$ is a *minimum* of $\mathcal{C}$. A point $(x, y_1) \in \mathcal{C}$ is a *maximum* of $\mathcal{C}$.

The following result is illustrated by Figure 5.7.

Theorem 5.3.2. Let $f : [y_0, y_1] \to \mathbb{R}$ be unimodal and let $\mathcal{C}$ be an oriented simple closed curve defined on the rectangle $[x_0, x_1] \times [y_0, y_1]$. Assume that, for each $y \in (y_0, y_1)$, there exists a unique pair of points $(x_{\min}(y), y)$, $(x_{\max}(y), y) \in \mathcal{C}$ such that $x_{\min}(y) < x_{\max}(y)$, and assume that $\mathcal{C}' \triangleq f(\mathcal{C})$ is a butterfly. If f is $\vee$-unimodal, then $\mathcal{C}'$ has exactly two minima, which are equal. Alternatively, if f is $\wedge$-unimodal, then $\mathcal{C}'$ has exactly two maxima, which are equal.

Proof. We assume that the map f is $\vee$-unimodal; the $\wedge$-unimodal case is analogous. Let $[x_0, x_1] \times [q_c, q_1]$ be the smallest rectangle containing $\mathcal{C}'$, and let $q = f(y)$, where $q \in [q_c, q_1]$. Let $y_c \in (y_0, y_1)$ satisfy $q_c = f(y_c)$. By Definition 5.2.1, y_c is the global minimizer of f. By assumption, there exist exactly two points $(x_{\min}(y_c), y_c)$ and $(x_{\max}(y_c), y_c) \in \mathcal{C}$ such that $x_{\min}(y_c) < x_{\max}(y_c)$. Applying f to these points yields $(x_{\min}(y_c), f(y_c)), (x_{\max}(y_c), f(y_c)) \in \mathcal{C}'$. Hence these points are minima of the curve $\mathcal{C}'$ and, since $x_{\min}(y_c) \neq x_{\max}(y_c)$, it follows that these points are distinct. Thus, the butterfly map $\mathcal{C}'$ has exactly two minima of equal value q_c. □

The following theorem is related to Theorem 5.3.2 and represents the dual of Theorem 5.3.1.

Theorem 5.3.3. Let $\mathcal{C}'$ be a butterfly and let $[x_0,\, x_1] \times [q_0, q_1]$ be the smallest rectangle with sides parallel to the x- and y-axes containing $\mathcal{C}'$. Decompose $\mathcal{C}'$ as the union of two branches, namely, branch $\mathcal{B}_+$ associated with increasing x and branch $\mathcal{B}_-$ associated with decreasing x. Furthermore, define $g_+ : [x_0,\, x_1] \to [q_0, q_1]$ and $g_- : [x_0,\, x_1] \to [q_0, q_1]$, such that $\mathcal{B}_+$ and $\mathcal{B}_-$ are the graphs of g_+ and g_-, respectively. (a) Assume that $\mathcal{C}'$ has exactly two minima (x_a, q_c), (x_b, q_c), with $x_0 < x_a < x_b < x_1$ and $q_c = q_0$. Furthermore, assume that g_+ (resp., g_-) is decreasing on $[x_0, x_b]$ and

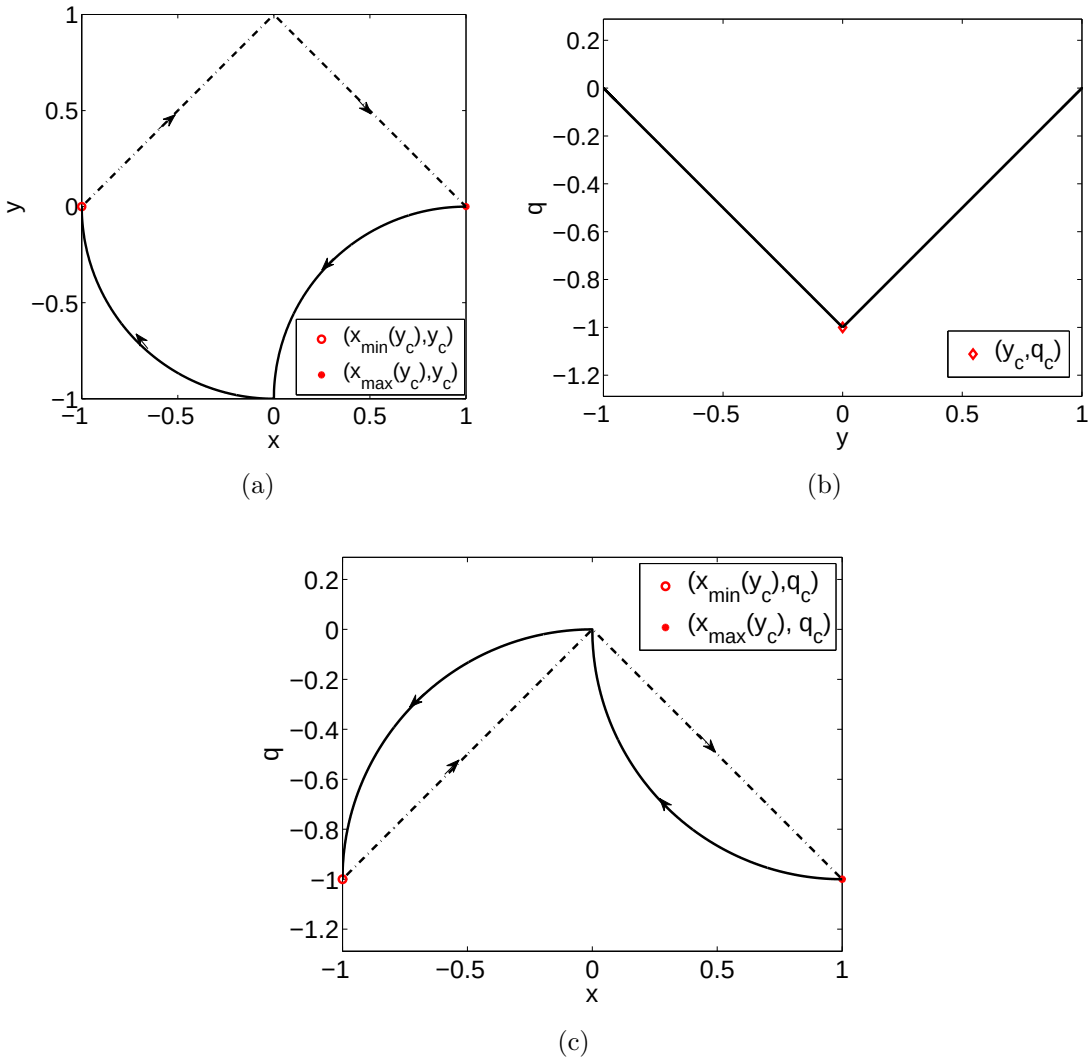

Figure 5.7: Illustration of the proof of Theorem 5.3.2. The simple closed curve $\mathcal{C}$ and points $(x_{\min}(y_c), y_c)$ and $(x_{\max}(y_c), y_c)$ are shown in (a). The $\vee$-unimodal map f and the point (y_c, q_c) are shown in (b). The butterfly map $\mathcal{C}'$ and the points $(x_{\min}(q_c), q_c)$ and $(x_{\max}(q_c), q_c)$ are shown in (c).

increasing on $[x_b, x_1]$, and g_- (resp., g_+) is decreasing on $[x_0, x_a]$ and increasing on $[x_a, x_1]$. Then, for each $\vee-$unimodal function f with minimum value q_c, there exist a piecewise monotonically increasing simple closed curve $\mathcal{C}_1$ with counterclockwise (resp., clockwise) orientation and a piecewise monotonically decreasing simple closed curve $\mathcal{C}_2$ with clockwise (resp., counterclockwise) orientation, such that $\mathcal{C}' = f(\mathcal{C}_1) = f(\mathcal{C}_2)$.

(b) Assume that $\mathcal{C}'$ has exactly two maxima (x_a, q_c), (x_b, q_c), with $x_0 < x_a < x_b < x_1$ and $q_c = q_1$. Furthermore, assume that g_+ (resp., g_-) is increasing on $[x_0, x_b]$ and decreasing on $[x_b, x_1]$, and g_- (resp., g_+) is increasing on $[x_0, x_a]$ and decreasing on $[x_a, x_1]$. Then, for each $\wedge-$unimodal function f with maximum value q_c, there exist a piecewise monotonically increasing simple closed curve $\mathcal{C}_1$ with counterclockwise (resp., clockwise) orientation and a piecewise monotonically decreasing simple closed curve $\mathcal{C}_2$ with clockwise (resp., counterclockwise) orientation, such that $\mathcal{C}' = f(\mathcal{C}_1) = f(\mathcal{C}_2)$.

Proof. We prove the case in (a) where g_+ is decreasing on $[x_0, x_b]$ and increasing on $[x_b, x_1]$, and g_- is decreasing on $[x_0, x_a]$ and increasing on $[x_a, x_1]$, as illustrated in Figure 5.8(a). The other case in (a) and the two cases in (b) can be proven analogously. Let f be a $\vee-$unimodal function, such that $f(y_c) = q_c$ for some y_c, and

$$f(y) = \begin{cases} f_-(y), & \text{if } y \leq y_c, \\ f_+(y), & \text{if } y \geq y_c, \end{cases}$$

where the continuous functions f_- and f_+ are strictly decreasing and increasing, respectively (Figure 5.8(b)). Let f_-^{-1} and f_+^{-1} denote the inverse functions of f_- and f_+, respectively, as illustrated in Figure 5.8(c). Note that f_-^{-1} is continuous and strictly decreasing, and f_+^{-1} is continuous and strictly increasing, with $y_c = f_-^{-1}(q_c) = f_+^{-1}(q_c)$.

Define a curve $\mathcal{C}_1$ on the plane as the union of four directed segments that are the

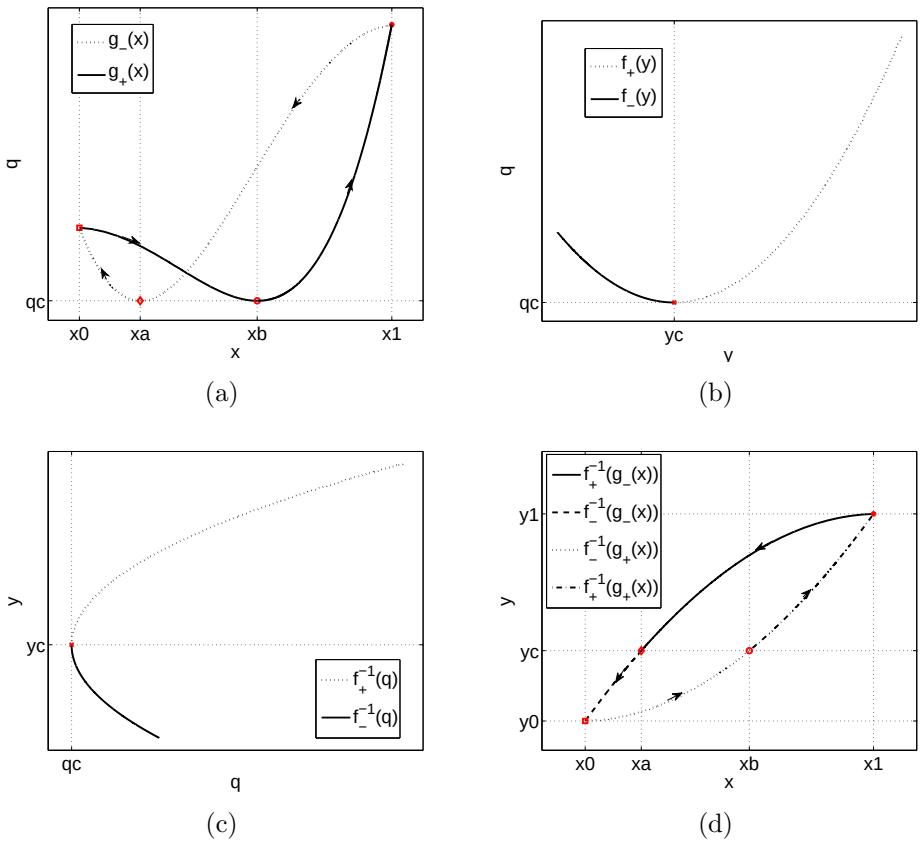

Figure 5.8: Illustration of the proof of Theorem 5.3.3. A butterfly $\mathcal{C}'$ is shown in (a), and a $\vee$-unimodal function f is shown in (b). The inverse functions of f_+ and f_- in (b) are shown in (c). The constructed simple closed curve $\mathcal{C}$ is shown in (d).

corresponding graphs of

$$y = f_-^{-1}(g_+(x)) \quad \text{as } x \text{ increases from } x_0 \text{ to } x_b, \tag{5.4}$$

$$y = f_+^{-1}(g_+(x)) \quad \text{as } x \text{ increases from } x_b \text{ to } x_1, \tag{5.5}$$

$$y = f_+^{-1}(g_-(x)) \quad \text{as } x \text{ decreases from } x_1 \text{ to } x_a, \tag{5.6}$$

$$y = f_-^{-1}(g_-(x)) \quad \text{as } x \text{ decreases from } x_a \text{ to } x_0, \tag{5.7}$$

as illustrated in Figure 5.8(d). Since $f_-^{-1}(g_+(x_b)) = f_-^{-1}(q_c) = y_c = f_+^{-1}(g_+(x_b))$, $f_+^{-1}(g_+(x_1)) = f_+^{-1}(g_-(x_1))$ (from continuity of $\mathcal{C}'$), $f_+^{-1}(g_-(x_a)) = y_c = f_-^{-1}(g_-(x_a))$,

and $f_-^{-1}(g_-(x_0)) = f_-^{-1}(g_+(x_0))$ (from continuity of $\mathcal{C}'$), $\mathcal{C}_1$ is continuous and closed.

Define $y = h_+(x)$ on $[x_0, x_1]$ using (5.4) and (5.5), and define $y = h_-(x)$ on $[x_0, x_1]$ using (5.6) and (5.7). Namely, h_+ and h_- represent the two branches of $\mathcal{C}_1$ associated with increasing and decreasing x, respectively. Using the properties of $f_\pm^{-1}$ and $g_\pm$, it can be shown that both h_+ and h_- are strictly increasing functions of x. Furthermore, for each $x \in (x_0, x_1)$, $h_+(x) < h_-(x)$. Therefore, $\mathcal{C}_1$ is a simple closed curve with counterclockwise orientation. Finally, $f(\mathcal{C}_1)$ can be defined as

$$
\begin{aligned}
f_-(y) = f_-(f_-^{-1}(g_+(x))) &= g_+(x) \text{as } x \text{ increases from } x_0 \text{ to } x_b, \\
f_+(y) = f_+(f_+^{-1}(g_+(x))) &= g_+(x) \text{as } x \text{ increases from } x_b \text{ to } x_1, \\
f_+(y) = f_+(f_+^{-1}(g_-(x))) &= g_-(x) \text{as } x \text{ decreases from } x_1 \text{ to } x_a, \\
f_-(y) = f_-(f_-^{-1}(g_-(x))) &= g_-(x) \text{as } x \text{ decreases from } x_a \text{ to } x_0,
\end{aligned}
$$

and, thus, $\mathcal{C}' = f(\mathcal{C}_1)$.

Similarly, we define the curve $\mathcal{C}_2$ using

$$
\begin{aligned}
y &= f_+^{-1}(g_+(x)) \quad \text{as } x \text{ increases from } x_0 \text{ to } x_b, && (5.8) \\
y &= f_-^{-1}(g_+(x)) \quad \text{as } x \text{ increases from } x_b \text{ to } x_1, && (5.9) \\
y &= f_-^{-1}(g_-(x)) \quad \text{as } x \text{ decreases from } x_1 \text{ to } x_a, && (5.10) \\
y &= f_+^{-1}(g_-(x)) \quad \text{as } x \text{ decreases from } x_a \text{ to } x_0. && (5.11)
\end{aligned}
$$

Following the same line of reasoning as above, it follows that $\mathcal{C}_2$ is a piecewise monotonically decreasing, simple closed curve with clockwise orientation, and $\mathcal{C}' = f(\mathcal{C}_2)$.

□

5.4 Hysteresis in a Preloaded Two-Bar Linkage Mechanism

In this section, we give a detailed analysis of a mechanical system in which two output variables are related by a unimodal map in order to demonstrate that our theoretical results can be used in practice. We analyze the dynamics of the two-bar linkage with joints P, Q, and R and preloaded by a spring with stiffness constant k as shown in Figure 5.9. The purpose of this discussion is to show that we can transform a simple hysteresis map into a butterfly through a unimodal map. That is, that the shape of the hysteresis map in this mechanism depends on the output variable because the two possible outputs are related through a unimodal function. Additional details of derivations are given by [23].

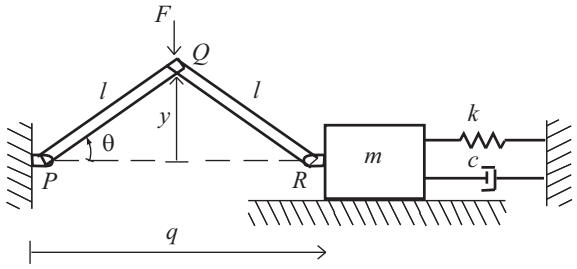

Figure 5.9: The preloaded two-bar linkage with a vertical force F acting at the joint Q. The word 'preloaded' refers to the presence of the spring with stiffness constant k, which is compressed when the two-bar linkage is in the horizontal equilibrium.

A constant vertical force F is applied at Q, where the two bars are joined by a frictionless pin. Let θ denote the counterclockwise angle that the left bar makes with the horizontal, and let q denote the distance between the joints P and R. When $F = 0$, the linkage has three equilibrium configurations. In Figure 5.10(a) and (b), the values of q and θ are q_0 and $\pm\theta_0$, respectively, and the spring k is relaxed. Note that $q_0 = 2l\cos\theta_0$. For the third equilibrium shown in Figure 5.10(c), both bars are horizontal with $\theta = 0$.

Note that y is the vertical distance from the joint Q to the horizontal equilibrium,

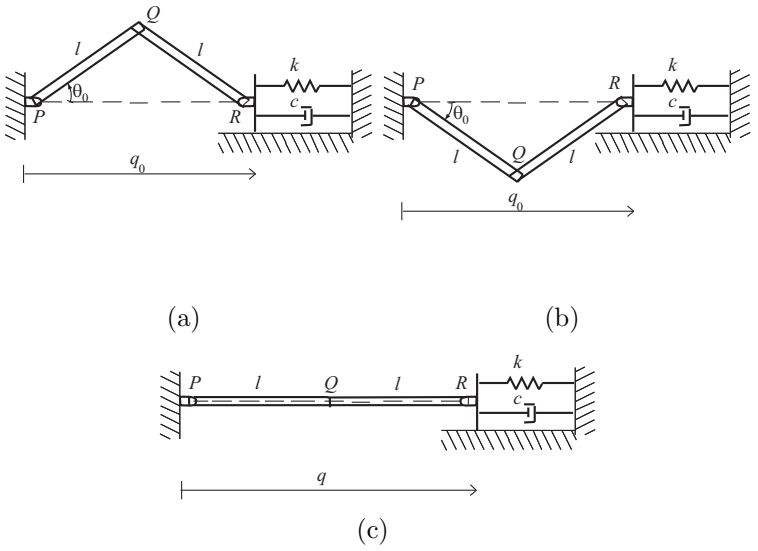

Figure 5.10: Static equilibria of the preloaded two-bar linkage when the spring is relaxed and $F = 0$. In (a) the equilibrium angle θ_0 is positive, in (b) the angle is negative, and in (c) $\theta = 0$. Equilibria in (a) and (b) are stable, while the equilibrium in (c) is unstable.

and q is the horizontal distance from joint P to joint R as shown in Figure 5.9. The static equilibria of the system are given by

$$(\sin\theta)\left(1 - \frac{\cos\theta_0}{\cos\theta}\right) = \frac{F}{4kl}. \tag{5.12}$$

The equilibrium set $\mathcal{E}$ for the preloaded two-bar linkage is the set of points (F, y) that satisfy

$$y\left(1 - \frac{l\cos\theta_0}{\sqrt{l^2 - y^2}}\right) = \frac{F}{4k}. \tag{5.13}$$

Alternatively, set $\mathcal{E}$ can be expressed as the set of points (F, q) that satisfy

$$\pm\sqrt{(4l^2 - q^2)}\left(1 - \frac{2l\cos\theta_0}{q}\right) = \frac{F}{2k}. \tag{5.14}$$

Relations (5.13) and (5.14) are obtained from (5.12) using

$$y = l\sin\theta, \quad q = 2l\cos\theta, \tag{5.15}$$

respectively. The equilibrium sets $\mathcal{E}$ defined by (5.13)-(5.14) are shown in the Figure 5.11. Set $\mathcal{E}$ is useful for analyzing the hysteresis of the preloaded two-bar linkage. It is shown in [54] that a system that exhibits hysteresis has a multi-valued equilibrium map and that the hysteresis map is a subset of the equilibrium map. It can be seen from the equilibrium set $\mathcal{E}$ in Figure 5.11 that multiple equilibria exist for each constant $F \in (-0.375, 0.375)$.

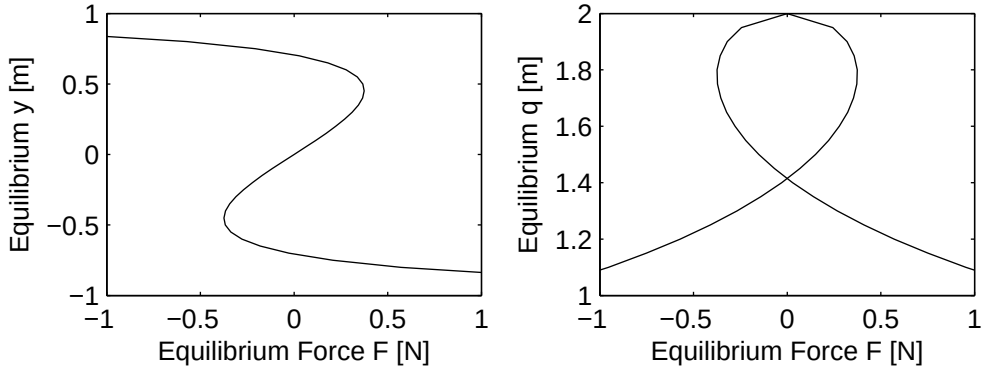

Figure 5.11: Equilibrium sets $\mathcal{E}$ for the preloaded two-bar linkage. The set $\mathcal{E}$ defined by (5.13) is shown on the left, while the set $\mathcal{E}$ defined by (5.14) is shown on the right. The parameter values are $\theta_0 = \pi/4$ rad, $k = 1$ N-m, and $l = 1$ m.

The equations of motion for the preloaded two-bar linkage are given by

$$\begin{aligned}\Big((2ml^2 + \frac{9}{8}m_{\text{bar}}l^2)\sin^2\theta + \frac{5}{24}m_{\text{bar}}l^2\Big)\ddot{\theta} \\ + (2ml^2 + \frac{9}{8}m_{\text{bar}}l^2)(\sin\theta)(\cos\theta)\dot{\theta}^2 \\ + 2kl^2(\cos\theta_0 - \cos\theta)(\sin\theta) \\ + 2cl^2(\sin\theta)^2\dot{\theta} = -\frac{l\cos\theta}{2}F,\end{aligned} \tag{5.16}$$

where m_{bar} is the inertia of each bar. Using (5.15) the dynamics (5.16) can be expressed in terms of the displacement q as

$$\begin{aligned}\Big((m+\frac{9}{16}m_{\text{bar}})(4l^2-q^2)+\frac{5}{12}m_{\text{bar}}l^2\Big)(4l^2-q^2)\ddot{q}\\ +\frac{5}{12}m_{\text{bar}}l^2q\dot{q}^2+c\dot{q}(4l^2-q^2)^2\\ +k(q-q_0)(4l^2-q^2)^2=\frac{1}{2}q(4l^2-q^2)^{\frac{3}{2}}F.\end{aligned} \tag{5.17}$$

We use (5.16) and (5.17) to simulate the linkage dynamics under the periodic external force $F = \sin(\omega t)$ N with parameter values $k = 1$ N/m, $m = 1$ kg, $c = 1$ N-s/m, $m_{\text{bar}} = 0.5$ kg, and $l = 1$ m. As shown in Figure 5.12 there exists a nontrivial clockwise hysteresis map from the vertical force F to the vertical displacement y at low frequencies. The presence of a nontrivial loop at asymptotically low frequencies constitutes hysteresis. Note that the signed area of each hysteresis loop is equal to the energy dissipated in one cycle. Figure 5.13 shows the input-output map between the vertical force F and horizontal displacement q. At asymptotically low frequencies this input-output map is a symmetric butterfly with two loops of opposite orientation. The energy dissipated in one cycle is equal to the sum of the signed areas of the two loops. Because the loops have equal area, but opposite orientation, the total energy dissipated is zero. Energy is not dissipated since the force F and the displacement q are orthogonal. A comparison of the hysteresis maps and the equilibrium sets $\mathcal{E}$ for the preloaded two-bar linkage is shown in Figure 5.14.

Thus the hysteresis map is a simple closed curve when the output variable is y and a butterfly when the output variable is q. From (5.15) we find the unimodal map $f = \sqrt{4(l^2-y^2)}$, which transforms the simple map to a butterfly and is shown in Figure 5.15.

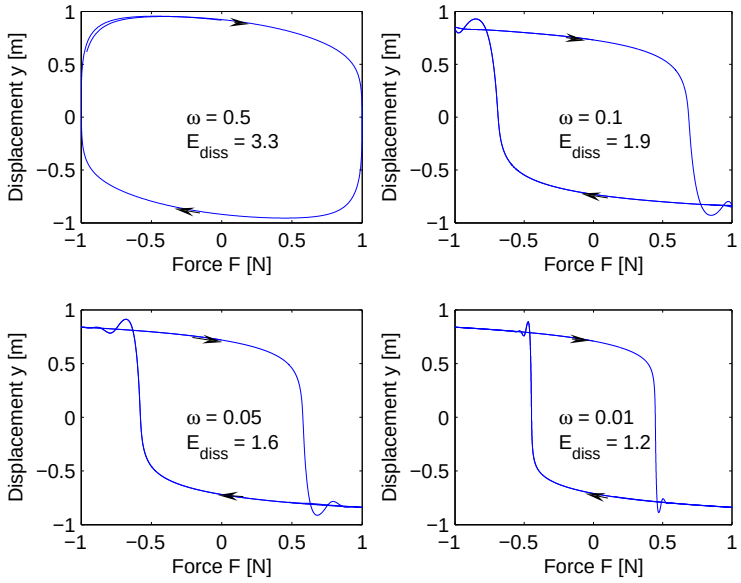

Figure 5.12: Input-output maps between the vertical force F and the vertical displacement y for the two-bar linkage model (5.16) for several values of frequency ω in rad/s. The nonvanishing clockwise displacement-force loop at asymptotically low frequencies is the hysteresis map. E_{diss}, which is the area of each loop, is the energy dissipated in one complete cycle. The parameter values are $k = 1$ N/m, $m = 1$ kg, $c = 1$ N-s/m, $m_{\text{bar}} = 0.5$ kg, $l = 1$ m, and $F(t) = \sin(\omega t)$ N.

5.5 Hysteresis in a Magnetostrictive Actuator

In this section we present butterfly hysteresis data obtained from a magnetostrictive actuator. We find the unimodal function that relates the butterfly hysteresis map to a simple hysteresis map. The simple hysteresis map can be modeled with a generalized Prandtl-Ishlinskii model, which is invertible and thus can be used to compensate for the hysteresis in the magnetostrictive actuator.

A Terfenol-D magnetostrictive actuator manufactured by Etrema Products, Inc. exhibits displacement to current butterfly hysteresis shown in Figure 5.16. In order to transform the butterfly into a simple hysteresis map, we adopt the following from [117].

Definition 5.5.1. Let ΔL be the change in the length of the magnetostrictive

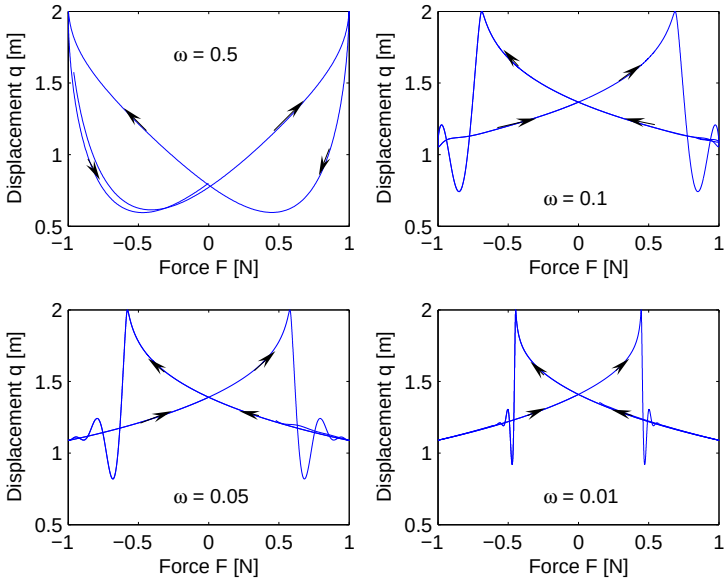

Figure 5.13: Input-output maps between the vertical force F and the horizontal displacement q for the two-bar linkage model (5.17) for several values of frequency ω in rad/s. The parameters values are $k = 1$ N/m, $m = 1$ kg, $c = 1$ N-s/m, $m_{\text{bar}} = 0.5$ kg, $l = 1$ m, and $F(t) = \sin(\omega t)$ N.

rod, and let L_{rod} be the length of the demagnetized rod. Then

$$\lambda \triangleq \frac{\Delta L}{L_{\text{rod}}} \tag{5.18}$$

is the *magnetostriction* in the rod.

We assume that the magnetostriction and magnetization M along the rod direction are related through a quadratic law

$$\lambda = a_1 M^2 + b_1, \tag{5.19}$$

where $a_1 = \dfrac{\lambda_s}{M_s^2}$, b_1 is a constant, λ_s is saturation value of magnetostriction, and M_s is the saturation value of magnetization. The input current I and the magnetic field

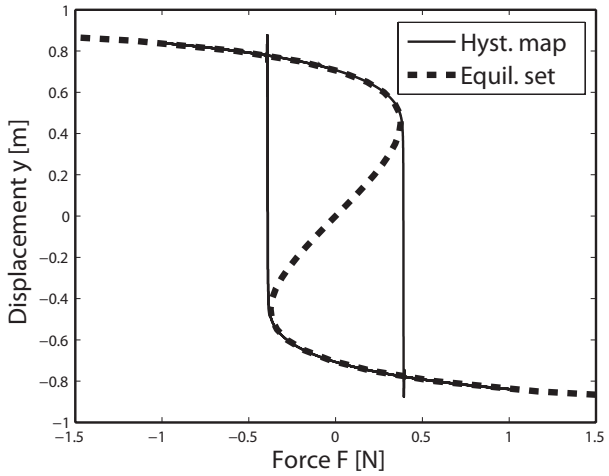

(a)

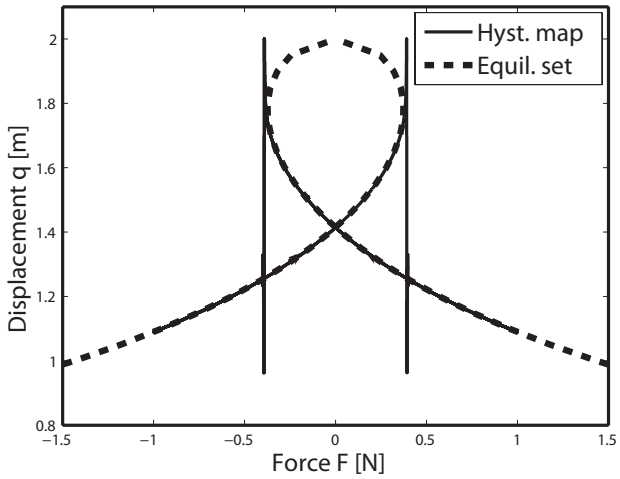

(b)

Figure 5.14: Comparison of the equilibrium sets $\mathcal{E}$ and the hysteresis maps for the preloaded two-bar linkage. The output variable is y in (a) and q in (b). The hysteresis map is a subset of $\mathcal{E}$ except for the vertical segments at the bifurcation points. The parameters values are as in Figure 5.12 with $F(t) = \sin(0.001t)$ N.

H are related through

$$H = c_0 I + H_{\text{bias}}, \tag{5.20}$$

where c_0 is the coil factor and H_{bias} is the bias field produced by dc current. Actuator

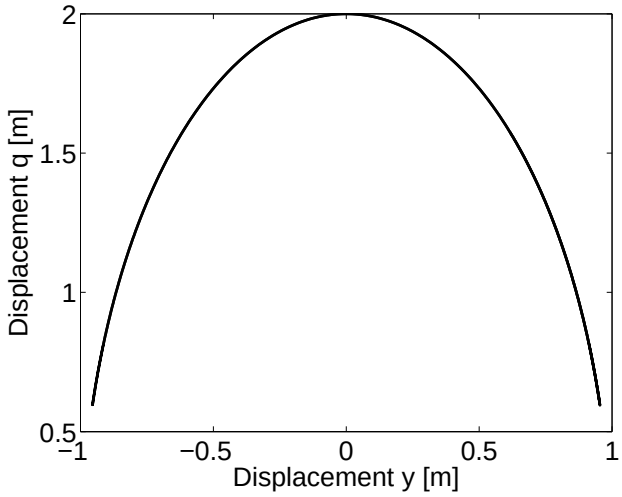

Figure 5.15: The $\wedge$-unimodal mapping function $f(y) = \sqrt{4(l^2 - y^2)}$ that transforms the simple hysteresis map of the buckling mechanism into a butterfly.

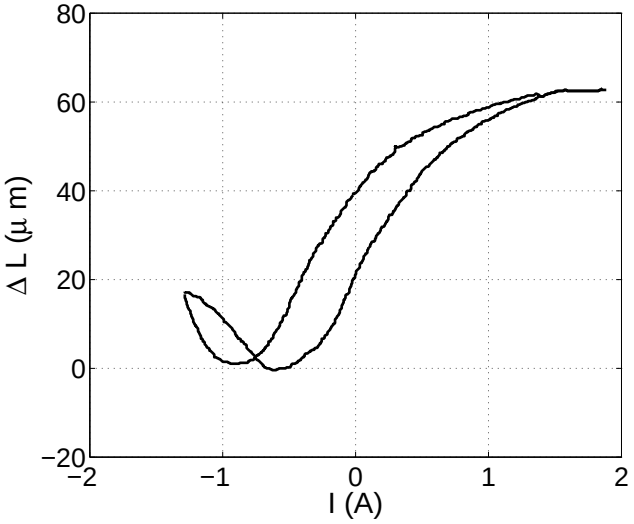

Figure 5.16: Experimental displacement-to-current butterfly hysteresis in a Terfenol-D magnetostrictive actuator.

specifications state that $M_s = 7.87 \times 10^5$ A/m, $L_{\text{rod}} = 5.13 \times 10^{-2}$ m, $c_0 = 1.54 \times 10^4$ m^{-1}; the remaining parameters are experimentally identified to be $\lambda_s = 1.313 \times 10^{-3}$ and $H_{\text{bias}} = 1.23 \times 10^4$ A/m.

Combining (5.18)-(5.20) we transform the butterfly curve in Figure 5.16 into a simple hysteresis curve between the magnetic field H and the magnetization along

the rod M. Using (5.18) and (5.19) we obtain

$$M = \pm\sqrt{\frac{\lambda - b_1}{a_1}}. \tag{5.21}$$

The sign of M is chosen such that the H to M hysteresis curve is piecewise monotonically increasing, as dictated by the physics. The resulting plot of λ versus M is shown in Figure 5.17(a). Equation (5.20) is used to calculate the values of the magnetic field H corresponding to the input current. The resulting H to M hysteresis map is shown in Figure 5.17(b). Notice that there is a vertical jump in the hysteresis map at the point where it crosses the x-axis. This jump is due to the fact that the two local minima of the butterfly map in Figure 5.16, while close, are not equal as expected from Theorem 5.3.2.

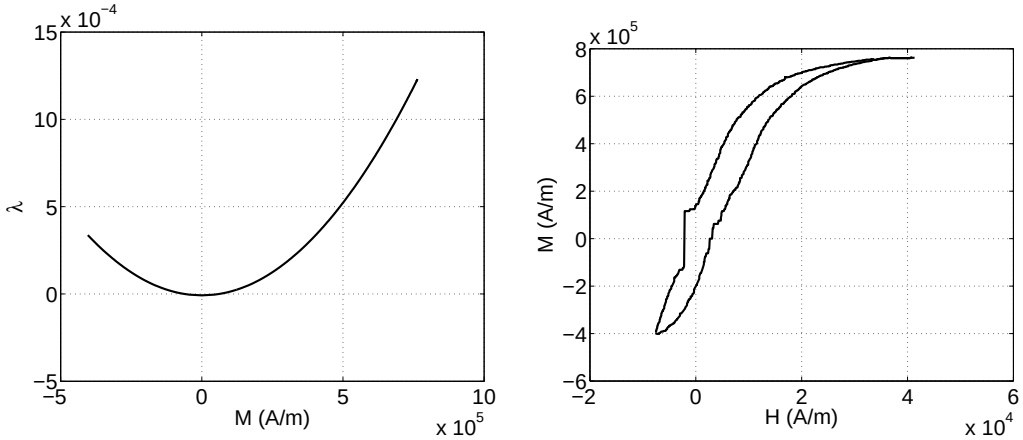

(a) (b)

Figure 5.17: Transformation from the butterfly to a simple closed curve. The $\vee$-unimodal relationship between M and λ obtained from (5.21) is shown in (a). (b) shows the simple hysteresis curve between the magnetic field H and magnetization M along the rod. A vertical jump due to unequal local minima of the butterfly map is visible at the point where the map crosses the H-axis.

To minimize the jump in the H-M hysteresis map, we now assume that the relationship between M and λ is hysteretic, as suggested by [120, 121]. That is, one

branch of the butterfly map in Figure 5.16 is transformed to M through (5.19), while the other branch is transformed through a unimodal map of the form

$$\lambda = a_2 M^2 + b_2, \tag{5.22}$$

where a_2 and b_2 are defined so that (5.19) and (5.22) form a closed hysteresis map. The hysteretic M-λ relationship is shown in Figure 5.18(a). The resulting H to M hysteresis map is shown in Figure 5.18(b).

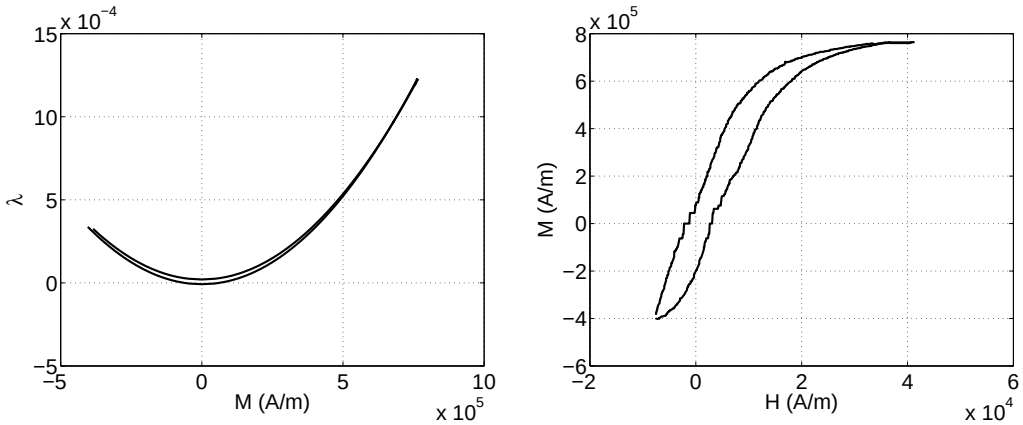

(a) (b)

Figure 5.18: Hysteretic unimodal relationship between M and λ obtained by applying (5.19) to one branch and (5.22) to the other branch of the butterfly map in Figure 5.16 is shown in (a). (b) shows the simple hysteresis curve between the magnetic field H and magnetization along the rod M obtained by applying a hysteretic $M - \lambda$ relationship to the butterfly hysteresis map.

In order to model the hysteresis in Fig. 5.18(b), we use a generalized Prandtl-Ishlinskii (PI) model defined by [72]. The generalized PI model consists of generalized play operators that are defined by the input u, threshold w, and envelope function γ.

The generalized Prandtl-Ishlinskii model utilizes N generalized play operators with thresholds w_i, $i = 1, \ldots, N$. Let the input $u(t)$ be a piecewise monotone continuous function on the interval $t \in [t_0, t_n]$, let $[t_0, t_n] = [t_0, t_1] \cup [t_1, t_2] \cup \cdots \cup [t_{n-1}, t_n]$, and define the initial state of the i-th play operator as $x_i(u(t_0)) = x_{0i}$. The output

of the generalized play operator i at time t_j, $j = 1, \ldots, n$ is defined as

$$x_i\big(u(t_j)\big) = \max\left(\gamma(u(t_j)) - w_i,\, \min\left(\gamma(u(t_j)) + w_i, x_i\left(u(t_{j-1})\right)\right)\right), \tag{5.23}$$

where $w \geq 0$ is the *threshold* of the generalized play operator and the strictly increasing continuous odd function $\gamma : \mathbb{R} \to \mathbb{R}$ is the *envelope function*. The output of the generalized PI model at time t_j is defined as

$$y(t_j) = q\gamma(u(t_j)) + \sum_{i=1}^{N} p(w_i) x_i(u(t_j)), \tag{5.24}$$

where q is a positive constant and $p(w)$ is a positive density function. As in [72], we use the envelope function

$$\gamma(v) = c_0 \tanh(c_1 v + c_2) + c_3 \tag{5.25}$$

and the density function

$$p(w) = \rho e^{-\tau w}, \tag{5.26}$$

where $c_0, c_1, c_2, c_3, c_4, \rho, \tau$ are constants with $\rho > 0$. We assume that w varies as $w = k\beta$, $k = 1, \ldots, N$, $\beta > 0$. We utilize a least squares optimization routine that minimizes the error between the data and the model defined by

$$J = \frac{1}{2} \sum_{i=1}^{m} (y(i) - M(i))^2, \tag{5.27}$$

where m is the number of available data points of M. The values of M and H are scaled by $k = 10^{-4}$ in order to avoid numerical problems. The output of the optimization is summarized in Table 5.1.

Comparison of the output of the identified generalized PI model (5.23)-(5.24) with

Parameter	Identified value
c_0	4.0904
c_1	0.7774 m/A
c_2	-0.0666
c_3	-0.2686
ρ	4.6403 A/m
τ	-0.1909
q	11.9609 A/m
β	1.1386

Table 5.1: Identified parameters of the generalized PI model from the least squares optimization routine.

parameters in Table 5.1 and experimental data in Figure 5.18(b) is shown in Figure 5.19(a). Using (5.18)-(5.20) and (5.22) we convert the output of the generalized PI model from Figure 5.19(a) into a butterfly hysteresis curve. The comparison of this butterfly map and the experimentally measured data from Figure 5.16 is shown in Figure 5.19(b).

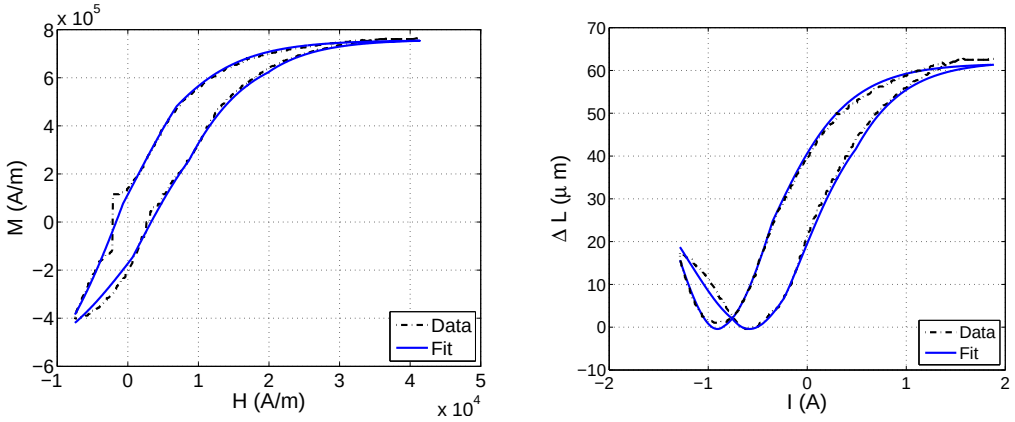

(a) (b)

Figure 5.19: Comparison of the experimental data and the output of the PI model. (a) compares the experimental data shown in Figure 5.18(b) and the output of the generalized PI model (5.23)-(5.24) with parameters defined in Table 5.1. (b) compares the butterfly map from experimental data in Figure 5.16 and the butterfly map obtained by applying (5.19), (5.20), and (5.22) to the output of the generalized PI model with parameters defined in Table 5.1.

5.6 Conclusions

We studied the relationship between simple and butterfly hysteresis maps and showed that the simple closed curve and butterfly are related by a unimodal map. Constraints can be placed on the types of simple closed curves that can be transformed into butterflies and the types of unimodal maps that can achieve this transformation.

To illustrate, we start with the hysteresis map of the preloaded two-bar linkage. The hysteresis map of this system is a simple closed curve in terms of the force input and linkage joint displacement. However, if the output is the displacement of the spring-loaded mass, then the hysteresis map is a butterfly. The butterfly appears due to the unimodal mapping between the linkage-joint displacement and the displacement of the spring-loaded mass.

Furthermore, we show that the unimodal transformation between simple and butterfly curves can be used to compensate for hysteresis in a magnetostrictive actuator. We use a quadratic law to relate the change of length of a specimen of magnetostrictive material to the magnetization along the rod direction, and to transform the butterfly map into a simple hysteresis map. The simple hysteresis map is monotone and can be fitted and inverted.

Future work includes the extension of these results to include hysteretic unimodal maps and multibutterflies. The use of hysteretic unimodal maps could give more flexibility in the types of butterflies that can be obtained from a given simple closed curve and enable easier fits to experimental data in control applications.

CHAPTER VI

Conclusions

In this work, we have considered friction models which are based on frictionless and lossless interactions of physical elements, such as masses, springs, and dashpots. The interaction of these elements leads to emergence of a hysteretic model for friction.

In Chapter II of this dissertation, we introduced the multiplay model of hysteresis, which consists of a parallel connection of N mass/spring/dashpot with deadzone elements. This hysteresis model has nonlocal memory and its hysteresis map is completely determined by the stiffness coefficients and widths of the gaps of the deadzone elements. The multiplay model can be used to model a hysteretic system with a hysteresis map possessing the symmetry of the cyclic rotation group C_2. Parameters of the multiplay model can be determined based on the slope of the desired hysteresis map. Once the multiplay model parameters are know, two different algorithms can be used to invert the model to aid in control applications.

In Chapter III, we developed an asperity-based friction model. This friction model is based on the frictionless and lossless interaction of a body with a row of rigid bristles. The bristles represent the roughness of the contacting surfaces. The rotating bristle model is based on bristles that are attached to the ground through a torsional spring and a dashpot. As the body moves the bristles pivot and counteract its motion, energy is used to compress the spring at the base of each bristle. As the body passes

over the bristle, the bristle is suddenly released, and the energy stored in the spring is dissipated by a dashpot regardless of how slowly the mass moves. Consequently, the bristle model is hysteretic.

The rotating bristle model exhibits quasi-stick-slip, similar to exact stick-slip but where the stick phase is replaced by a backward movement. Thus, we introduced the discontinuous rotating bristle model (DRBM), which exhibits exact stick-slip and hysteresis and is identical to the rotating bristle model except during direction reversals.

We then simplified the DRBM to obtain single-state friction models that are continuous and have the same stick-slip properties as the DRBM. For the FFBM single-state model the internal friction state represents the contribution of each bristle to the friction force. For the MPABM, the internal friction state is given by the exponentially weighted moving average of the sum of the pivot angles of all of the bristles contributing to the friction force. The FFBM and MPABM single-state friction models are closely related to the LuGre model and exhibit exact stick-slip and hysteresis. Thus, we showed that the interaction of the bristles and a body results in the friction force that has the properties of experimentally based friction models such as LuGre.

In Chapter IV, we developed the compressed bristle model, an asperity based friction model in which the friction force arises through the frictionless and lossless interaction of a body with an endless row of bristles. The bristles represent the microscopic roughness of the contacting surfaces. The bristles consist of a frictionless roller attached to the ground through a linear spring. The body is allowed to move horizontally and vertically over the bristles which are compressed and a reaction force occurs at the point of contact. Friction force is the sum of all horizontal components of the contact forces between all of the bristles and the body. As the body passes over the compressed bristles, they are released and the energy stored in the spring is

dissipated regardless of how slowly the body moves. Thus, energy is dissipated in the limit of DC operation and the system is hysteretic.

In the vertical direction, the body and the bristles form an undamped oscillator. The body oscillates vertically regardless of whether it is moving horizontally or not. During the vertical oscillations, as the body rises, the friction force decreases and the body speeds up. This mechanism gives rise to the dynamic Stribeck effect. We referred to it as dynamic Stribeck effect since the friction force-velocity curve forms a loop.

Furthermore, we showed that the compressed bristle model exhibits stick-slip friction and that the compressed bristle model equations can be simplified to give a single-state friction model. The simplified bristle model (SBM) retains the stick-slip and hysteresis properties of the compressed bristle model. The internal friction state of the SBM can be interpreted as the average deflection of the bristles from their relaxed length. The simplified compressed bristle model is equivalent to the LuGre model.

We studied the relationship between simple and butterfly hysteresis maps and showed that the simple closed curve and butterfly are related by a unimodal map in Chapter V. Constraints can be placed on the types of simple closed curves that can be transformed into butterflies and the types of unimodal maps that can achieve this transformation.

To illustrate, we started with the hysteresis map of the preloaded two-bar linkage. The hysteresis map of this system is a simple closed curve in terms of the force input and linkage joint displacement. However, if the output is the displacement of the spring-loaded mass, then the hysteresis map is a butterfly. The butterfly appears due to the unimodal mapping between the linkage-joint displacement and the displacement of the spring-loaded mass.

Furthermore, we showed that the unimodal transformation between simple and

butterfly curves can be used to compensate for hysteresis in a magnetostrictive actuator. We used a quadratic law to relate the change of length of a specimen of magnetostrictive material to the magnetization along the rod direction, and to transform the butterfly map into a simple hysteresis map. The simple hysteresis map is monotone and can be fitted and inverted.

Future work includes the extension of these results to include hysteretic unimodal maps and multibutterflies. The use of hysteretic unimodal maps could give more flexibility in the types of butterflies that can be obtained from a given simple closed curve and enable easier fits to experimental data in control applications.

BIBLIOGRAPHY

BIBLIOGRAPHY

[1] I. D. Mayergoyz and G. Friedman, "Generalized Preisach model of hysteresis," *IEEE Trans. on Magnet.*, vol. 24, no. 1, pp. 212–217, 1988.

[2] B. Armstrong-Hélouvry, *Control of Machines with Friction.* Boston, MA: Kluwer, 1991.

[3] M. A. Krasnosel'skii and A. V. Pokrovskii, *Systems with Hysteresis.* New York: Springer-Verlag, 1980.

[4] I. D. Mayergoyz, *Mathematical Models of Hysteresis.* Elsevier, 2003.

[5] F. Al-Bender and J. Swevers, "Characterization of friction force dynamics: Behavior and modeling on micro and macro scales," *IEEE Contr. Sys. Mag.*, vol. 28, no. 6, pp. 82–91, 2008.

[6] B. Armstrong-Hélouvry, P. Dupont, and C. Canudas de Wit, "A survey of models, analysis tools and compensation methods for the control of machines with friction," *Automatica*, vol. 30, no. 7, pp. 1083–1138, 1994.

[7] B. Feeny, A. Guran, N. Hinrichs, and K. Popp, "Historical review on dry friction and stick-slip phenomena," *Appl. Mech. Rev.*, vol. 51, no. 5, pp. 321–341, 1998.

[8] J. A. C. Martins, J. T. Oden, and F. M. F. Simoes, "Recent advances in engineering science: A study of static and kinetic friction," *Int. J. Eng. Sci.*, vol. 28, no. 1, pp. 29–92, 1990.

[9] A. Visintin, *Differential Models of Hysteresis.* New York: Springer-Verlag, 1994.

[10] D. J. Segalman, "A four-parameter Iwan model for lap-type joints," *J. Appl. Mech.*, vol. 72, pp. 752–760, September 2005.

[11] D. J. Segalman and M. J. Starr, "Inversion of masing models via continuous Iwan systems," *Int. J. Non-Lin. Mech.*, vol. 43, pp. 74–80, 2008.

[12] D. D. Quinn and D. J. Segalman, "Using series-series Iwan-type models for understanding joint dynamics," *J. Appl. Mech.*, vol. 72, pp. 666–673, 2005.

[13] D. J. Segalman, "Modeling joint friction in structural dynamics," *Struct. Contr. Health Monit.*, vol. 13, pp. 430–453, 2006.

[14] K. J. Nix and T. C. Lindley, "The application of fracture mechanics to fretting fatigue," *Fatigue and Fracture of Engineering Materials and Structures*, vol. 8, pp. 143–160, April 1985.

[15] D. A. Hills, D. Nowell, and J. J. O'Connor, "On the mechanics of fretting fatigue," *Wear*, vol. 125, pp. 129–146, 1988.

[16] B. Alfredsson and A. Cadario, "A study of fretting friction evolution and fretting fatigue crack initiation for a spherical contact," *Int. J. Fatigue*, vol. 26, pp. 1037–1052, 2004.

[17] E. D. Nicholas and W. M. Thomas, "A review of friction processes for aerospace applications," *Int. J. Materials and Product Technology*, vol. 13, pp. 45–55, November 1998.

[18] W. M. Thomas and E. D. Nicholas, "Friction stir welding for the transportation industries," *Materials and Design*, vol. 18, pp. 269–273, December 1997.

[19] R. John, K. V. Jata, and K. Sadananda, "Residual stress effects on near-threshold fatigue crack growth in friction stir welds in aerospace alloys," *Int. J. Fatigue*, vol. 25, pp. 939–948, 2003.

[20] T. Sakamoto, "Normal displacement and dynamic friction characteristics in a stick-slip process," *Tribology International*, vol. 20, no. 1, pp. 25–31, 1987.

[21] D. M. Tolstoi, "Significance of the normal degree of freedom and natural normal vibrations in contact friction," *Wear*, vol. 10, pp. 199–213, 1967.

[22] A. K. Padthe, B. Drincic, J. Oh, D. D. Rizos, S. D. Fassois, and D. S. Bernstein, "Duhem modeling of friction-induced hysteresis: Experimental determination of gearbox stiction," *IEEE Contr. Sys. Mag.*, vol. 28, pp. 90–107, October 2008.

[23] A. K. Padthe, N. A. Chaturvedi, D. S. Bernstein, S. P. Bhat, and A. M. Waas, "Feedback stabilization of snap-through buckling in a preloaded two-bar linkage with hysteresis," *Int. J. Non-Linear Mech.*, vol. 43, no. 4, pp. 277–291, 2008.

[24] H. Olsson, K. J. Åström, C. Canudas de Wit, M. Gafvert, and P. Lischinsky, "Friction models and friction compensation," *European Journal of Control*, vol. 4, no. 3, pp. 176–195, 1998.

[25] K. J. Astrom and C. Canudas-De-Wit, "Revisiting the LuGre friction model," *IEEE Control Systems Magazine*, vol. 28, no. 6, pp. 101–114, 2008.

[26] F. Avanzini, S. Serafin, and D. Rocchesso, "Modeling interaction between rubbed dry surfaces using an elasto-plastic friction model," in *Proc. 5^{th} Int. Conference on Digital Audio Effects*, Hamburg, Germany, September 2002, pp. 111–116.

[27] C. Canudas de Wit, H. Olsson, K. J. Åström, and P. Lischinsky, "A new model for control of systems with friction," *IEEE Trans. Autom. Contr.*, vol. 40, no. 3, pp. 419–425, 1995.

[28] N. Barabanov and R. Ortega, "Necessary and sufficient conditions for passivity of the LuGre friction model," *IEEE Trans. Autom. Contr.*, vol. 45, no. 4, pp. 675–686, 2000.

[29] C. Makkar, W. E. Dixon, W. G. Sawyer, and G. Hu, "A new continuously differentiable friction model for control systems design," in *IEEE/ASME Int. Conf on Adv. Intell. Mechatronics*, Monterey, CA, 2005, pp. 600–605.

[30] S. H. Park, J. S. Kim, J. J. Choi, and H.-O. Yamazaki, "Modeling and control of adhesion force in railway rolling stocks: Adaptive sliding mode control for the desired wheel slip," *IEEE Contr. Sys. Mag.*, vol. 28, no. 5, pp. 44–58, 2008.

[31] D. A. Haessig and B. Friedland, "On the modeling and simulation of friction," *ASME J. Dyn. Sys. Meas. Contr.*, vol. 113, pp. 354–361, 1991.

[32] N. E. Dowling, *Mechanical Behavior of Materials: Engineering Methods for Deformation, Fracture, and Fatigue.* Englewood Cliffs, NJ: Prentice Hall, 1993.

[33] F. Al-Bender, V. Lampaert, S. D. Fassois, D. D. Rizos, K. Worden, D. Engster, A. Hornstein, and U. Parlitz, "Measurement and identification of pre-sliding friction dynamics," in *Nonlinear Dynamics of Production Systems.* Weinheim: Wiley, 2004, pp. 349–367.

[34] D. D. Rizos and S. D. Fassois, "Presliding friction identification based upon the Maxwell slip model structure," *Chaos*, vol. 14, no. 2, pp. 431–445, 2004.

[35] F. Al-Bender, V. Lampaert, and J. Swevers, "Modeling of dry sliding friction dynamics: From heuristic models to physically motivated models and back," *Chaos*, vol. 14, no. 2, pp. 446–445, 2004.

[36] P. Dahl, "Solid friction damping of mechanical vibrations," *AIAA J.*, vol. 14, no. 2, pp. 1675–82, 1976.

[37] P. A. Bliman, "Mathematical study of the Dahl's friction model," *European J. of Mechanics and Solids*, vol. 11, no. 6, pp. 835–848, 1992.

[38] Y. Q. Ni, Z. G. Ying, J. M. Ko, and W. Q. Zhu, "Random response of integrable Duhem hysteretic systems under non-white excitation," *Int. J. Non-Linear Mech.*, vol. 37, no. 8, pp. 1407–1419, 2002.

[39] D. S. Bernstein, "Ivory ghost," *IEEE Control Systems Magazine*, vol. 27, no. 5, pp. 16–17, October 2007.

[40] H. Sahota, "Simulation of butterfly loops in ferroelectric materials," *Continuum Mechanics and Thermodynamics*, vol. 16, pp. 163–175, February 2004.

[41] J. Li and G. J. Weng, "A micromechanics-based hysteresis model for ferroelectric ceramics," *Journal of Intelligent Material Systems and Structures*, vol. 12, pp. 79–91, February 2001.

[42] J. A. Barker, D. E. Schreiber, B. G. Huth, and D. H. Everett, "Magnetic hysteresis and minor loops: Models and experiments," in *Proc. Royal Society of London A*, vol. 386, 1983, pp. 251–261.

[43] D. Croft, G. Shed, and S. Devasia, "Creep, hysteresis and vibration compensation for piezoactuators," *J. Dynamic Systems, Measurement and Control*, vol. 123, pp. 35–43, 2001.

[44] C. A. Dickinson, D. Hughes, and J. T. Wen, "Hysteresis in shape memory alloy actuators: The control issues," in *Proc. SPIE 2715*, 1996, pp. 494–506.

[45] R. B. Grobet and D. W. L. Wang, "General stability criteria for a shape memory alloy position control system," in *Proc. IEEE Conf. Robotics and Automation*, Nagoya, Japan, 1995, pp. 2313–2319.

[46] L. W. Carr, K. W. McAlister, and W. J. McCroskey, "Analysis of the development of dynamic stall based on oscillating airfoil measurements," NASA, Technical Report TN D-8382, 1977.

[47] D. Greenblatt and I. Wygnanski, "Dynamic stall control by periodic excitation, part 1: NACA parametric study," *Journal of Aircraft*, vol. 38, no. 3, pp. 430–438, 2001.

[48] S. Mittal and P. Saxena, "Prediction of hysteresis associated with the static stall of an airfoil," *AIAA J. Contr.*, vol. 38, no. 5, pp. 557–576, 2000.

[49] D. Angeli, J. E. Ferrell, and E. D. Sontag, "Detection of multistability, bifurcations, and hysteresis in a large class of biological positive feedback systems," in *Proc. Nat. Academy Sci.*, vol. 101, no. 7, 2004, pp. 1822–1827.

[50] D. Angeli and E. D. Sontag, "Multi-stability in monotone input/output systems," *Sys. Contr. Lett.*, vol. 51, pp. 185–202, 2004.

[51] A. Brown, A. Joshi, and M. Xiao, "Controlled steady-state switching in optical bistability," *Applied Physics Lett.*, vol. 83, no. 7, pp. 1301–1303, 2003.

[52] G. Cao and P. P. Banarjee, "Theory of hysteresis and bistability during transmission through a linear nondispersive-nonlinear dispersive interface," *J. Opt. Soc. Amer. B*, vol. 6, no. 2, pp. 191–198, 1989.

[53] B. Feeny, A. Guran, N. Hinrichs, and K. Popp, "Historical review on dry friction and stick-slip phenomena," *Appl. Mech. Rev*, vol. 51, no. 5, pp. 321–341, 1998.

[54] J. Oh and D. S. Bernstein, "Step-convergence analysis of nonlinear feedback hysteresis models," in *Proc. Amer. Contr. Conf.*, Portland, OR, June 2005, pp. 697–702.

[55] ——, "Semilinear Duhem model for rate-independent and rate-dependent hysteresis," *IEEE Trans. Autom. Contr.*, vol. 50, pp. 631–645, 2005.

[56] D. M. Rowson, "An analysis of stick-slip motion," *Wear*, vol. 31, pp. 213–218, 1975.

[57] H. Olsson and K. J. Åström, "Friction generated limit cycles," *IEEE Trans. on Cont. Sys. Tech.*, vol. 9, no. 4, pp. 629–636, 2001.

[58] R. I. Leine, D. H. V. Campen, and A. D. Kraker, "Stick-slip vibrations induced by alternate friction models," *Nonlin. Dynamics*, vol. 16, pp. 41–54, 1998.

[59] P. A. Bliman and M. Sorine, *Models of Hysteresis.* CRC Press, 1993, ch. Friction modeling by hysteresis operators. Application to Dahl, sticktion and Stribeck effects, pp. 10–19.

[60] F. Davi, "On domain switching in deformable ferroelectrics, seen as continua with microstructure," *Zeitschrift fr Angewandte Mathematik und Physik*, vol. 52, no. 6, pp. 966–989, November 2001.

[61] C. F. Marki, D. R. Jorgesen, H. Zhang, P. Wen, and S. C. Esener, "Observation of counterclockwise, clockwise and butterfly bistability in 1550 nm VCSOAs," *Optics Express*, vol. 15, no. 8, pp. 4953–4959, April 2007.

[62] S. Ducharme, A. V. Bune, L. M. Blinov, V. M. Fridkin, S. P. Palto, A. V. Sorokin, and S. G. Yudin, "Critical point in ferroelectric Langmuir-Blodgett polymer films," *Physical Review B*, vol. 57, no. 1, pp. 25–28, January 1998.

[63] J. Oh, B. Drincic, and D. S. Bernstein, "Nonlinear feedback models of hysteresis," *IEEE Control Systems Magazine*, vol. 29, no. 1, pp. 100–119, February 2009.

[64] I. D. Mayergoyz, *Mathematical Models of Hysteresis and Their Applications.* Amsterdam: Elsevier, 2003.

[65] G. Bertotti, *Hysteresis in Magnetism: For Physicists, Materials Scientists, and Engineers*, I. Mayergoyz, Ed. Academic Press, 1998.

[66] A. Visintin, *Differential Models of Hysteresis.* New York: Springer-Verlag, 1994.

[67] M. Brokate and A. Visintin, "Properties of the Preisach model for hysteresis," *J. Reine und Angewandte Mathematik*, vol. 402, pp. 1–40, 1989.

[68] G. Lin, D. Yang, and R. O. Warrington, "A computational model of the shape memory alloys for the design and control of micro actuators," *Micromechanical Systems*, vol. 40, pp. 171–181, 1992.

[69] D. Hughes and J. T. Wen, "Preisach modeling of piezoceramic and shape memory alloy hysteresis," *Smart Materials and Structures*, vol. 6, no. 3, pp. 287–300, 1997.

[70] M. Brokate and J. Sprekels, *Hysteresis and Phase Transitions*. New York, NY: Springer, 1996.

[71] K. Kuhnen, "Modeling, identification and compensation of complex hysteretic nonlinearities: A modified Prandtl-Ishlinskii approach," *European Jour. of Cont.*, vol. 9, no. 4, pp. 407–418, 2003.

[72] M. A. Janaideh, J. Mao, S. Rakheja, W. Xie, and C. Y. Su, "Generalized Prandtl-Ishlinskii hysteresis model: Hysteresis modeling and its inverse for compensation in smart actuators," *Proc. IEEE Conf. Dec. Contr.*, pp. 5182–5187, December 2008.

[73] N. J. Ahmad and F. Khorrami, "Adaptive control of systems with backlash hysteresis at the input," in *Proc. Amer. Contr. Conf.*, San Diego, CA, 1999, pp. 3018–3022.

[74] R. Boneh and O. Yaniv, "Control of an elastic two-mass system with large backlash," *J. Dynamic Systems, Measurement and Control*, vol. 121, no. 2, pp. 278–284, 1999.

[75] C. A. Desoer and S. M. Shahruz, "Stability of dithered nonlinear systems with backlash and hysteresis," *Int. J. Contr.*, vol. 43, no. 4, pp. 1045–1060, 1986.

[76] H. Cho and J. R. Barber, "Dynamic behavior and stability of simple frictional systems," *Mathl. Comput. Modeling*, vol. 28, no. 4-8, pp. 37–53, 1998.

[77] ——, "Stability of the three-dimensional Coulomb friction law," *Proc. R. Soc. Lond. A*, vol. 455, pp. 839–861, 1999.

[78] J. Swevers, F. Al-Bender, C. G. Ganseman, and T. Prajogo, "An integrated friction model structure with improved presliding behavior for accurate friction compensation," *IEEE Trans. Autom. Contr.*, vol. 45, no. 4, pp. 675–686, 2000.

[79] M. A. Krasnosel'skiĭ and A. V. Pokrovskiĭ, *Systems with Hysteresis*. New York: Springer-Verlag, 1980.

[80] M. Al Janaideh, S. Rakheja, and C. Y. Su, "A generalized rate dependent play operator for characterizing asymmetric and symmetric hysteresis nonlinearities," *Proc. Amer. Contr. Conf.*, pp. 1911–1916, June 2008.

[81] F. Al-Bender, W. Symens, J. Swevers, and H. V. Brussel, "Theoretical analysis of the dynamic behavior of hysteresis elements in mechanical systems," *Int. J. Non-Lin. Mech.*, vol. 39, pp. 1721–1735, 2004.

[82] F. Scheibe and M. C. Smith, "A behavioral view of play in mechanical networks," in *Proc. of the European Control Conference*, 2007, pp. 3755–3762.

[83] J. J. Choi, S. I. Han, and J. S. Kim, "Development of a novel dynamic friction model and precise tracking control using adaptive back-stepping sliding mode controller," *Mechatronics*, vol. 16, pp. 97–104, 2006.

[84] K. K. Leang, Q. Zou, and S. Devasia, "Feedforward control of piezoactuators in atomic force microscope systems," *IEEE Control Systems Magazine*, vol. 29, no. 1, pp. 70–82, February 2009.

[85] C. Makkar, G. Hu, W. G. Sawyer, and W. E. Dixon, "Lyapunov-based tracking control in presence of uncertain nonlinear parameterizable friction," *IEEE Trans. Autom. Contr.*, vol. 52, no. 10, pp. 1988–1994, 2007.

[86] Y. Guo, Z. Qu, Y. Braiman, Z. Zhang, and J. Barhen, "Nanotribology and nanoscale friction: Smooth sliding through feedback control," *IEEE Contr. Sys. Mag.*, vol. 28, no. 6, pp. 92–100, 2008.

[87] B. S. R. Armstrong and Q. Chen, "The z-properties chart: Visualizing the presliding behavior of state-variable friction models," *IEEE Control Systems Magazine*, vol. 28, no. 5, pp. 79–89, October 2008.

[88] R. I. Leine, D. H. V. Campen, A. De Kraker, and L. Van Den Steen, "Stick-slip vibrations induced by alternate friction models," *Nonlinear Dynamics*, vol. 16, pp. 41–45, 1998.

[89] N. B. Do, A. A. Ferri, and O. A. Bauchau, "Efficient simulation of a dynamic system with LuGre friction," *Journal of Computational and Nonlinear Dynamics*, vol. 2, pp. 281–289, 2007.

[90] L. C. Bo and D. Pavelescu, "The friction-speed relation and its influence on the critical velocity of stick-slip motion," *Wear*, vol. 82, pp. 277–289, 1982.

[91] C. J. Radcliffe and S. C. Southward, "A property of stick-slip friction models which promotes limit cycle generation," in *Proc. Amer. Contr. Conf.*, vol. 2, 1990, pp. 1198–1203.

[92] A. F. D'Souza and A. H. Dweib, "Self-excited vibrations induced by dry friction, part 2: Stability and limit-cycle analysis," *Journal of Sound and Vibration*, vol. 137, no. 2, pp. 177–190, 1990.

[93] P. Dupont, V. Hayward, B. Armstrong, and F. Altpeter, "Single state elastoplastic friction models," *IEEE Trans. Autom. Contr.*, vol. 47, no. 5, pp. 787–792, 2002.

[94] B. Drinčić and D. S. Bernstein, "A sudden-release bristle model that exhibits hysteresis and stick-slip friction," in *Proc. Amer. Contr. Conf.*, San Francisco, CA, June 2011, pp. 2456 – 2461.

[95] R. I. Leine and H. Nijmeijer, *Dynamics and bifurcations of non-smooth mechanical systems*. Berlin: Springer, 2004.

[96] A. F. Filippov, *Differential Equations with Discontinuous Righthand Sides*. Dordrecht, The Netherlands: Kluwer Academic Publishers, 1988.

[97] M. di Bernardo, C. J. Budd, A. R. Campneys, and P. Kowalczyk, *Piecewise-smooth Dynamical Systems*. London, UK: Springer-Verlag, 2008.

[98] P. Dupont, B. Armstrong, and V. Hayward, "Elasto-plastic friction model: Contact compliance and stiction," in *Proc. Amer. Contr. Conf.*, Chicago, IL, June 2000, pp. 1072–1077.

[99] G. E. P. Box, G. M. Jenkins, and G. C. Reinsel, *Time Series Analysis: Forecasting and Control*. Hoboken, New Jersey: Wiley, 2008.

[100] C. C. Holt, "Forecasting seasonals and trends by exponentially weighted moving averages," *Int. J. Forecasting*, vol. 20, pp. 5–10, 2004.

[101] A. K. Padthe, N. A. Chaturvedi, D. S. Bernstein, S. P. Bhat, and A. M. Waas, "Hysteresis analysis and feedback stabilization of snap-through buckling," *Proc. Amer. Contr. Conf.*, pp. 729–734, July 2003.

[102] F. Al-Bender, V. Lampert, and J. Swevers, "A novel generic model at asperity level for dry friction force dynamics," *Tribology Letters*, vol. 16, no. 1–2, pp. 81–93, 2004.

[103] B. Drinčić and D. S. Bernstein, "A frictionless bristle-based friction model that exhibits hysteresis and stick-slip behavior," *J. Sound and Vibration*, 2012, submitted.

[104] W. B. Horne and R. C. Dreher, "Phenomena of pneumatic tire hydroplaning," NASA, Technical Note TN D-2056, 1963.

[105] P. Andren and A. Jolkin, "Elastohydrodynamic aspects on the tyre-pavement contact at aquaplaning," Swedish National Road and Transport Research Institute, VTI rapport 483A, 2003.

[106] A. J. Tuononen and M. J. Matilainen, "Real-time estimation of aquaplaning with an optical tyre sensor," *Institution of Mechanical Engineers, Part D: J. Automobile Engineering*, vol. 223, pp. 1263–1272, 2009.

[107] X. Tan and R. V. Iyer, "Modeling and control of hysteresis," *IEEE Control Systems Magazine*, vol. 29, no. 1, pp. 26–29, February 2009.

[108] R. Cross, M. Grinfeld, and H. Lamba, "Hysteresis and economics: Taking the economic past into account," *IEEE Control Systems Magazine*, vol. 29, no. 1, pp. 30–43, February 2009.

[109] B. Appelbe, D. Flynn, H. McNamara, P. O'Kane, A. Pimenov, A. Pokrovskii, D. Rachinskii, and A. Zhezherun, "Rate-independent hysteresis in terrestrial hydrology," *IEEE Control Systems Magazine*, vol. 29, no. 1, pp. 44–69, February 2009.

[110] R. V. Iyer and X. Tan, "Control of hysteretic systems through inverse compensation," *IEEE Control Systems Magazine*, vol. 29, no. 1, pp. 83–99, February 2009.

[111] N. Ebine and K. Ara, "Magnetic measurement to evaluate material properties of ferromagnetic structural steels with planar coils," *IEEE Transaction on Magnetics*, vol. 35, no. 5, pp. 3928–3930, September 1999.

[112] P. Pakdeevanich and M. J. Adams, "Measurements and modeling of reflective bistability in 1.55-μm laser diode amplifiers," *IEEE Journal of Quantum Electronics*, vol. 35, no. 12, pp. 1894–1903, December 1999.

[113] O. Pietzsch, A. Kubetzka, M. Bode, and R. Wiesendanger, "Observation of magnetic hysteresis at the nanometer scale by spin-polarized scanning tunneling spectroscopy," *Science*, vol. 292, pp. 2053–2056, June 2001.

[114] M. Kamlah and C. Tsakmakis, "Phenomenological modeling of the non-linear electro-mechanical coupling in ferroelectrics," *International Journal of Solids and Structures*, vol. 36, no. 12, pp. 669–695, 1999.

[115] X. Tan and J. S. Baras, "Modeling and control of hysteresis in magnetostrictive actuators," *Automatica*, vol. 40, no. 9, pp. 1469–1480, 2004.

[116] G. J. Simitses, *An Introduction to the Elastic Stability of Structures*. Englewood Cliffs, NJ: Prentice Hall, 1967.

[117] X. Tan, "Control of smart actuators," Ph.D. dissertation, University of Maryland, College Park, MD, 2002.

[118] B. Drinčić and D. S. Bernstein, "Why are some hysteresis loops shaped like a butterfly?" in *Proc. Amer. Contr. Conf.*, St. Louis, MO, June 2009, pp. 3977–3982.

[119] V. Guillemin and A. Pollack, *Differential Topology*. Englewood Cliffs, NY: Prentice-Hall, Inc., 1974.

[120] E. Arakawa, K. Mori, H. Nishigaitsu, and N. Aizawa, "X-ray diffraction technique to observe magnetostriction and magnetization at coextensive volumes of iron," *IEEE Tran. on Magn.*, vol. 42, no. 1, January 2006.

[121] I. Brard, R. Georges, and G. L. Blevennec, "Magnetostrictive hysteresis in Nickel polycrystalline thick films," *J. Appl. Phys*, vol. 75, no. 10, May 1994.